A STUDY OF DIRECT POWDER ROLLING ROUTE FOR CP-TITANIUM

Centre for Material Engineering, University of Cape Town

Masters Dissertation

Student: Yu Zhang

Supervisor: Prof. R.D. Knutsen

September 2015

Abstract

Titanium and its alloys have extremely high strength to weight ratio and corrosion resistance. This has made titanium alloys very attractive materials for many structural applications. However, the high price of these alloys has seen their use restricted to very few high performance areas such as aerospace and bio-medical applications. The costs can be significantly reduced by directly converting titanium powder to metal products, particularly via the direct powder rolling process.

This present research is based on a parametric study of powder rolling and operational effects including rolling speed, roll gap size, roll surface width and powder feeding rate on the integrity of the metal powder compacted strip that is produced from the direct powder rolling process. The objectives of this work were to predict the powder rolling compaction performance in terms of compaction pressure, roll surface force and rolling torque, and produce the highest possible relative density of CP-titanium green strips by optimized rolling variable setups, and to achieve its full density by additional hot deformation processing. In this work, a purpose-built gravity fed vertical powder rolling mill with a roller diameter of 265 mm and a roller width of 150 mm was used. Johanson’s powder rolling model has been implemented to simulate performance and a series of rolling parameter setups have been conducted by the using a purpose-built powder rolling mill. Pre-alloyed, water-atomized stainless steel 316L powder and hydride-dehydride (HDH) CP-titanium powders with a mean particle size of 100 µm were used as the experimental material to validate the simulated results in terms of relative density and strip dimensions.

The powder rolling experiments were carried out based on the Johanson’s powder rolling model to conduct a parametric experimental study in various setups of powder rolling parameter combinations, including roll gap, roll face width, rolling speed and powder feeding rate. The rolling speed range was set to be 10, 12 and 14 rpm (maximum) since Johanson does not cover the rolling speed effect in the model. According to the modelling results, the roll gap range was set to be 0.5, 1 and 1.5 mm for obtaining effective rolling pressure. Three sizes of hopper outlet diameter (15, 20, 25 mm) were used in this experiment to investigate the powder feeding rate effect.

The relative density of the compacted green strip was measured according to the ASTM B962-13 [29] standard; the highest obtained relative densities of stainless steel and titanium from powder the powder rolling experiment were in excess of 82% and 85% respectively. The experimental results have shown that the powder compacted strip thickness is always larger than the roll gap size. The width of the powder compacted green strip is directly proportional to the rolling speed in the vertical rolling compactor and the relative density of metal powder increases as the roll gap is reduced and as the feeding rate is increased. Moreover, CP-titanium powder has significantly better rolling compaction performance compared to stainless 316L powder in terms of formability. Furthermore, the Johanson's model is able to provide reasonable prediction of nip angle and rolling pressure distribution for the gravity-fed vertical rolling compaction process.

Two types of CP-titanium green strips with average of 75% and 85% relative densities produced by optimized rolling setups were further subjected to vacuum sintering process at 1200 °C for 2 hours in order to investigate the sintering effect on a relative improvement in density of at least 7% was achieved for the 85% relative density green strip. Cold rolling and recrystallization annealing after sintering further provided substantial increase in density and the mechanical properties of the recrystallized strip are comparable to CP-titanium grade 2 wrought metal.

The achievement of this study can be used to provide a quality prediction of the direct powder rolling compaction process, and to design an optimal rolling mill and operating setups for producing powder compact sheet or strip. In addition, this work can be used as a starting point for further developing titanium alloy and related metal strip from the direct powder rolling route.

Acknowledgments

I would like to express my gratitude to all those who assistance me during this research work.

- Prof. Robert Knutsen, my supervisor of the project, for his constant encouragement and guidance. He has walked me through all the stages of this project. Without his consistent and illuminating instruction, this project could not have reached its present form.
- Mr Glen Newins, the Principal Technical Officer at University of Cape Town Mechanical Engineering Department workshop, for his assistance in workshop.
- Dr Silethelwe Chikosha, Senior Researcher at Council for Scientific and Industrial Research (CSIR), for her assistance in measuring the metal powder characteristics.
- All the staff, students and others involved at the Centre for Materials Engineering (CME) for giving me their help and time to me through these years.
- Last my thanks would go to my beloved family for their loving considerations in me all through these years.

Declaration

I, Yu Zhang, know that meaning of plagiarism and declare that all the work in this document, save for that which is properly acknowledged, is my own.

Signature: Signed by candidate

Date: 04/12/2015

Table of Contents

List of Acronyms and Abbreviations

PM – Powder Metallurgy

PA- Pre-Alloyed

NNS – Near-Net-Shape

CP – Commercially Pure

DPR – Direct Powder Rolling

HCP – Hexagonal Close Packed

HDH – Hydride-Dehydride

BBC – Body Centered Cubic

TTT – Temperature – Time – Transformation

SEM – Sanning Electron Microscopy

CIP – Cold Isostatic Pressing

HIP – Hot Isostatic Pressing

LM – Light Microscopy

PSC – Plane Strain Compression

EDS – Energy Dispersive Spectroscopy

Chapter 1

Introduction

1.1 Subject of the Dissertation

The subject of this thesis is to research the rolling parameters that influence the integrity of the compacted CP-titanium strip in terms of relative density and dimension so that the rolling process can be optimized for the production of strip or plate by direct powder rolling. This dissertation is based on the Johanson's powder rolling theory and involves a parametric study to determine the influence of variables including rolling speed, roll gap, roll surface width and powder feeding rate to achieve the relative density (>80%) of CP-titanium powder compacted strips. And to compare the post-deformation annealed condition of powder rolled CP-titanium strip with wrought CP-titanium grade 2 material in terms of mechanical properties.

1.2 Background to the Dissertation

Titanium and its alloys have extremely high strength to weight ratio and excellent corrosion resistance. This has been made titanium alloys very attractive materials for many structural applications. However, the high price of these alloys has seen their use restricted to very few high performance areas such as aerospace and bio-medical applications. Titanium is not a rare material and ranks as the ninth most plentiful element and the fourth most abundant structural metal in the earth. The high price of titanium is due to its high reactivity at high temperatures and therefore cannot be directly reduced from its dioxide. The only common commercial process currently producing pure titanium is the expensive and energy intensive Kroll Process [1] which produces titanium as a sponge-like material. In an attempt to reduce the cost of producing titanium alloy parts, many studies have been conducted in the field of titanium alloy powder metallurgy (PM) and specifically on the near-net-shaping of the Ti-6Al-4V alloy [2]. There is no need for metal re-melting and machining process since PM directly produces a final product from powder. South Africa has abundant titanium mineral reserves (near 20% of world reserves), but these reserves do not contribute directly towards to titanium metal or value-added titanium product [3]. In order to extend this field in South Africa, Centre for Materials Engineering (CME) has focused on PM compaction processes for producing titanium alloy final product. The direct powder rolling process is one of the powder metallurgy (PM) compaction processes that produce the long compact metal powder strip or plate.

The achievement of this work is able to provide a quality prediction of the direct powder rolling compaction process, and can be extend to design an optimal rolling mill and operating setups for desired metal powder compacted sheet or strip. Providing a guideline for further developing titanium alloy and related metal strip from direct powder rolling route.

1.3 Objectives of the Dissertation

Although the primary interest of this work involves CP-titanium powder, stainless steel 316l powder was included in the study to avoid excessive wastage of titanium powder during the early stages of the parametric study.

This research aims to achieve the following:

- Determine the powder characteristics of stainless steel and CP-Titanium powders by conducting uniaxial pressing test, shear test and wall friction test.
- Implement the Johanson’s powder rolling model and simulate the powder rolling performance in terms of rolling pressure by importing measured powder characteristic parameters and the CME rolling mill geometry dimensions.

- Conduct a parametric experimental study on various setups of powder rolling parameter combinations including roll gap, roll face width, rolling speed and powder feeding rate on both stainless steel 316L and CP-titanium powder.
- Validate the predicted Johanson's model results with the measured experimental data in terms of relative density of rolled strips.
- Investigate the contribution of sintering process, plastic deformation and recrystallization on the relative density and mechanical properties of different CP-titanium strips.

1.4 Scope and Limitations

This dissertation investigates the influence of powder rolling and operational parameters effects (rolling speeds, roll gap size, roll surface width and feeding rate) on the integrity of the compacted stainless and CP-titanium metal powder strip. Rolling speeds were only investigated at 10, 12 and 14 rpm due to the maximum capability of the CME rolling mill. The roll gaps were fixed at 1.5 mm, 1 mm, and 0.5 mm. The roll surface widths were investigated at 14 mm, 65 mm, 85mm, and 100 mm. The hopper outlet diameters of 1.5 cm, 2.0 cm and 2.5 cm were used. The fed powder material was only used 200 ml for each trial. The relative density calculated and presented in this dissertation was calculated as a percentage of the theoretical full densities of CP-titanium (4.51 $\mathrm{g/cm^3}$) and stainless steel 316L (7.90 $\mathrm{g/cm^3}$) [36]. The feed pressure was only estimated according to the data from Simon and Guigon [32].

The particle size and shape effect of direct powder rolling process was not investigated in this thesis. Due to compacted powder strip dimensional limitations, the tensile test was only conducted by using standard subsize specimens. The contamination and oxygen content of processed CP-titanium powder rolled strip was not investigated in this dissertation.

1.5 Plan of Development

This dissertation will begin with a literature review in chapter 2 and the experimental methodology will be presented in chapter 3. The results and discussion of the direct powder rolling model implementation and subsequent experimental direct powder rolling results are presented and discussed in chapter 4. In chapter 5, the as-sintered and post-deformation annealed conditions of CP-titanium powder rolled strip are presented and discussed. In chapter 6 and 7, the conclusions and recommendations of this research are given, followed by a list of references and the appendix.

Chapter 2

Literature Review

2.1 Titanium

2.1.1 Introduction

A new metallic element was discovered in black magnetite by an English clergyman W. Gregor in 1791. Four years later, one German chemist M.H. Klaproth also found this element in a study of rutile and named this element as titans (son of Greek god Uranus and Gaea, also known as giant). In 1910, United States scientist M.A. Hunter was the first to extract pure titanium by reducing titanium tetrachloride ($\mathrm{TiCl_4}$) with sodium. In 1932, Luxembourg scientist W.J. Kroll fabricated large quantities of pure titanium by combining $\mathrm{TiCl_4}$ with calcium. After eight years, W.J. Kroll successfully fabricated malleable sponge titanium through $\mathrm{TiCl_4}$ reduction process by changing the reducing agent from calcium to magnesium. Since then, he was recognized as the father of titanium industry. Subsequently, Kroll fled to the United States due to the outbreak of the Second World War and successfully achieved titanium industrialization through the U.S. Bureau of Mines. This method is still widely used in today's titanium industry and is known as 'Kroll process'. Therefore, the element of titanium was found in the 18th century, but it was only extracted as pure state in 1910 and the titanium industrialization was successfully achieved after 1940s [4].

After the Second World War, the titanium-based alloys became an indispensable material for jet aircraft due to its excellent corrosion resistance and high specific strength. In 1948, the company of DuPont was the first to produce titanium commercially. A large amount of titanium and its alloys are mainly consumed in the aerospace industry [5]. Additionally, marine, chemical industry, architecture and telecommunications equipment have an increasingly wide range of applications. Further, titanium can be used as artificial bone since it also has outstanding compatibility with the human body [4].

Titanium is not actually a rare substance as it ranks as the ninth most plentiful element and the fourth most abundant structural metal in the earth. Unfortunately, it is only able to be found compound and is never found in a pure state. Thus, the difficulty is in processing the metal and makes it expensive. Even today it is produced only in a batch process, and no continuous process exists as for other structural metals [4].

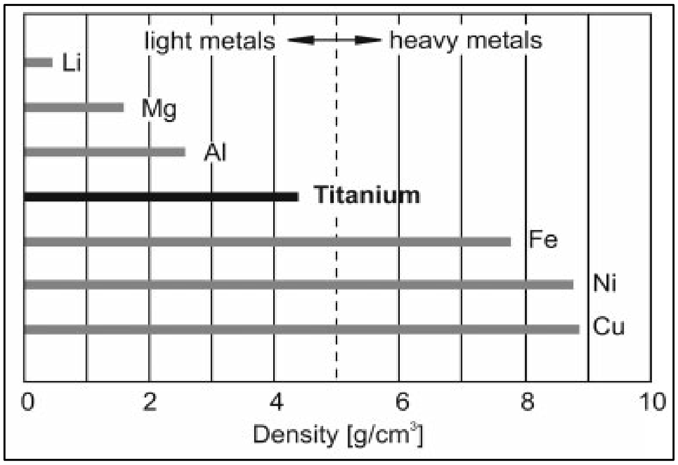

Figure 2.1: The specific weight of various metals [5].

Metals vary substantially in weight. At 0.5 $\mathrm{g.cm^{-3}}$ Lithium has the lowest density while Osmium and Iridium are the heaviest metals with a density of 22.5 $\mathrm{g.cm^{-3}}$ (see Figure 2.1). The separating point between light and heavy metals is 5 $\mathrm{g.cm^{-3}}$, and titanium with a density of 4.51 $\mathrm{g.cm^{-3}}$ is treated as the heaviest light metal. Although twice as heavy as the classic light metal aluminum, it still has only about half the specific weight of iron or nickel. The advantage that titanium has over aluminum is that titanium alloys can often be used at temperatures exceeding 500 °C, whereas 130 °C is given as the general maximum operating temperature for conventional aluminum [6,7].

2.1.2 Alpha and Beta Titanium

Titanium exists in various crystal structures, which are only stable within specific temperature ranges. Pure titanium and most of titanium alloys exist in hexagonal close packed (hcp) structure at low temperature, which is called Alpha α-titanium. However, the body- centered cubic (bcc) structure is transformed when the temperature exceeds $882 \pm 2^\circ\mathrm{C}$ [8]. The temperature at which α titanium has no longer existed and α crystal structure is fully transformed β phase microstructure is called the transus or β-transus temperature. In particular, the transus temperature is not fixed and varies according to the purity of titanium and element content of titanium alloys. The atomic unit cells of the hcp α titanium and the bcc β titanium are schematically shown in Figure 2.2 below.

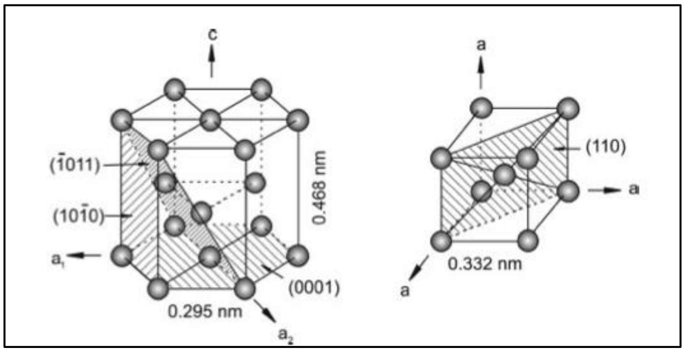

Figure 2.2 Crystal structure of hcp α titanium and the body centered cubic (bcc) β titanium [6].

The deformability and diffusion rate are mainly determined by the titanium crystal structure [6]. In general for metals, the deformability increases from the hexagonal close packed lattice to the body centered cubic to the face centered cubic lattice. As described by Leyens and Peters [6], the β phase titanium is easier to undergo plastic deformation than α phase titanium. The number of slip systems describes the deformability of different crystal structures. This term is determined by the number of slip planes multiplied by the number of slip directions. Hence, there are 3 slip systems for the hcp structure and 12 of slip systems for the bcc structure. These highly dense packed atom planes and directions are energetically more favorable for plastic deformation. Therefore, the denser the slip plane, the easier it is the dislocation to move.

2.1.3 The Classification of Titanium Alloys

The alloying elements of titanium can be classified as neutral, α-stabilizers and β-stabilizers (see Figure 2.4). All of these classified alloying elements influence the transus temperature. Neutral alloying elements (Sn, Zr) do not have significant influence on the transus temperature. α-stabilizing elements (Al, O, N, C) expand the α phase field to a higher transus temperature and β-stabilizing elements (Mo, V, Fe, Mn, Cr, Cu, H) pull the β phase field to a lower transus temperature. Both α and β stabilizing elements develop an intermediary α+β field on the phase diagrams of titanium alloys. In addition, β-stabilizers can be subdivided into β-isomorphous and β-eutectic elements. β-isomorphous elements (Mo, V, Ta, Nb) are more important due to its high solubility in titanium, conversely the β-eutectic elements (Fe, Mn, Cr, Co, Ni, Cu) have very low solubility in titanium and intermetallic compounds are formed.

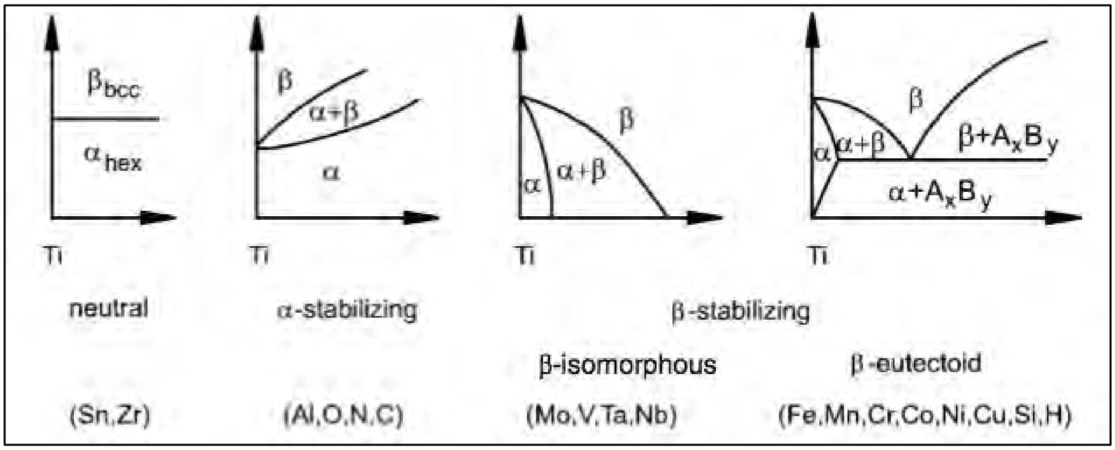

Figure 2.3 Influence of alloying elements on phase diagram of Ti alloys [6].

For further concerns, the phase fields can be subdivided into near- α and metastable β alloys. The three dimensional phase diagram which is combined two phase diagrams with an α-stabilizing element and a β-stabilizing element of respectively (see Figure 2.3). Refer to this diagram, the α alloys are made up of commercial pure titanium and α-stabilizing elements. The near- α alloys are reached when less than 5% fraction of β-stabilizing elements are added. Moreover, the α+β alloys are reached by increasing volume fraction of β-stabilizing element in the range of 5 to 40%. The metastable β alloys are reached in the α+β phase field when the volume fraction of β-stabilizing element is further increased to a level where β alloys no longer transform to martensite by fasting cooling [4, 6].

2.1.4 Phase Transformations of Ti-6Al-4V

This alloy is an α + β alloy, with 6 wt% aluminum stabilizing the α phase and 4 wt% vanadium stabilizing the β phase. At room temperature, the beta to alpha transformation of this alloy is not completed, resulting in approximately 10% by volume fraction of β phase. In the titanium alloy of Ti-6Al-4V, the β-transus temperature is approximately 995°C (1268K), which is influenced by impurities and oxygen content [10]. Depending on cooling rate and prior heat treatment the beta phase may transform into a variety of alpha phase morphologies. The α morphologies include allotriomorphic and widmanstatten α, massive α, and martensitic α. According to certain cooling rates, these transformation products are given in Table 2.1.

Table 2.1: Characteristics of the β -> α+ β Transformation in Ti-6Al-4V [9].

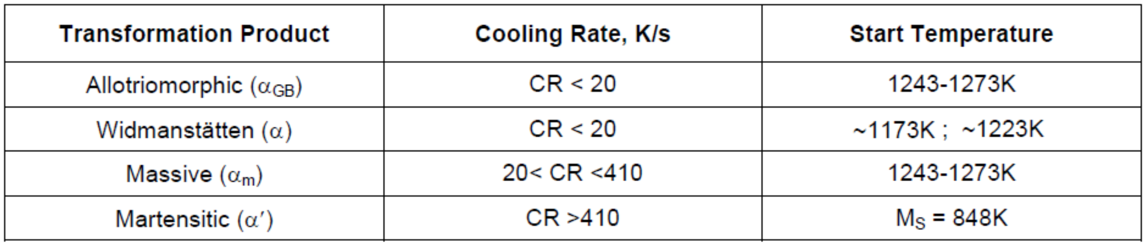

Transformation Product	**Cooling Rate, K/s**	**Start Temperature**
Allotriomorphic (α_{GB})	CR < 20	1243-1273K
Widmanstätten (α)	CR < 20	~1173K ; ~1223K
Massive (α_m)	20< CR <410	1243-1273K
Martensitic (α')	CR >410	M_S = 848K

For very slow cooling rates from high up in the α + β region or above the β-transus temperature (995°C ± 20°C) the β phase mainly transforms into a primary α. The α nucleation rate is increased in the β grain boundaries by increasing the cooling rate thereby enhancing the formation and growth of α platelets in to the prior β grains. The length and width of these α platelets are determined by the cooling rate; an increased cooling rate enhancing the nucleation rate and slowing the diffusion process. At a certain point, the cooling rate is fast enough for nucleation of α to occur inside the prior β grains as well, and leading to the formation of the basketweave structure. Finally, if quenched, the β phase will fully or partly transform into a martensitic α. This martensite exists in two different forms, α '(α prime / hexagonal martensite) phase having hexagonal structure and α "(α double prime / orthorhombic martensite) phase having an orthorhomibic crystal structure [11]. The type and amount of α ' and α " formed upon quenching depends on the chemical composition of the β stabilizers existing at temperature prior to quenching. The β phase experiences large compositional variation, which is reflected in significant mechanical property changes [12]. Vanadium content of the β phase occurs in proportion to the reduction of the volume fraction of β phase. At vanadium contents ≥ 15 wt%, the β phase is stabilized and retains its bcc crystal structure upon quenching. When vanadium contents of 10 ± 2 wt%, the β phase is quenched (from a temperature range of approximately 750-900°C), it partly retains the bcc structure and partly transforms into soft orthorhombic α " matensite. The higher the solution heat treatment temperature, the smaller is the vanadium enrichment in the β phase, leading to transformation into hexagonal α ' upon quenching (from temperatures above 900°C) [10,13].

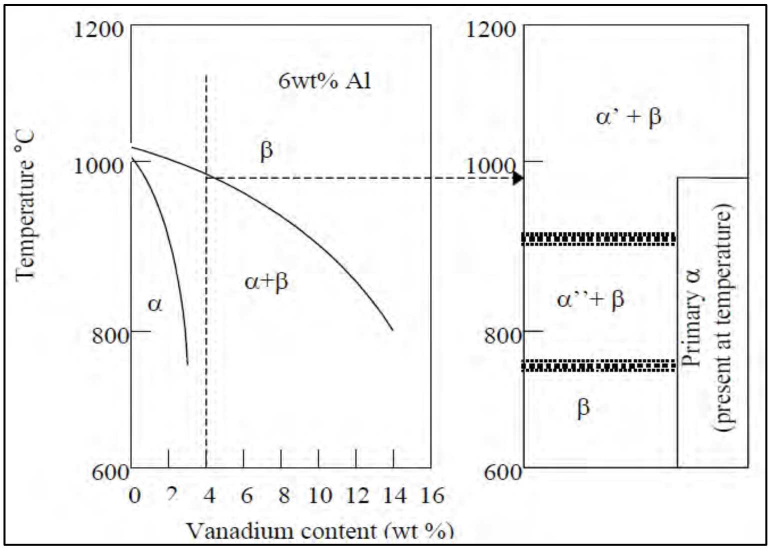

Figure 2.5: A schematic illustration of microstructures occurring in Ti-6Al-4V after quenching from different temperatures [10].

A schematic illustration of the microstructures resulting from quenching from various temperatures is given in Figure 2.5. This figure attempts only to illustrate the principle transformations on quenching; in reality mixtures of both α ', α " and metastable/stable β can occur, depending on elemental compositional variations. The grain boundary allotriomorph α phase starts to form when the temperature drops below the β transus temperature. And then it continues to grow along β grain boundaries depending upon the cooling rate.

2.2 Powder Metallurgy

2.2.1 Introduction

Pressing metal is mature technology since the old civilization. In 1920s, the modern powder metallurgy (PM) technology achieved the mass production of porous bronze bushes for bearings and tungsten carbide odes. During World War II, further development of powder metallurgy occurred in a great variety of ferrous and non-ferrous materials in manufacturing. In 1960s, Powder metallurgy was growing more rapidly mainly due to its potential factors, which included economical processing and unique properties. Primarily, the powder metallurgy process is efficient, economical and effective for manufacturing high precision product from powder. Moreover, there are some relevant consolidation processing techniques such as powder rolling, powder extrusion, powder compaction and Hot Isostatic Pressing (HIP) [5]. The flow diagram indicating the PM processing was illustrated in Figure 2.6.

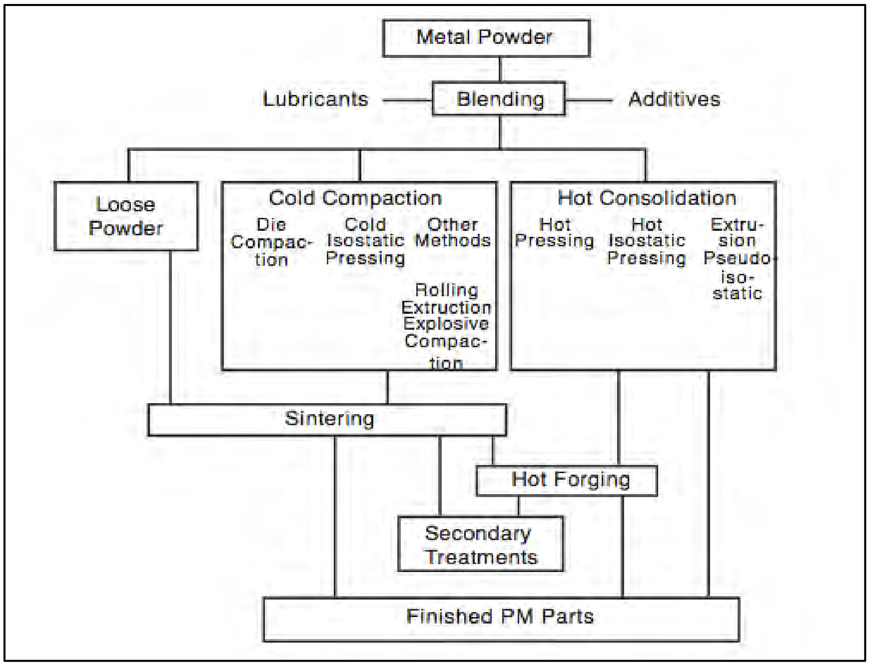

Figure 2.6: The flow diagram of powder metallurgy processing [5].

In the past decade, high performance new types of powders allow production of larger and high strength materials by the significant advances in powder fabrication technology. Nowadays, the size of PM parts has become many times larger. Higher density and mechanical properties has been developed by using new alloying elements through improved heat treatment process [5].

2.2.2 Reasons for Using Powder Metallurgy

PM processing as an advanced manufacturing method is more competitive than other conventional methods like casting, forging, pressing and machining. A particular group of PM processes (e.g. CIP, HIP) is one of the solutions when the required strength, wear resistance and operational temperature exceed the capabilities of casting alloys.

Conventional casting and forging processes often result in non-uniform microstructure distribution. Full dense high performance alloys with uniform microstructure can be achieved by careful control of powder particles and PM processing [5].

Another advantage for the PM approach is that of its near-net-shape (NNS) ability. NNS refers to the production of parts that are very near to their final dimensions once produced, with a minimum of machining still required before the final part is complete. As a result of this, PM techniques are very material efficient using only the material that is required and reducing the expense associated with machining [14].

2.2.3 Powder Characteristics

The quality of PM product is mainly dependent on the metal powder characterization. Powder fabrication methods influence the chemical and physical structures of metal particles and the particle size distribution. The characterization of powder also influences the composition and microstructure of sintered material during compaction and sintering processes. One simple summary of characterization of various powder properties is given in Table 2.2.

Table 2.2: Summary of various powder properties and measuring methods [5].

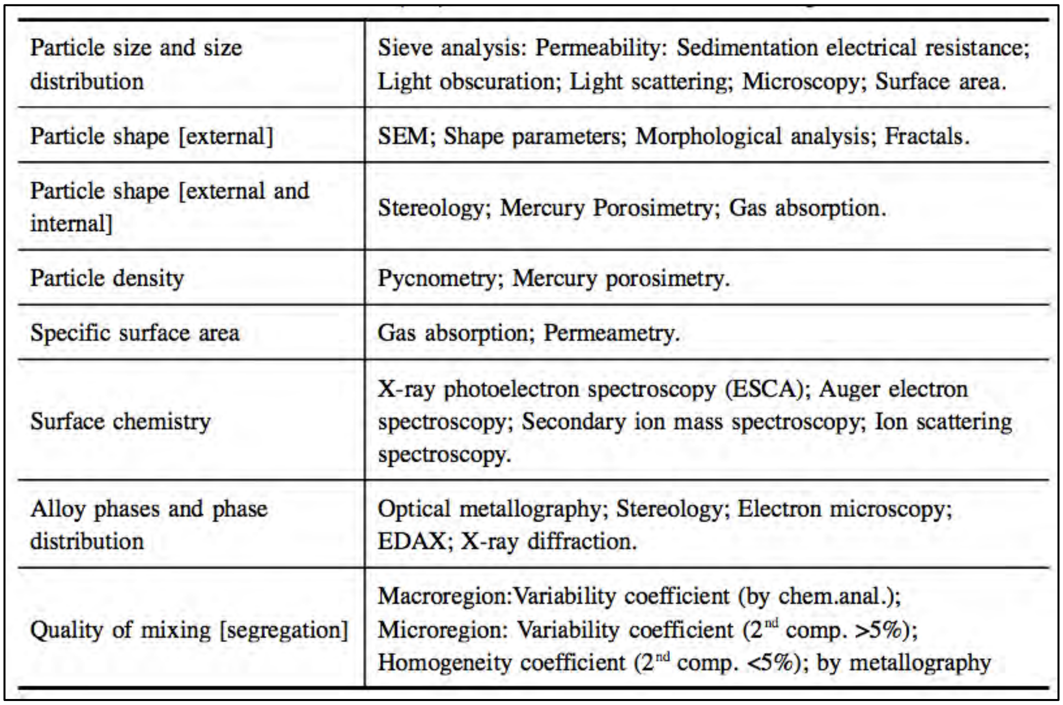

Particle size and size distribution	Sieve analysis: Permeability: Sedimentation electrical resistance; Light obscuration; Light scattering; Microscopy; Surface area.
Particle shape [external]	SEM; Shape parameters; Morphological analysis; Fractals.
Particle shape [external and internal]	Stereology; Mercury Porosimetry; Gas absorption.
Particle density	Pycnometry; Mercury porosimetry.
Specific surface area	Gas absorption; Permeametry.
Surface chemistry	X-ray photoelectron spectroscopy (ESCA); Auger electron spectroscopy; Secondary ion mass spectroscopy; Ion scattering spectroscopy.
Alloy phases and phase distribution	Optical metallography; Stereology; Electron microscopy; EDAX; X-ray diffraction.
Quality of mixing [segregation]	Macroregion:Variability coefficient (by chem.anal.); Microregion: Variability coefficient (2^{nd} comp. >5%); Homogeneity coefficient (2^{nd} comp. <5%); by metallography

The content of impurity elements in the metal powders or bulk solid materials can influence the processing and the properties of the final product considerably. It is very important to understand whether such elements exist in the form of their elements or whether they exist in the form of a chemical compound. One example from G.S. Upadhyaya's book [5], in reduced iron powder, silicon is present as impurity in the form of silica and other ceramic and inert compounds may exist as well. These may be reported in terms of an acid-insoluble matter, the effect of impurity elements on the hardness of the particles and the degree of chemical reactivity during sintering will differ widely, depending on their actual form [5].

The hydrogen loss is another common parameter that is used to measure the level of oxygen impurity in metal powders oxides, which are easily reduced by hydrogen. However, this measured value can be inexact because of the incomplete reduction of oxides. Thus, annealing the metal powders in an inert-gas atmosphere is an effective way to reduce its oxygen content. The formation of metal oxides may influence the compaction and sintering. In the worst scenarios, metal oxides can remain in the sintered materials. As the particle size decreases (larger surface area) it will cause a large amount of oxygen adsorption and with increasing surface chemical activity [5].

The microstructure of metal powders has a significant impact on the behavior of powder compaction and sintering and on product performance. Fine grain size is always desirable, not only because it improves the performance and uniformity of its product, but also it gives better mechanical properties [5].

G.S. Upadhyaya described that the grain size in the metal microstructure can be dependent on the powder particle size. The particular powder production method such as rapidly cooled powder, would naturally give rise to small particles and also small grain sizes. Pre-alloyed (PA) powders may contain various phases depending on their exact composition, the appropriate phase diagram, their thermal history and the method of powder production used [5].

Particle Size and Shape

The powder particle shape is another characteristic which can be determined by measuring its contour surface. The current recognized system to categorize powder shape characteristics and its fabrication methods is given in Figure 2.7. Spherical powder is the simplest one and ideal shape. Unlike spherical powder, the irregular shape is more complicated to measure its size and it has a large surface area and friction during compaction. The porous powder is even more difficult to define its size and shape characteristics since it has large amount of porosity.

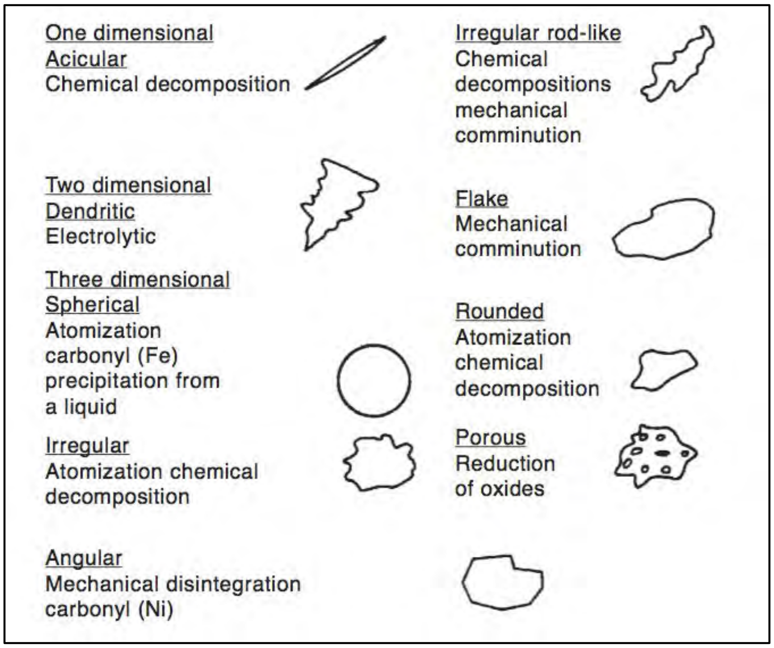

Figure 2.7: Categories of various powder shape characteristics [5].

Consider the particle shapes in Figure 2.8. The powder can be described as rounded and irregular in shape. However, such description is still not convincing. Thus some possible size measurements for characterizing the particle shape in the figure below.

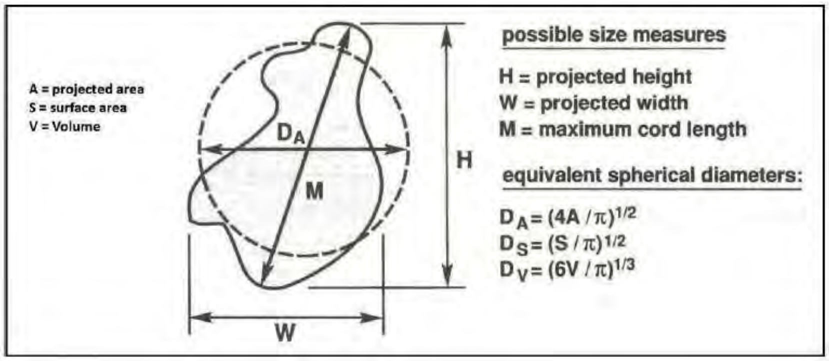

Figure 2.8: The projected image of a rounded but irregular particle. Six possible measures of particle size are shown [13].

In reality, although the same method is used to prepare the powder under mass production, all the powder cannot be the exact same size. Size distribution is therefore used to describe the size characteristics of powder. In Figure 2.9, Particle size distribution curves relate the particle size to the corresponding fraction of the powder with that size [13].

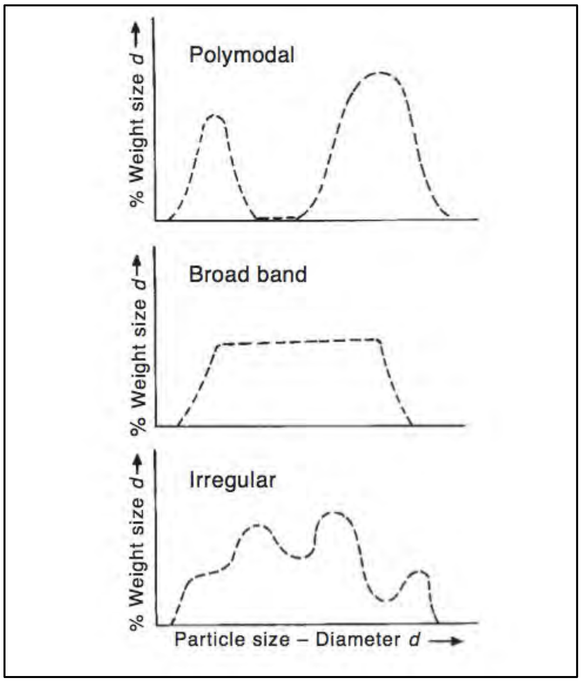

Figure 2.9: schematic illustrations of some realistic particle size distributions [5].

Measurement Techniques

Screening is the most common technique to distinguish particle sizes. A square shape of grid spaced wires is given in Figure 2.10. The mesh size depends on the number of wires per unit length. The opening size decreases with increase in mesh size number. In other words, 200 meshes indicate 200 wires per inch. For each mesh, the wire has a diameter of 52 um and the remaining opening size is 75 um. However, the limitation of the screening technique is that it cannot measure the mesh size smaller than 38 um. The powder passing through a mesh is designated by a – sign and that retained on a mesh is designed by a + sign. For example, -100 to +200 mesh powder would be passed through a 100 mesh screen but not a 200 mesh screen and the particle size would be between 150 and 75um. Although screening is widely used in particle size analysis, it has a 3-7% permissible variation in average opening size as a manufacturing tolerance [13].

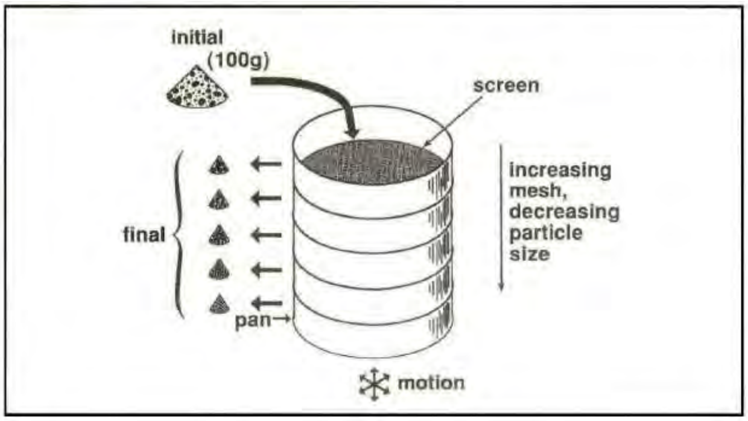

Figure 2.10: Schematic representation of screening process to analysis particle sizes [13].

Table 2.3: Standard mesh size on screening technique [5].

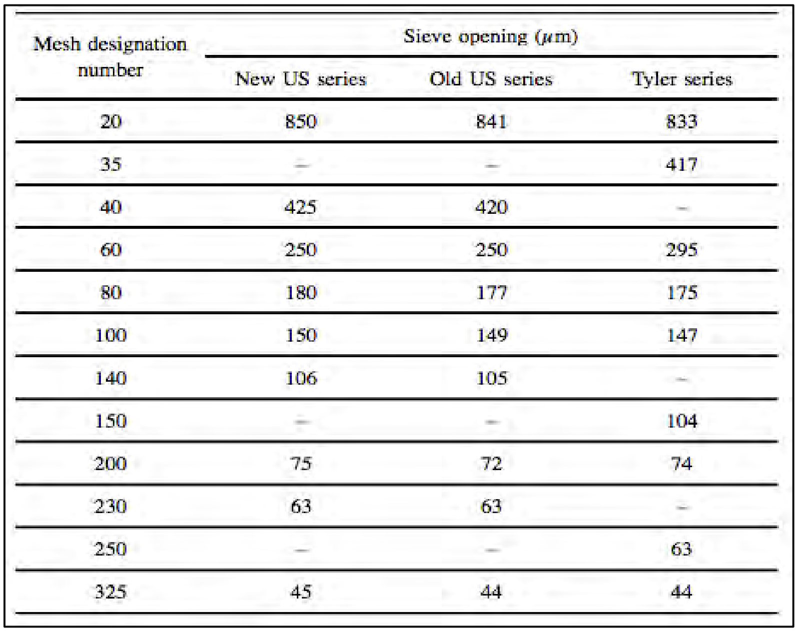

Mesh designation number	Sieve opening (μm)		
	New US series	Old US series	Tyler series
20	850	841	833
35	–	–	417
40	425	420	–
60	250	250	295
80	180	177	175
100	150	149	147
140	106	105	–
150	–	–	104
200	75	72	74
230	63	63	–
250	–	–	63
325	45	44	44

There are a number of other particle size measurement techniques available in powder metallurgy, but each has its own limitations. Table 2.4 classifies some of the common methods of particle size determination and their limits of applicability.

Table 2.4 classifies some of the common methods of particle size determination [5].

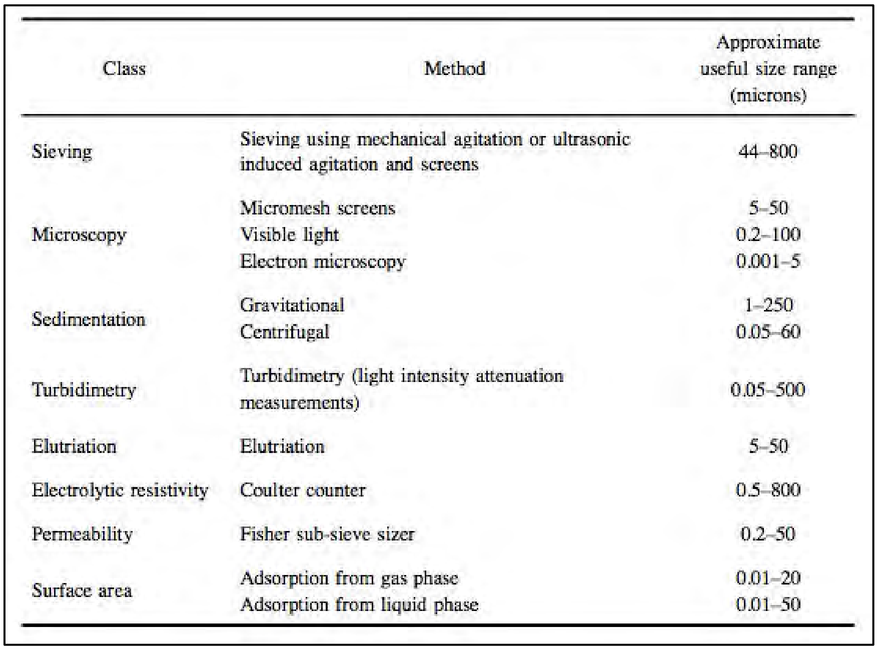

Class	Method	Approximate useful size range (microns)
Sieving	Sieving using mechanical agitation or ultrasonic induced agitation and screens	44–800
Microscopy	Micromesh screens Visible light Electron microscopy	5–50 0.2–100 0.001–5
Sedimentation	Gravitational Centrifugal	1–250 0.05–60
Turbidimetry	Turbidimetry (light intensity attenuation measurements)	0.05–500
Elutriation	Elutriation	5–50
Electrolytic resistivity	Coulter counter	0.5–800
Permeability	Fisher sub-sieve sizer	0.2–50
Surface area	Adsorption from gas phase Adsorption from liquid phase	0.01–20 0.01–50

Green Strength

Green strength is one significant mechanical property to describe the capability of compacted powder to maintain its size and shape during handling without any heat treatment. The definition of green strength is the mechanical strength of unsintered powder compact and is generally measured by transverse rupture strength or three point bending testing.

Table 2.5: Summary of relationship between powder characteristics and green strength

Green Strength	**Particle surface roughness**	**Powder surface area**	**Powder apparent density**	**Compaction pressure**	**Surface oxidation and contamination**
Increase	Increased	Increased	Decreased	Increased	Decreased
Reason	More space for mechanical interlocking	Increasing the irregularity	More interlocking and reducing the particle size	More force to enforce interlocking	Reducing brittle oxides

G.S. Upadhyaya [5] introduced that the standard green strength test is the transverse bend test of a 12.7 by 31.7mm rectangular green specimen with a thickness of 6.35 mm. It is the stress calculated from the flexure formula which is required to break the specimen and as follows

$$\text{Green strength} = \frac{3PL}{2wt^2}, \mathrm{N/mm^2} \qquad [5]$$

Where P is the breaking load, N; L is the distance between the supporting rods, mm; t is the specimen thickness, mm; w is the width of specimen, mm.

Apparent and Tap Density

Apparent density or bulk density of powder is the density when the powder is in the loose state without applied load and is often expressed in mass per unit volume. This parameter determines the size of compaction die, transport equipment, and the behavior during sintering. Other factors also directly influence the apparent density that is the solid material density, particle size , shape and surface area [5].

G.S. Upadhyaya [5] described that apparent density is determined by the Hall flowmeter, where a container of known volume is completely filled by flowing metal powder through a Hall funnel (see Figure 2.11). The apparent density can be obtained from the mass of the powder divided by the funnel volume.

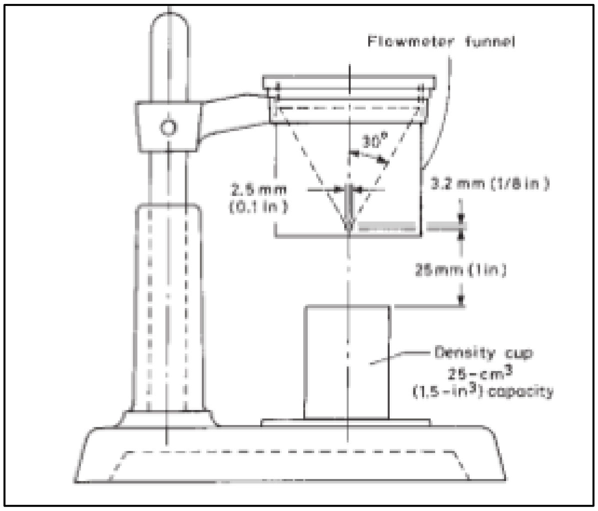

Figure 2.11: Hall flowmeter [5].

Tap density is the highest density that can be reached by mechanical vibration without external pressure. The amount of increase in density due to tapping depends on the particle internal friction. The greater the frictional conditions in the original powder (small sizes, irregular shapes and roughened surface), the greater the increase in density due to tapping [5].

Flowability

Flowability or flow rate has played a critical role in powder compaction and it mainly depends on the adhesive forces between individual particles. For fine and dry bulk particles, the van der Waals interactions play the essential role of the adhesive forces. Conversely, in moist bulk particles, liquid ‘bridges’ are formed by small regions of liquid in the contact area of particles, which causes low capillary pressure due to surface tension. Thus, the moist bulk particles have poorer flowability than the dry bulk particles [15].

Whether a particle flows fast or slowly depends on the relationship of the adhesive forces and the other forces acting on the particles. It can be indicated that the influence of adhesive forces on flow behavior increases with decreasing particle size. Therefore, a bulk particle flows more slowly with decreasing particle size and vice versa [15].

If particles are compressed against to each other by external forces, the compressive force plays another major role for raising the adhesive force. Thereby large stresses exist locally at the particles' contact points due to the small contact points. This causes plastic deformation of the particles in the contact area. Thus, the adhesive forces are increased by the compressive force acting on a bulk particle [16].

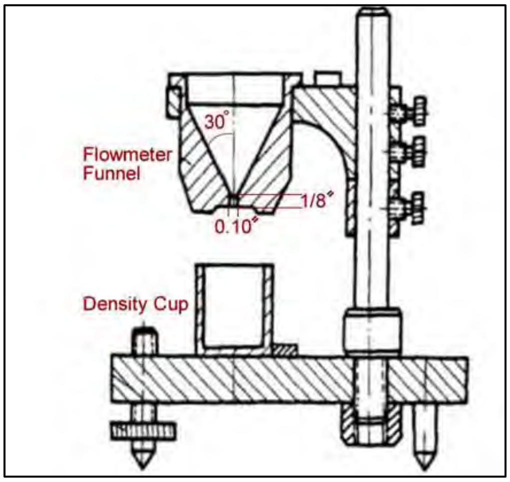

Figure 2.12: Hall Flow Meter [5].

Flow rate is usually determined by the time for 50 g of powder to flow through the Hall flowmeter (see Figure 2.12). The fine powder flows slower than the coarse powder since the small particle size offers large surface area. In other words, the higher apparent density gives a low flow rate [5].

Compressibility

One of the main uses of metal powder in PM is to compact the metal powder into desired shapes, so that powder compaction behavior is another important metal powder characteristic. Compressibility is defined as the ability to densify a powder under a specific known applied load. In order to measure this property, a die is filled with powder and the density is measured after compaction at a specified compaction pressure. Typically, one cylinder or rectangular test specimen is used. Powder compressibility depends upon various factors such as powder hardness, particle shape, internal porosity, particle size distribution and contaminations [5].

The compressibility can be described in the equation as follows:

$$\text{Densification parameter} = \frac{\text{Green density} - \text{Apparent density}}{\text{Theoretical density} - \text{Apparent density}} \qquad [5]$$

Generally, compressibility is directly proportional to the apparent density. Another term of compression ratio (CR) is described in German's book [13] which is the ratio of the volume of loose powder to the volume of the compacted powder. This parameter is very useful for the tool design [13].

$$C_R = \frac{V_L}{V_C} = \frac{\rho_g}{\rho_a} \qquad [13]$$

Where V_L is the volume of the loose powder, V_c is the volume of the compacted powder, ρ_g is the green density, and ρ_a is the apparent density. A high interparticle friction will give a low initial density, but other factors such as particle size and lubrication will influence the compact density.

2.2.4 Powder Fabrication

Nearly most metals can be transformed into powder particles, but the fabrication method used to create that powder depends on the particular material properties of the metal. Metal powder production methods can be classified as follows:

- Chemical methods
- Physical methods
- Mechanical methods
- Atomization methods

The chosen method must be related to the application and the desired properties and structure of the final product.

Mechanical production techniques

There are four fundamental mechanical processes including impaction, attrition, shearing and compression. Impaction is the process that applies rapid impact to the material thereby causing cracks in order to achieve size reduction. Attritioning reduces powder size by a rubbing motion. Shearing forms a cleavage type of fracture by cutting and then compressive force breaks the material in to powder. For powders in the millimeter size range, hammer mills are efficient, but for powders in the 1 to 100 um size range, stirred ball mills and other intense attrition devices are more appropriate. Powders produced by mechanical methods are typically irregular shape. The disadvantage of mechanical methods is that lack of control may include chemical contaminants, oxygen, oil and other metals [5].

Electrolytic production techniques

A powder can be precipitated at the cathode of an electrolytic cell under certain operating conditions. Metals formed into high purity powders by this method are palladium, copper, iron, zinc, manganese, and silver. The main advantage is that the electrolytic precipitation can provide high purity. The cycle begins with dissolution of the anode under an applied voltage in an electrolytic cell such as shown in Figure 2.13. Transport through the electrolyte is used to purify the deposit that forms at the cathode. The porous cathode deposit is removed, washed, dried, ground into fine powder, and annealed to remove any strain hardening [5].

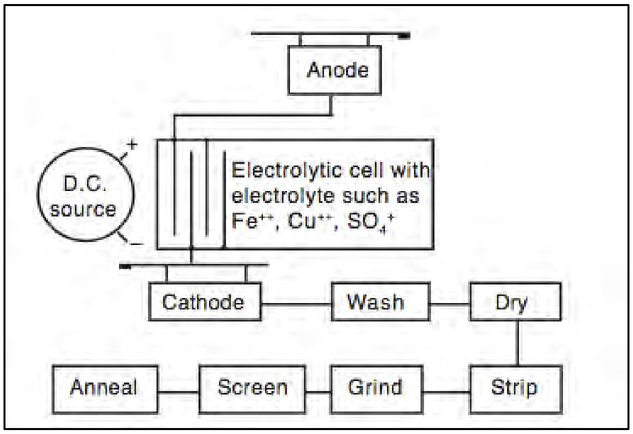

Figure 2.13: an electrolytic process for producing metal powder [5].

Powder formed by the electrolytic technique is often dendritic or sponge in shape, although considerable adjustability in particle size and shape is possible. The specific properties of the powder are dependent on the bath conditions during deposition and on the subsequent processing steps. Two examples of electrolytic copper powders are shown in Figure 2.14.

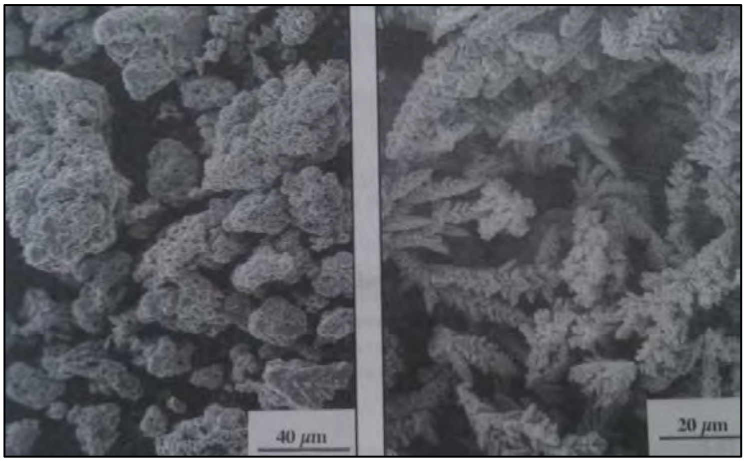

Figure 2.14: Two scanning electron micrographs (SEM) of electrolytic copper powders show typical sponge and dendritic shapes (Courtesy of J. Johnson) [13].

Although electrolytic production process is acceptable for pure powders, there are difficulties with the technique. Only elemental powders are practical. Contaminants can hinder the formation and deposition of powders at the cathode [5].

Chemical production techniques

Decomposition of a solid by a gas:

A common chemical fabrication of metal powder is oxide reduction. Oxide reduction is performed by thermo-chemical reactions that involve reducing gases such as carbon monoxide or hydrogen. This method often produces powder in sponge shape. In addition, high temperature processes can result in dense particles with polygonal shapes. The reduced powder is ground to fracture the interparticle diffusion bonds and to ensure the desired particle size. Annealing improves the final compressibility of the powder [5].

Decomposition of metal hydrides:

This process needs initial hydriding the metals like Ti, Zr, Hf, V, Th by heating the metal in the form of sponge, chip or turnings or even compact metal in hydrogen. TiH_2 is formed from titanium in the temperature range between 300–500 °C. These hydrides are very brittle and can be ball-milled into powder of the desired particle size. These then can be dehydrided by heating them in a vacuum atmosphere at the same temperature at which the hydride was formed [5].

Atomization production techniques

Atomization techniques can be classified into three categories which including gas atomization, water atomization. Both elemental and pre-alloyed powders are produced by these methods. The basic approach is to drive the molten metal through an orifice; the metal powder is formed from the melt by using a spray of droplets [5].

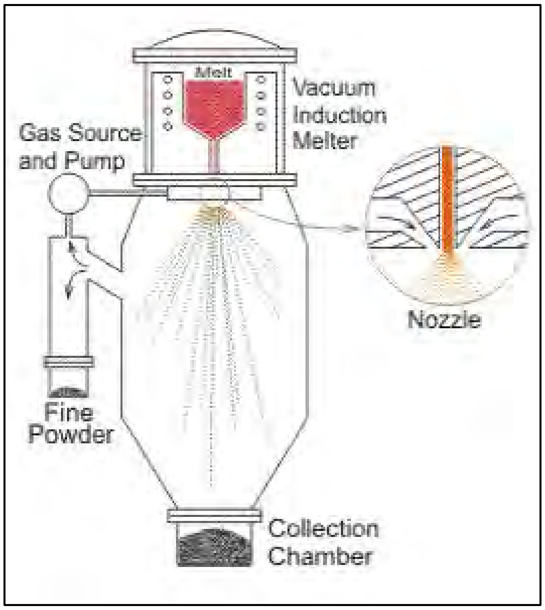

Figure 2.15: The schematic of gas atomization process

Gas atomization (see Figure 2.15) and water atomization techniques are similar fabrication processes which are capable to control the particle size and chemical properties. They are based on the principal of heating pure metal or re-melt metal alloys, and allowing the metal melt stream spilt apart into a fine spray by means of impacting it with high pressure gas or water. The fine spray is rapid cooled and solidified into fine metal powder particles [5].

2.2.5 Powder Compaction

Loose powder does not have higher density than the tap density without external pressure. Therefore, the external force is required to achieve greater density. There are several reasons for using powder compaction, they are:

- To compact the powder into desired shape
- To reduce the porosity of compact powder
- To improve the green strength for subsequent treatment

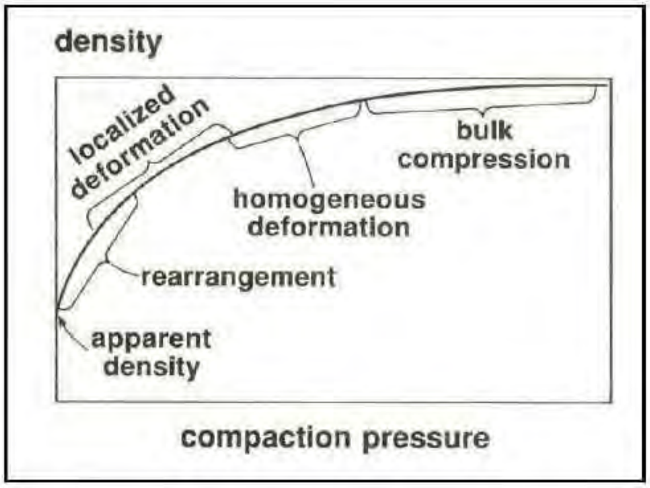

Figure 2.16: The pressure-density curve [13].

Four stages of power under compaction pressure are given in Figure 2.16 above. Initially a larger number of voids exist in the loose powders, which equal its apparent density. The highest density that can be reached at this stage is its tap density after vibration. The powder starts to rearrange with filling of large voids between particles after the pressure is applied, in which giving better packing arrangement. The porosity is decreased with increasing applied pressure which is shown in Figure 2.17.

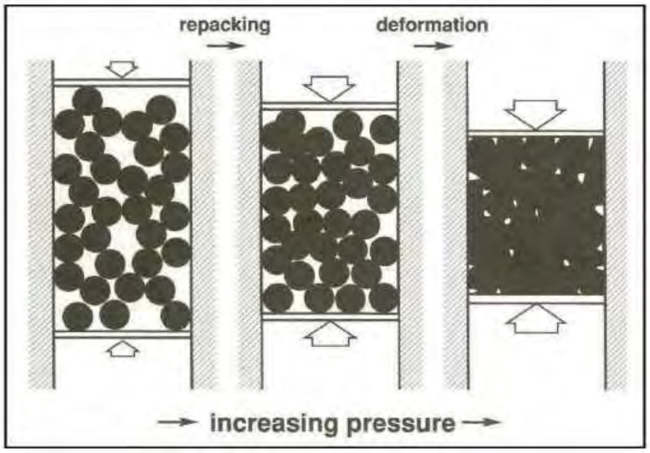

Figure 2.17: A schematic representation showing the densification mechanisms during uniaxial pressing [13].

The point contacts of powders initially undergo elastic deformation and a residual elastic energy is stored in the compact. The area of these contact surfaces enlarges and leads the plastic deformation and allows for new contact points to be appeared. At a certain pressure for specific material, the powder compact starts to reach its dense solid, and deforms as a bulk material or solid material. Further densification will not be occurred when exceeds this point [13].

2.2.6 Powder Uniaxial Compaction

Uniaxial powder pressing is the most conventional compaction method. This technique usually requires rigid die and hydraulic presses. The density of powder compact can reach up to 90% of its theoretical density under the compaction process. This technique is simple, efficient and easy for manipulate, but the mold design usually is relatively more difficult in terms of the shape of the powder compact. Typically, powders have different compaction behavior with fluids and the density of powder compact is often non-uniform. The compaction techniques are classified by the movements of the individual tool element's upper punch, lower punch and die relative to one another and can be divided into single action pressing and double action pressing [5].

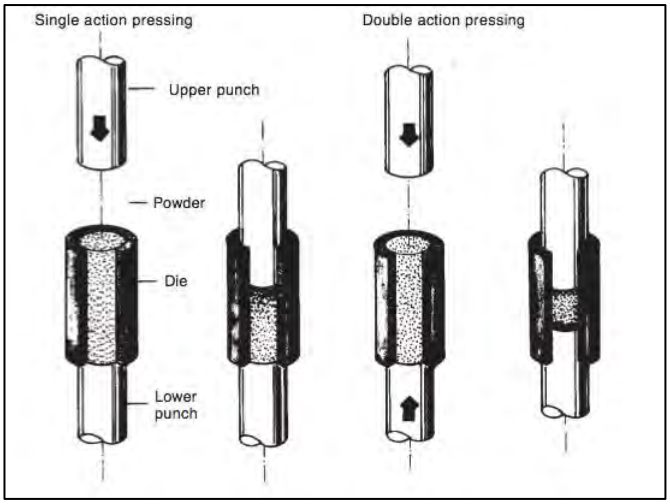

Figure 2.18: A schematic representation of both single and double action pressing [5].

This compacting mechanism in Figure 2.18 consists of the lower punch and the die which are both stationary. The upper punch moves into the die with filled powder to provide compaction force. The die wall gives the uniform pressure distribution. The density of top part of the compact is higher than the bottom part. In the double action pressing, only the die wall is stationary in the press. The upper and bottom punch move towards each other simultaneously into the die. The middle section of the compact is called 'neutral zone' which has the relatively low density [5].

The pressing sequence is listed as follows:

1. **Filling** – powder is filled into the die.
2. **Pressing** – pressure is applied into the die in order to press the loose powder into its compact.
3. **Withdrawal of the upper punch from the die** – there is a risk that cracking may occur in the green compact. When the upper punch releases the balance forces from the internal die ends, the elastic spring back force of the lower punch may cause danger.
4. **Ejection** – ejection must be well controlled to prevent any bending stress to break the green strength of compact by the ejection force.

Uniaxial Compaction Theory

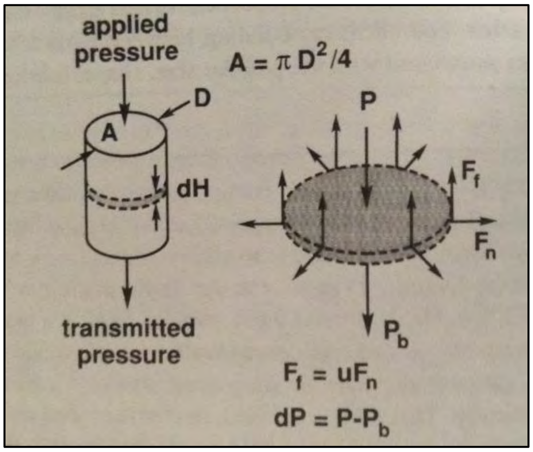

Figure 2.19: The balance of forces during die compaction [13].

The diameter D and height H of a powder compact are shown in Figure 2.19. Assume a slice section of height dH, when there is an external pressing force F, it shows that the pressure P on top of the thin element and that transmitted through the element bottom P_b will differ by the normal force acting against friction between powder and die wall. Thus, on this thin section the balance of forces along the axis can be expressed as follows:

$$\sum F = 0 = A(P_b - P) + \mu F_n \qquad (1\text{-}1)$$

Where F_n is the normal force, μ is the coefficient of friction between the powder and the die wall, and A is the cross sectional area. The normal force can be given in terms of the applied pressure with a proportionality constant z which varies with the compact density. The factor represents the ratio of the radial stress to the axial stress, thus

$$F_n = \pi \, z \, P \, D \, dH \qquad (1\text{-}2)$$

The friction force F_f is calculated directly from the normal force and coefficient of friction μ as,

$$F_f = \pi \, \mu \, z \, P \, D \, dH \qquad (1\text{-}3)$$

Combining terms gives the pressure difference between the top and bottom of the powder element dP as,

$$dP = P - P_b = -\frac{F_f}{A} = \frac{-4 \, \mu \, z \, P \, dH}{D} \qquad (1\text{-}4)$$

Integration of the pressure term with respect to compact height gives the pressure at any position x below the punch as follows:

$$P_x = P \, exp(\frac{-4 \, \mu \, z \, x}{D}) \qquad (1\text{-}5)$$

This equation 1-5 is applicable to a single action pressing and applies to the uniaxial pressing test for any powder in order to further calculate the compressibility of certain powder particles.

2.2.7 Metal Powder Rolling Compaction

Metal Powder rolling is essentially a continuous compaction process. It is the most important compaction method to produce metal plate or strip. Metal powder is fed from the hopper through the gap of two rolls in order to produce a continuous compacted green strip. The powder rolling mills are usually vertically arranged in order to improve powder flowability by its gravity. The subsequent sintering process was influenced by the quality of the direct rolled green strip in terms of its relative density. This section focuses on the impact of the rolling process and the characterization of metal powder on the quality of powder compacted strip, such as relative density and mechanical properties. A successful rolling compaction process depends on the following effects:

Particle shape – The ideal powder shape is to be very irregular since it has larger interlock forces than other shapes such as spherical particles.

Compressibility – Good compressibility offers large particle interlocking forces, which can lead to a relative density of at least 80 to 85%.

Particle Size – The fine particles offer less voids in compact green strip. In other words, the fine particle give higher packing density.

Surface Oxidation – This effect plays a significant role in powder rolling. Oxide often weakens the green strength during rolling. Thus, moisture and temperature must be well controlled during rolling compaction.

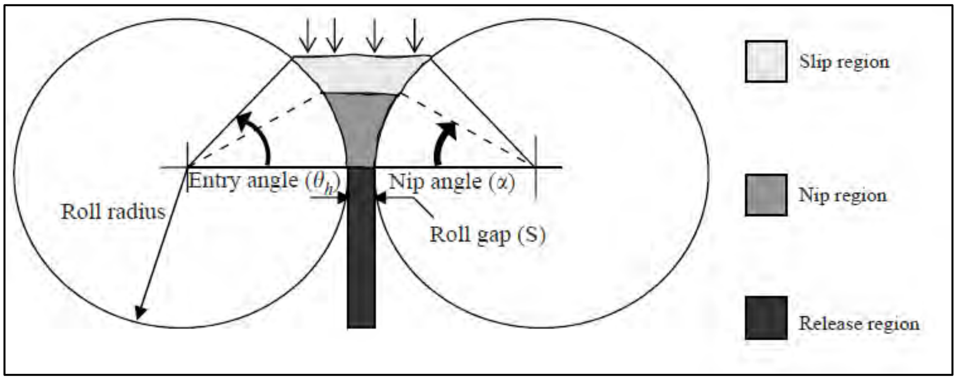

Figure 2.20: Zones of rolling compaction process.

The rolling compaction process can be described in to three regions as shown in Figure 2.20 above:

Slip Region– The powder is dragged by the frictional force of the roll surface and prepared for following compaction.

Nip Region – This region can be defined between the nip angle and the smallest roll gap, where the powder becomes coherent, the density increases rapidly and large amount of powder is dragged into the roll gap.

Release Region - is a region of a great decrease in pressure as the compact is ejected and can expand due to elasticity. As the material is pushed out of the nip region, it picks up speed and begins to move faster than the roller. This increase in speed causes slip in the opposite direction before the product finally loses contact with the roller [5].

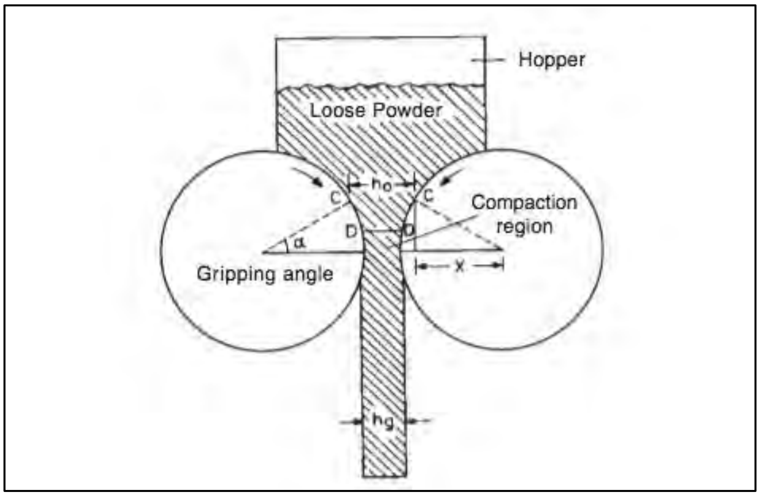

Figure 2.21: Schematic of vertically arranged powder rolling [5].

The thickness of the green strip which can be reached in powder rolling is determined by the roll diameter. The compaction length is related to the diameter of rolls (D) shown in Figure 2.21 above. The nip angle α for conventional metal rolling is the same for powder rolling (approximately 7 to 8°) [19]. The nip angle α is defined as:

$$cos\ \alpha = \frac{x}{D/2} \qquad (2\text{-}1)$$

According to further analysis of the rolling process, the relationship between the nip thickness h_0 and the thickness of rolled metal strip h_g can be expressed as,

$$h_0 = D\,(1-\cos\alpha) + h_g \tag{2-3}$$

The following assumptions are described as below:

1> Metal powder loss is negligible and the rolling process must be continuous without any slipping between green strip and rolls.

2> The density of rolled green strip is uniform distributed when the rolling parameters are constant.

3> The width of feeding metal powder is equalized with the width of rolled green strip.

According to the law of mass conservation and the assumption 1 and 2 made above, the mass flow equation can be expressed as,

$$\rho_{in} \cdot h_0 \cdot V_{in} \cdot B = \rho_{out} \cdot h_g \cdot V_{out} \cdot b \tag{2-4}$$

Where ρ_{in} is the relative density of the powder before rolling, B is the width of feeding zone, V_{in} is the powder feeding rate, ρ_{out} is the relative density of rolled strip, b is the width of green strip, V_{out} is the output speed of the rolled green strip.

From assumption 3, and B = b. Hence,

$$h_g = \frac{V_{in} \cdot h_0 \cdot \rho_{in}}{V_{out} \cdot \rho_{out}} \tag{2-5}$$

Let

$$S = \frac{V_{in}}{V_{out}} \tag{2-6}$$

Where S is the ratio of extension, which is associated with the rolling speed and the characteristics of metal powder. This quantity of S is relatively difficult to be measured, but generally it has a value of 1.00 – 1.02 [20].

$$C = \frac{\rho_{in}}{\rho_{out}} \tag{2-7}$$

Where C is the compression ratio (CR), which is influenced by the compressibility of the metal powder.

Substituting equations of (2-3), (2-6), (2-7) to (2-4).

Hence,

$$h_g = \frac{D(1 - \cos\alpha)}{CS - 1} \tag{2-8}$$

This equation is only able to describe the relationships between the roll diameter and the thickness of the green compact strip. It does not cover the interaction between the density of the green strip, roll press dimensions, material characteristics and the operating parameters such as roll face width, powder feeding rate etc. However, the question also can be asked if the nip angle (7 to 8°) whether is a reliable value or not since the angle was also defined as that it can be varied from 7 to 33° depending on the material in Johanson's theory [21].

In summary, the various factors which affect the direct powder rolling process were listed in the Table 2.6 below.

Table 2.6 Relationships between factors and calculating parameters during rolling process

Rolling Parameters	Factors of Rolling Process
μ	Roughness of Rolls, Rolling speed, Flowability of powders
S	Compaction force, Formability of Powders, Rolling Gap
D	Roll Diameter
C	Rolling Speed

Evans and Smith [22] explained that, the actual nip angle is much lower than the calculated friction angle because of the slipping taking place between particles. A large diameter of roll is required to roll the same thickness of strip from solid material in practice. Usually the roll diameter is 50 to 150 times larger than the rolled strip thickness.

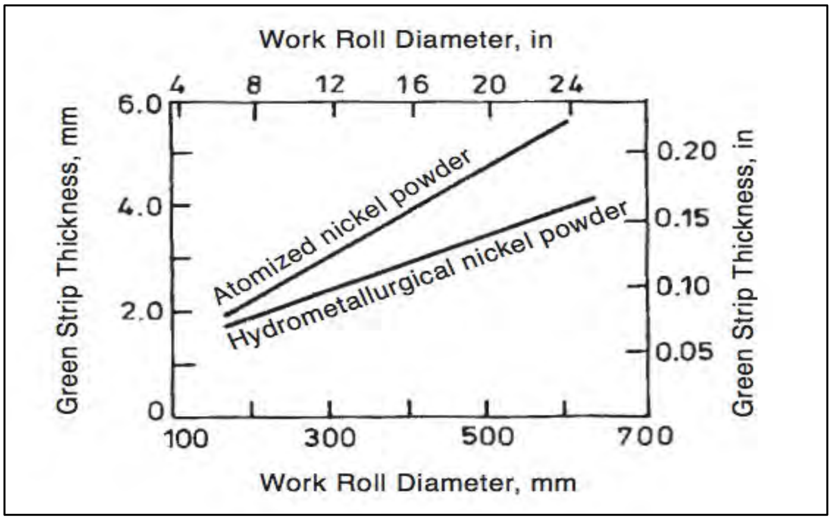

Figure 2.22: Relationship between green strip thickness and roll diameters with two types of nickel powders [5].

The graph in Figure 2.22 has shown the relationship between green strip thickness and roll diameters with two types of nickel powders. The slop difference is possibly caused by the particle shape and sizes.

Another aspect of rolling compaction is the width control. The strip edges must be well controlled in order to achieve uniform density along its width. In Figure 2.23(a) below, one flange type of roll overlaps another roll to prevent the powder moving sideways. Another technique of width control is to apply moving belts on the gap of two rolls, thus preventing powder loss from the gap as shown in Figure 2.23(b).

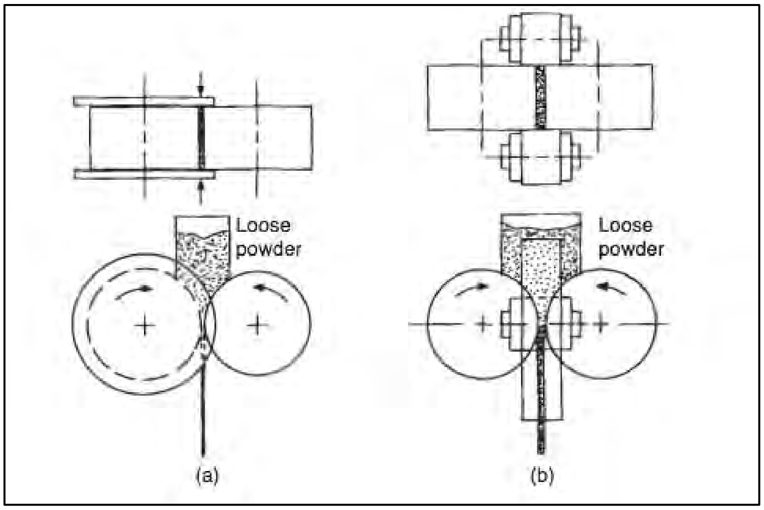

Figure 2.23: The edge control configuration of direct powder rolling [5].

Often the air may be entrapped in the powders and the stirring of the powder in the hopper can improve its flowability to the roll nip. Up to a given speed, called the 'flow transition speed', the flow rate of powder increases linearly with roll speed. Above this critical speed, relatively less and less powder flows into the roll gap, until at speeds considerably above the transition speed, continuous strip can no larger be rolled [5].

2.2.8 Sintering Process

Although the powder compacted product can reach up to 90% of its relative density, it still cannot be used directly for applications. This powder compacted product requires to be further densified in order to enhance its mechanical properties. This densification technique is called the sintering process. Sintering can be treated as a process that particles are bonding together under the influence of an elevated temperature. The temperature is usually below the metal melting point and sintering occurs by solid-state atomic motions. Densification and shrinkage is often associated with the sintering process. The surface energy per unit volume is inversely proportional to the particle diameter. Surface energy depends on the surface area and smaller particles with high surface areas to volume ratio have more energy. The driving force for solid-state sintering is the excess surface free energy. The loss of driving force with increasing time at any temperature is one of the reasons why it is so very difficult to remove all porosity by sintering [13].

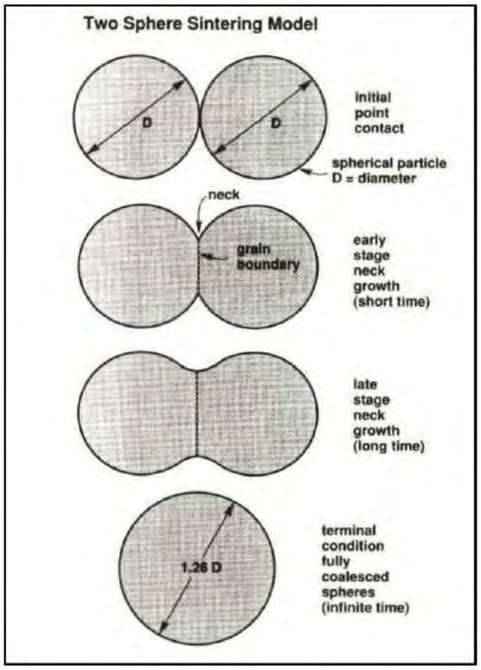

Figure 2.24 illustrates various stages of metal powder sintering can be classified in the following sequence: 1) initial bonding; 2) neck growth; 3) Pore closure; 4) Densification or shrinkage; 5) Pore coarsening [13].

In general, the highest possible density that can be achieved in sintered product is between 70 and 95% of the fully dense wrought product. However, the tensile properties and ductility are relatively lower than the wrought material of the same composition and structure due to the presence of porosity. These pores have detrimental effects on the mechanical properties of the material due to the stress concentration associated with them [13].

The sintering theory can be described in Figure 2.24 above. Assume spherical particles have many contacts in the powder compact and the bonds of contacting particles enlarge and merge under sintering. Each contact starts to grow and eventually a new grain boundary is formed. At a certain time, the two particles will merge into one single sphere. Theoretically, the new sphere has a diameter of 1.26 times than its original diameter [13].

2.3 Metal Powder Rolling Compaction Model Study

2.3.1 Introduction

A number of researchers have contributed to the development of the powder roll compaction process by different approaches. One of these approaches was the slab method which was developed by Katashinskii [17] to predict the pressure distribution and rolling force in metal powder rolling. Balicki et al. [18] reviewed that the advantage of this model is that it provides information about the two principal stresses and it has potential to include characteristics of powders such as cohesion and internal friction between particles. However, the ability to solve the resulting differential equation decreases considerably when more complex powder behavior characteristics are implemented.

The finite element method (FEM) is another most capable approach due to the substantial amount of information about rolling compaction geometry, powder rolling behavior, and frictional conditions that can be included in the simulation. This approach seems to be the most promising but it is not very practical. In fact, the ability of this approach to predict the operational parameters of rolling compaction mainly relies on the input information provided from the experimental data [18].

Johanson [21] developed a mathematical model which can predict the roll surface pressure, force and torque from the physical characteristics of the powder and the dimensions of the rolling mill. Bindhunmadhavan et al. [24] reviewed that the main advantage of this model is that it requires only a few experimental parameters for the powder: the angle of wall friction, the angle of internal friction (both measurable from shear testing experiments), and the compressibility factor (evaluated from the uniaxial compression). However, Johanson's model does not cover the effect of rolling speed or presumably the rolling speed is higher enough to produce the full roll face width of powder compact strip. Balicki et al. [18] also commented that this model can be used to calculate the maximum pressure exerted on the material being compacted and the final density of the powder compact can be predicted by combining the calculated pressure information with the experimental pressure-density relationship.

2.3.2 Johanson Rolling Model

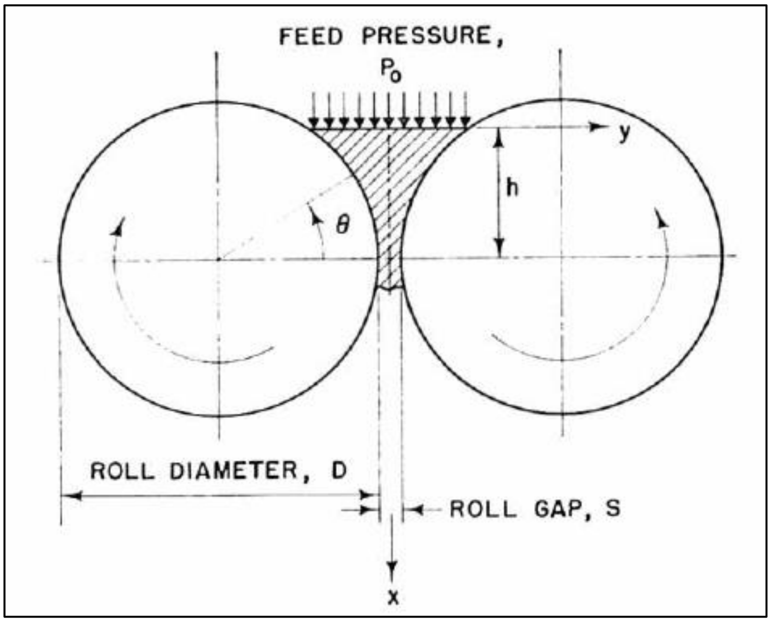

Figure 2.29: Metal Powder Roll Compaction [21].

The schematic of metal powder rolling compaction is sketched in Figure 2.29, which illustrates a continuous shear deformation process of powder material into compact strip. Johanson's theory describes the stress function in relation to roll geometry parameters and the plastic yield laws of the powder material undergoing continuous shear deformation between rolls proposed by Jenike and shield [23]. The theory is based on the behavior of powder material in the different compaction regions:

1. Initially, the loose powder is fed into the roll gap with a constant pressure screw or gravity-fed hopper. The bulk density of loose powder is not changed at this stage.
2. The powder begins to be compressed by the roll surfaces while the powder moves into the roll gap. The roll surface does not have enough normal pressure to grab the loose powder at this stage and thus the powder only experiences low shear stress in this region which is called the slipping zone.
3. The critical point along the roll surface where the powder stops slipping and starts to travel with the same speed as the roller is referred to by Johanson as the nip point; the angle of this point is denoted as $\theta = \alpha$.
4. The nip angle indicates the starting point of the compaction zone. In this region the powder experiences continuous shear deformation until the minimum roll gap is reached. This region is referred to as the nip zone.

2.3.3 Pressure Distribution at the Slip Region

The Johanson theory is based on the Jenike and Shield model for steady state powder particle flow during rolling compaction. The Jenike and Shield effective yield criterion (3-1) applies to a region between the rolls where the powder slips against the roll surface. The yield behavior of the powder is described by the internal friction angle δ.

$$\sin(\delta) = \frac{\sigma_1 - \sigma_2}{\sigma_1 + \sigma_2} \qquad (3\text{-}1)$$

This region starts where the powder is initially fed into the rolls, $\text{angle} = \theta_0$, at which point the feed pressure P_0 is the main stress experienced by the powder (3-1). The mean normal stress ($\sigma = (\sigma_1 + \sigma_2)/2$ for any θ) remains constant for considerable distance after the application of P_0, θ_h . Furthermore, the mean normal stress increases until the smallest roll gap S is reached where the $\theta = 0$.

$$\sigma_0 = \frac{\mathrm{P_o}}{(1 - \sin\delta)} \qquad (3\text{-}2)$$

The powder feeding angle θ_h is evaluated by using the wall friction angle ϕ and the effective internal friction angle δ (3-3).

$$\theta_h = \frac{\emptyset + \arcsin(\frac{\sin\emptyset}{\sin\delta})}{2} \tag{3-3}$$

One boundary condition is given by a condition of slip along the roll surface. The relationship between the tangential and the normal pressure or stress at the roll surface is given by the wall yield locus shown in Fig. 2.30.

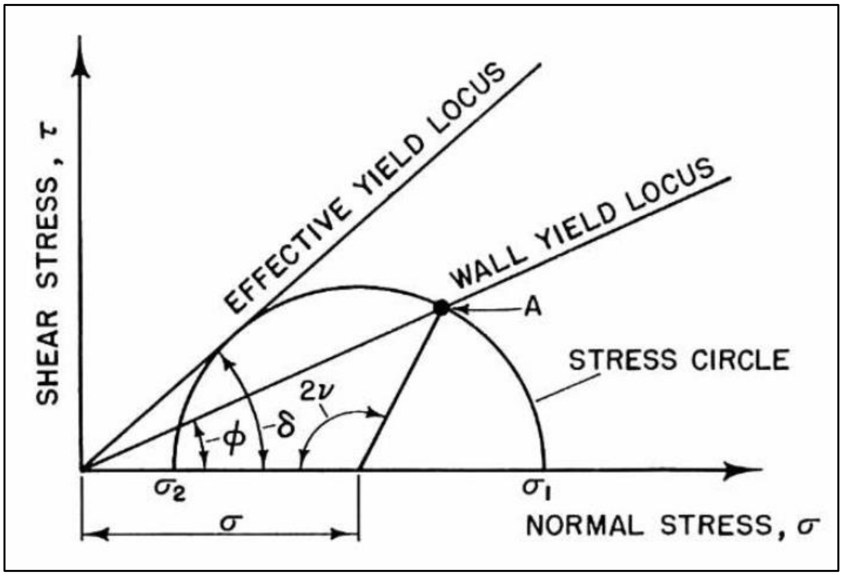

Figure 2.30: Jenike-Shield yield criterion for the internal and wall friction locus [21].

This friction between powder and roll surface is denoted as μ, but can also can be represented as a wall friction angle ϕ. Johanson explained that the frictional condition for slip along the roll surface, together with the position and magnitude of the feed pressure P_0, Fig. 2.29, is sufficient boundary information to determine the pressure distribution. The effective angle of internal friction δ and the wall friction angle ϕ is measured by using the shear cell test [23].

2.3.4 Pressure Distribution in the Nip Region

The powder particle flows to the nip zone and then is compressed until the smallest gap is reached. The mass conservation principle represented by equation (3-4) is applied due to the density change being proportional to the change in volume.

$$\frac{\gamma_\alpha}{\gamma_\theta} = \frac{V_\theta}{V_\alpha} \tag{3-4}$$

Assume a relative small segment of packed powder particles on the surface of arc-length ΔL has a volume of V_α and density of γ_α. According to the mass conservation principle, the same amount of mass of particles flow towards the smallest gap s or $\theta = 0$ and it must be compressed to a slice of volume of V_θ with a density of γ_θ that is under the same size of roll surface arc-length ΔL (see Figure 2.31). Therefore, the bulk density of particles is changed while the same amount of mass of particles move through the roll gap s.

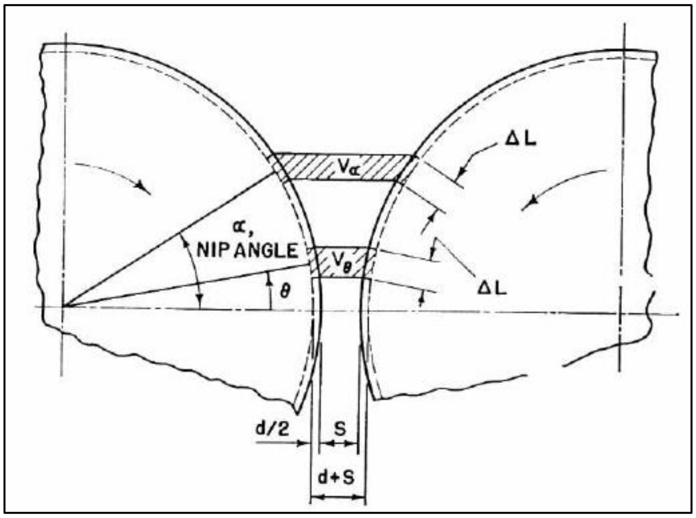

Figure 2.31: Region of nip in a roll press [21].

The Pressure-Density relationship is experimentally evaluated by a uniaxial pressing test. Experimental evidence indicates the fact that log density is a linear function of log pressure when the pressure is increased as shown in Figure 2.32.

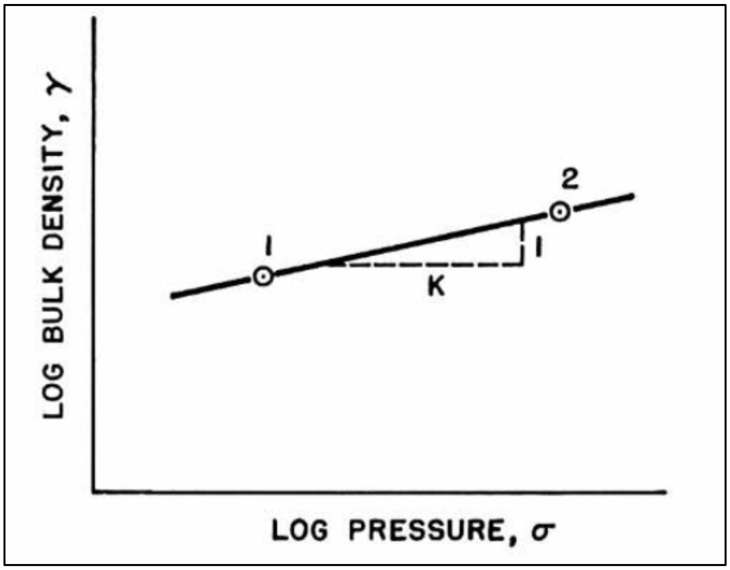

Figure 2.32: Pressure-density relationship [21].

This Pressure-Density linear function is given by the following equation:

$$\frac{\sigma_1}{\sigma_2} = \left(\frac{\gamma_1}{\gamma_2}\right)^K \tag{3-5}$$

Where K is a material property and is constant for a given moisture content, temperature, and time of compaction. This parameter describes the degree of volume reduction due to a certain pressure load. According to this linear relationship, the compressibility is obtained by plotting a certain number of pressure-density points from the uniaxial pressing test. The compressibility factor K is determined from the inverse gradient of the pressure-density function on a log plot. The value of K can be measured by a simple uniaxial pressing test.

The following relationship between stress or pressure at any angle θ, and stress at the nip angle, σ_α is derived from equations of (3-5) and (3-4):

$$\sigma_\theta = \sigma_\alpha \left(\frac{\gamma_\theta}{\gamma_\alpha}\right)^K = \sigma_\alpha \left(\frac{V_\alpha}{V_\theta}\right)^K \tag{3-6}$$

The volume V_θ between arc-length segment Δ*L,* roll diameter, *D* and roll width, *W* is given by:

$$\mathrm{V}_\theta = [\mathrm{d} + [\mathrm{S} + \mathrm{D}(1 - \cos\theta)\cos\theta]\Delta\mathrm{LW} \qquad \text{(3-7)}$$

The term d takes into account indentations in the roll surface, where it is defined as the average thickness of the rolled sheet when the roll gap S is zero. The value of d can be determined by the volume divided by the length multiplied by the width of the rolled sheet for S = 0. In fact, the value of d is negligible due to it is extremely small figure in relation to the roll gap. By combining Eq. 5 and 6 results in the following equation:

$$\sigma_\theta = \sigma_\alpha \left[\frac{\frac{\mathrm{d}}{\mathrm{D}} + \left(1 + \frac{\mathrm{S}}{\mathrm{D}} - \cos\alpha\right)\cos\alpha}{\frac{\mathrm{d}}{\mathrm{D}} + \left(1 + \frac{\mathrm{S}}{\mathrm{D}} - \cos\theta\right)\cos\theta}\right]^{\mathrm{K}} \qquad \text{(3-8)}$$

2.3.5 Determination of Nip Angle

Johanson speculates that there must be a transition point where the powder stops to slip along the roll surface and where the friction force is enough to stick the powder on the roll surface. . Johanson was able to separate the pressure distribution for the rolling compaction process under the slip or the no slip condition mathematically. In Figure 2.33, the solid curve represents the continuous slipping of the powder particles on the roll surface and the dashed curve represents no slipping or stick on the roll surface. The starting point of the nip region or the angular position, α or θ_i can be found by the intersection of the two curves in the given figure 2.33. Notably, the nip region is from the angular position of 0 to the angular position α or θ_i , and the powder slipping zone is between the angle θ_i and the point where the gradient of slip pressure curve equals 0 or θ_h and is also the starting point of feeding pressure P_o .

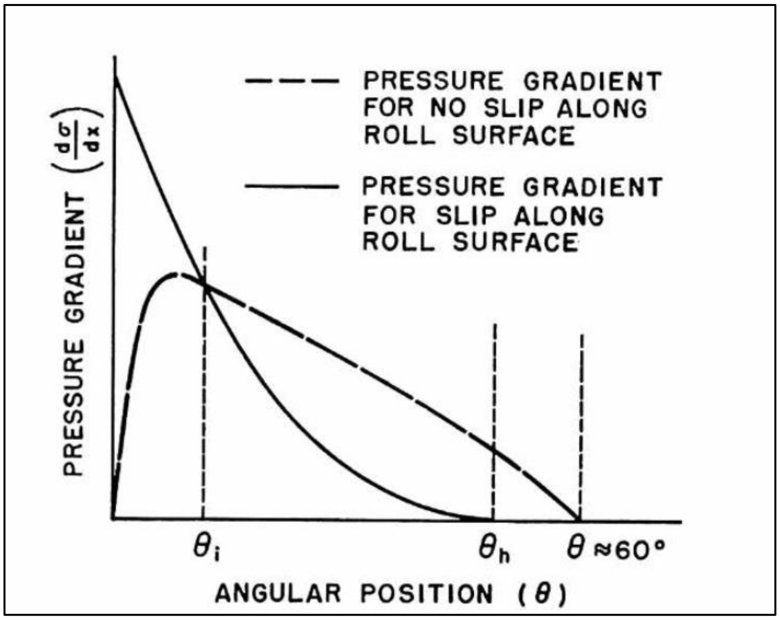

Figure 2.33: Vertical pressure gradient versus angular position in roll bite [21].

The pressure gradient for the assumption of powder slip condition (3-9) is derived by using the effective yield-locus criterion (3-1) combined with equilibrium conditions that form solvable hyperbolic equations of (3-9) and (3-10). However, the discussion of this method of calculation was beyond the scope of this dissertation.

$$\left(\frac{d\sigma}{dx}\right)_{\text{Slip}} = \frac{4\sigma\left(\frac{\pi}{2}-\theta-v\right)\tan\delta}{\frac{D}{2}\left[\left(1+\frac{S}{D}-\cos\theta\right)\right]\left[\cot(A-\mu)-\cot(A+\mu)\right]} \tag{3-9}$$

$$\left(\frac{d\sigma}{dx}\right)_{\text{No Slip}} = \frac{K\sigma_{\theta}\left(2\cos\theta-1-\frac{S}{D}\right)\tan\theta}{\frac{D}{2}\left(1+\frac{S}{D}-\cos\theta\right)\cos\theta} \tag{3-10}$$

The nip angle for a specific powder material is solved, by simply equating $\left(\frac{d\sigma}{dx}\right)_{\text{Slip}} = \left(\frac{d\sigma}{dx}\right)_{\text{No slip}}$, and solving for the angle $\theta = \alpha$. Hence, the nip angle α can be determined by solving equation (3-11) as follows.

$$\left(\frac{d\sigma}{dx}\right)_{\text{Slip}} = \left(\frac{d\sigma}{dx}\right)_{\text{No Slip}} \tag{3-11}$$

The variables appeared in the equations of (3-9) and (3-10) above are derived from the effective yield and wall locus (3-2) and are shown in the following equations:

$$A = \frac{\theta+v+\pi/2}{2} \tag{3-12}$$

$$\mu = \frac{\frac{\pi}{4}-\frac{\delta}{2}}{2} \tag{3-13}$$

$$v = \frac{\pi - \arcsin(\frac{sin\phi}{sin\delta})}{2} \tag{3-14}$$

In conclusion, according to the equations of (3-9) and (3-10), the nip angle mainly depends upon the compressibility factor K, the material flow properties, internal friction angle δ and wall friction angle ϕ, the roll diameter D and the roll gap S.

2.3.6 Roll Force and Torque Calculations

The pressure distribution was not very useful in the design of a rolling mill, and consequently Johanson provided the methods of calculating roll force and roll torque. When the pressure distribution in the nip region is known, the total roll-separating force can be calculated as

$$RF = \int_{\theta=0}^{\theta=\theta_h} \frac{P_\theta WDF}{2} \cos\theta d\theta \tag{3-15}$$

Where $P_\theta = \sigma_\theta(1+sin\delta)$ is the horizontal pressure at the center line between the rolls. The roll force can be approximated by reducing the upper limit of integration in equation (3-15) to $\theta = \alpha$. The result is :

$$RF = \frac{P_m WDF}{2} \tag{3-16}$$

where

$$F = \int_{\theta=0}^{\theta=\alpha} \left[\frac{\frac{d+S}{D}}{\frac{d}{D} + \left(1 + \frac{S}{D} - cos\theta\right) cos\theta} \right]^K \cos\theta d\theta \qquad (3\text{-}17)$$

And P_m is the maximum horizontal pressure exerted by the roll surface on the bulk material. Johanson describes that this pressure only occurs at $\theta = 0$. Similarly, the torque on each roll can be calculated by using the following equations

$$T = \int_{\theta=0}^{\theta=\alpha} \left[\frac{\frac{S}{D}}{\left(1 + \frac{S}{D} - cos\theta\right) cos\theta} \right]^K \sin\theta d\theta \qquad (3\text{-}18)$$

$$RQ = \frac{P_m W D^2 T}{8} \qquad (3\text{-}19)$$

2.3.7 Current Direct Powder Rolling Research

Roll Compaction of a Pharmaceutical Excipient: Experimental Validation of Rolling Theory for Granular Solids (2005) [24]

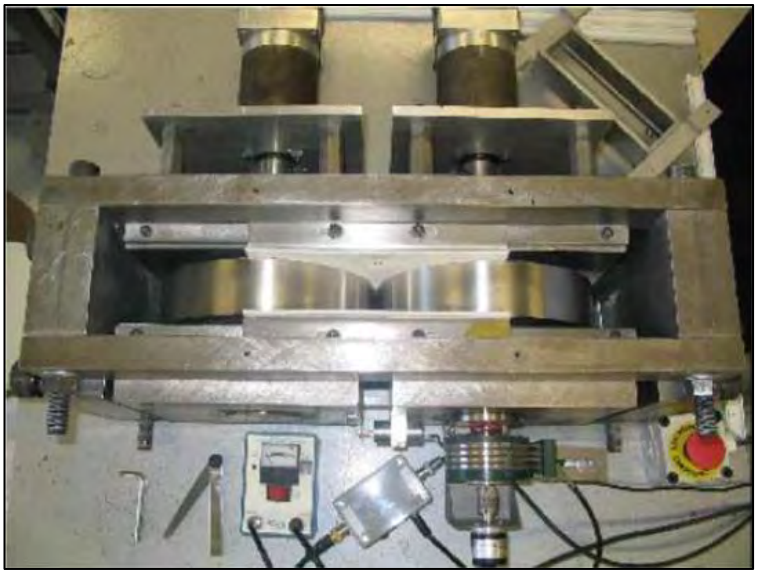

Figure 2.34: Laboratory scale instrumented roll press [24].

Much research has been conducted in creating high density and high performance PM metal products to challenge the conventional ingot products by using direct powder rolling process. Bindhumadhavan et al. [24] was one of the researchers who focused on conducting a detailed experimental powder rolling validation which was based on the Johanson's model.

In this work, one gravity-fed rolling compactor (see Figure 2.34) was built to measure compaction pressure by using a pressure sensor mounted in the roll shaft. The dimensions of roll compactor included 200 mm roll diameter, 46mm face width and adjustable 0-5mm gap sizes and 0.5-20 rpm controlled rolling speed. The microcrystalline cellulose grade Avicel PH102 of pharmaceutical excipient with a mean value (d50) of 105 µm was selected as the powder rolling material.

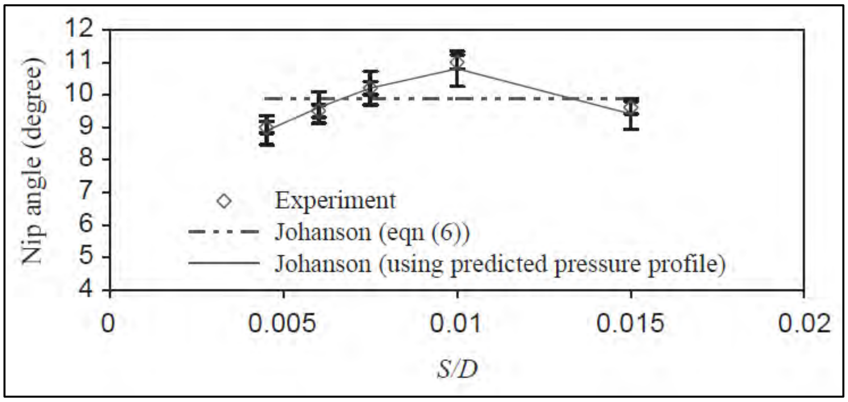

Figure 2.35: Comparison of the predicted and experimental nip angles [24].

The calculations were conducted for different roll gaps (s) with the same roll speed. The measured data and predicted results of nip angles for the same roll gaps and roll speed are shown in Figure 2.35. The result has shown the fact that the calculated nip angles were found to be almost independent of the gap due to the effect of the small value of the ratio S/D. The maximum difference between these two sets of measured values in relation to the calculated nip angle was only 1 degree of angular position. Bindhumadhavan et al. [24] explained that this difference depends upon the sensitivity of the pressure sensor.

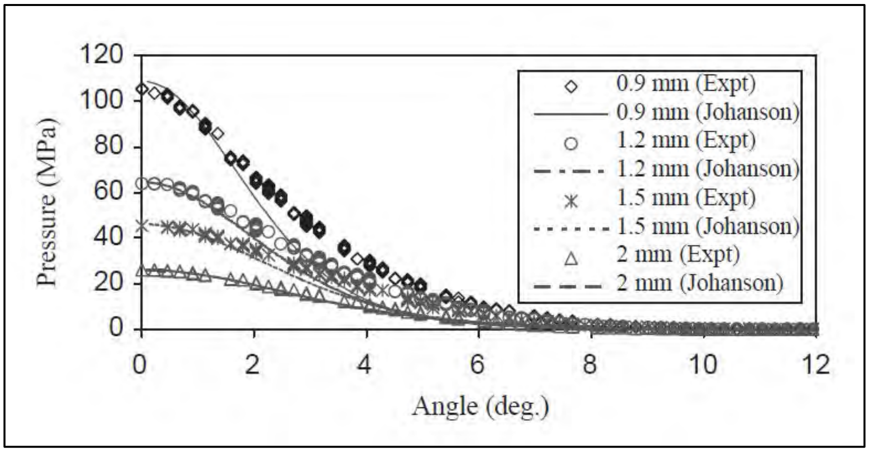

Figure 2.36: Effect of the roll gap on the measured rolling pressure profile versus the roller angular position [24].

In order to find the gap effect on the roll pressure, experiments were conducted at different roll gaps with a constant roll speed of 2 rpm. The measured data and calculated results of roll pressure are shown in Figure 2.36. The measured and predicted maximum pressures were matched up excellently but the measured data was increased more rapidly as the roll gap size deceases. Bindhumadhavan et al. [24] has found that one of the reasons is the deviations resulted from the roll gap approaching that of the particle size.

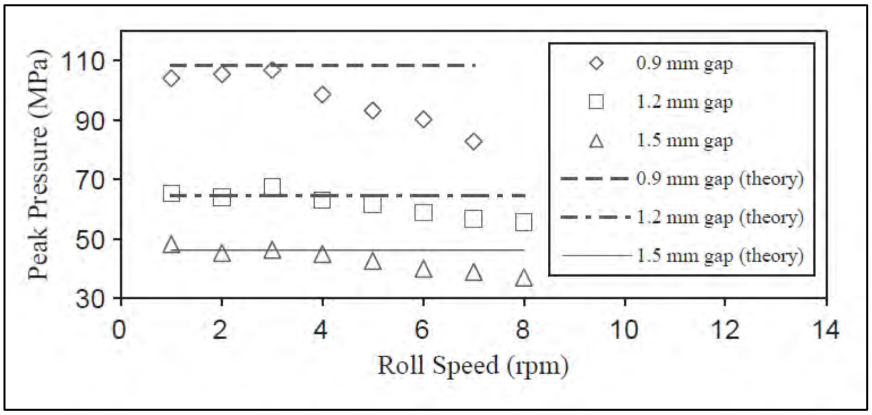

Figure 2.37: The effect of roll speed on the peak pressure at different roll gaps [24].

The experiments also were conducted at different roll speeds at three roll gaps since the Johanson's model does not take account of the roll speed effect. The results in Figure 2.37 proved that the measured peak pressures are nearly agreed with the theory at slow speeds.

However, peak or maximum roll pressure was decreased with increasing rolling speed. Bindhumadhavan et al. [24] explained that the rolling torque and roll force was decreased with increasing roll speed when the power is constant. G.Bindhumadhavan et al. [24] also claimed an assumption that might be able to account for the entrainment of air that results in a roll speed dependence of the roll pressure which is ignored in Johanson’s model.

In conclusion, this work has been proved that Johanson’s model is capable to provide a reasonable calculated result of nip angle and roll pressure from a rolling mill. However, Johanson’s model does not account for the reduction in the pressures at increasing speed.

Fabrication of Pure Iron Strips by Direct Powder Rolling Technique and Magnetic Properties (2006) [25]

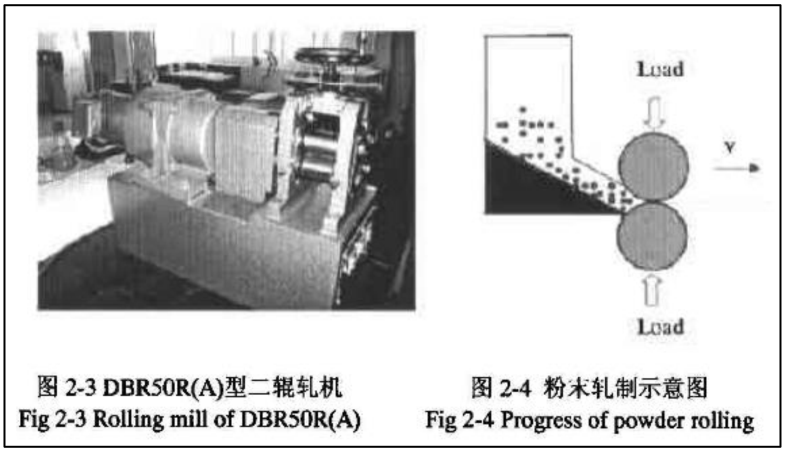

图 2-3 DBR50R(A)型二辊轧机
Fig 2-3 Rolling mill of DBR50R(A)

图 2-4 粉末轧制示意图
Fig 2-4 Progress of powder rolling

Figure 2.38: The image of roll compactor [25].

This masters’ dissertation was to study the effect of iron powder properties (flowability) and rolling parameters (roll gap) on the relative density and thickness of the compact green strips. In order to take account of the powder flowability or particle size effect, four different mesh sizes - 100, +200, +250, +325 of iron powders were selected for the experiment and they are denoted as powder 1, powder 2, powder 3 and powder 4 respectively. The photo of the rolling mill is given in Figure 2.38. Regarding the roll gap effect, it was varied in -0.05 mm, 0 mm, 0.05

mm, 0.10 mm, 0.15 mm and 0.20 mm. The rest of the rolling parameters were constant, including 50 mm rolling diameter, 70 mm rolling width and 2.3 m/min rolling speed.

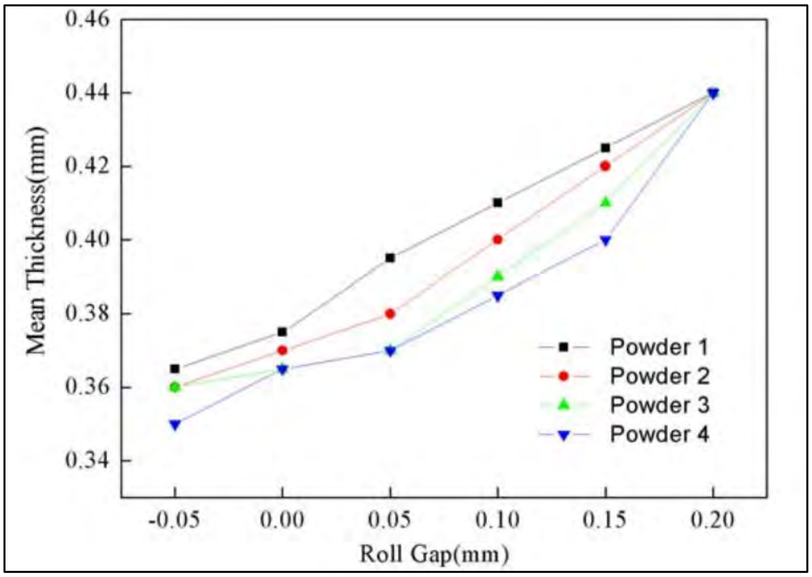

Figure 2.39: Effect of rolling gap on the thickness of strips [25].

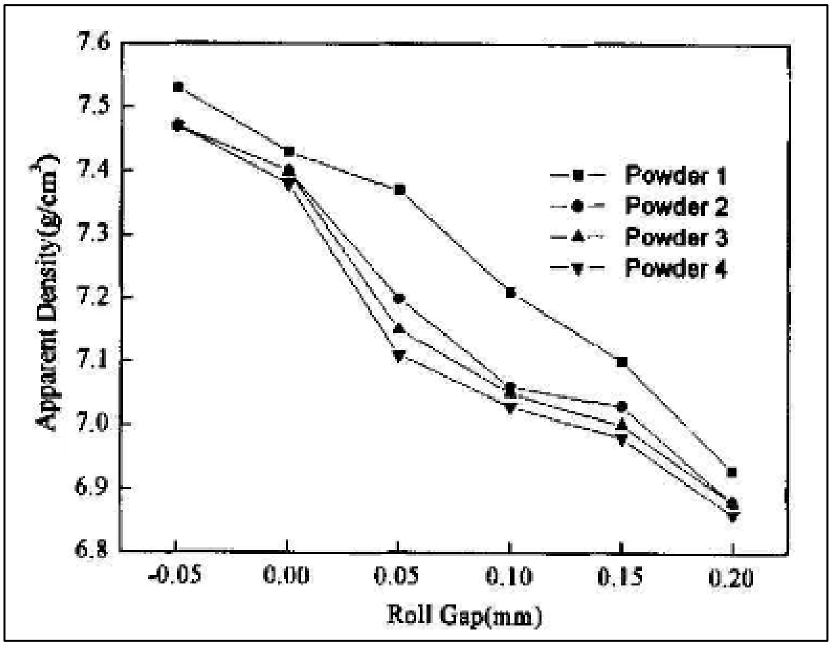

Figure 2.40: Effect of roll gap on the bulk density of strips [25].

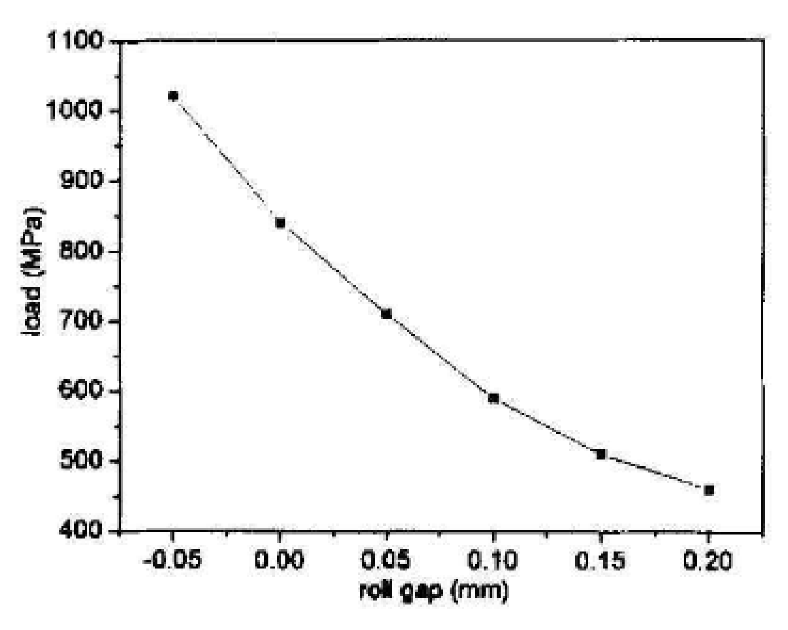

Figure 2.41: The relationship between roll gap and load (maximum rolling pressure) [25].

The results in Figure 2.39, 2.40 and 2.41 above have shown a similar trend among four different samples. The thicknesses of compact iron strips were always larger than the roll gap due to the spring-back effect on rolls and compact strips. The apparent density was decreased with increasing the roll gap among all four powder samples. The author explained that the compressive force was decreased when the roll gap is increased, so that the rolling force is one of the effects that directly influences the apparent density (bulk density) in direct metal powder rolling. Furthermore, the powder was not able to be compressed into strip when the gap was large enough. Relatively, the particle friction coefficient and bulk density (loose powder) of powder 1 is larger than the other powder samples, so that powder 1 has more material that was compressed per unit area and higher compact strip was produced.

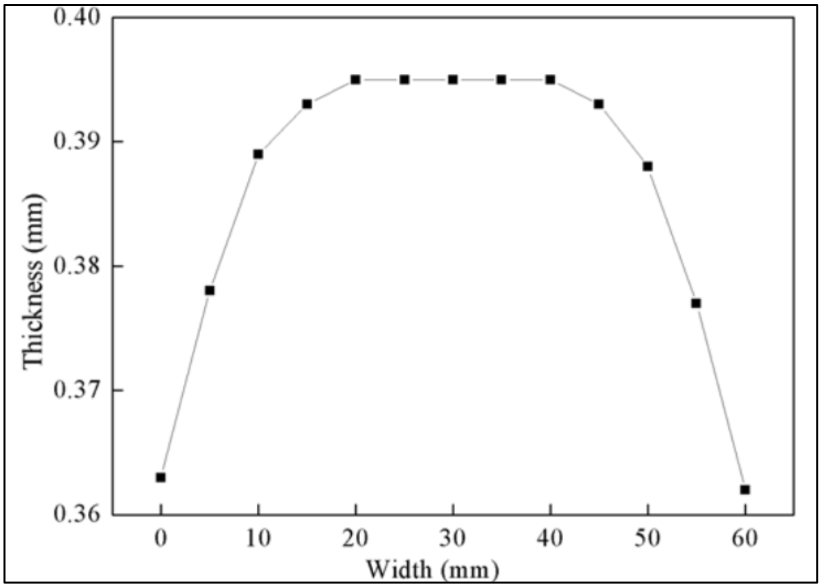

Figure 2.42: The variety of thickness with width of strips [25].

Regarding the range of thickness in Figure 2.42, the thickness of compact powder strip middle section was larger than the thinckness of strip edge. Li Yongjun [25] explained that this situation may be caused by the powder leakage from the gap between the side plates and roll surfaces. In addition, the powder also likely flow to the middle compression section rather than the sideways since the middle section has a relatively large gap caused by the deflection of the rolls.

Li Yongjun [25] concluded that the green density of rolled strip was influenced by the characteristics of powder and the rolling gap. In the same way, with larger apparent powder density (bulk density) and particle sizes, the relative density of rolled strip was increased. The densities of the rolled strip samples in four different particle sizes were decreased when the rolling gap increases. Moreover, the green strips were not formed when the rolling gap exceeds 0.2mm. The density in the middle section of the strip is higher than the edge and inhomogeneity always exists in the strips. The final density of the sintered iron strip was mainly relied on the density of the green strip due to the relative density of the green strip was increased only in small amount after being sintered for one hour at 900°C -1300°C. The highest density of sintered material was 7.58 $\mathrm{g/cm^3}$ and the highest density of the cold re-rolled sintered iron strip was 7.73 $\mathrm{g/cm^3}$ which is nearly 98.3% of its relative density. In addition, the density may be increased slightly if sintering time can be extended little longer and the cold re-rolling processing is better to be replaced by hot-rolling so that the edge crack caused by cold rolling can be avoided. This work has done an excellent parametric study in particle size and roll gap effect on the density and dimension of the green strip. However, the explanation of observed phenomenon is lack of appropriate theoretical support and some of the relevant parameters need to be further investigated such as rolling speed, rolling temperature and material feeding rate.

Process of Direct Powder Rolling of Blended Titanium Alloys (2006) [26]

The patent for Process of Direct Powder Rolling of Blended Titanium Alloys was published by ADMC Products in 2006 [26]. This invention was aimed at the direct rolling of elemental titanium alloy powders to a strip of 100% of the relative density. This rolling process consists of one vertical powder rolling mill and two horizontal cold re-rolling systems. The first vertical powder rolling was to achieve density of the rolled strip of 40%-80% of the relative density, whereby diameters of rolls are different, so that the green strip is bent for the subsequent re-rolling process to reach its 100% relative density.

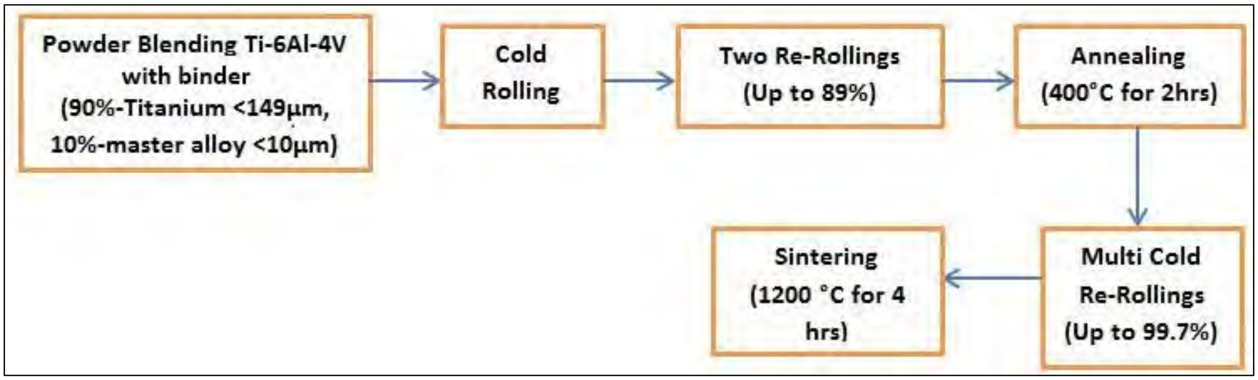

Figure 2.42: Flow diagram of process of direct powder rolling of blende titanium alloys.

Refer to Figure 2.42 above which demonstrates, the experiment illustrating the invention that produced rolled strip from elemental blended Ti-6Al-4V alloy powders with particle size less than 149 microns. The relative density of rolled green strip was 70% with 152.4 mm width and 6.35 mm thickness. The diameters of the two vertical rolls are 1270 mm and 1397 mm respectively, which resulted in bending deformation of the green strip. The rolled green strip was directed to the subsequent densification in the horizontal re-rolling mill staying in line with the first rolling mill. The green strip obtained from this re-rolling step had thickness of 3.81 mm and relative density of 89%. For stress relief, this strip was annealed for 2 hours in vacuum at 400 °C. Subsequently, this green strip was subjected to cold re-rolling process for final densification. The final relative density of 99.7% was obtained after multiple cold re-rolling in the rolling mill at continuously reduced gap between the roll until 2.54 mm was achieved. Then, the green strip was subjected to sintering process in vacuum condition for 4 hours at 1200 °C. Typical mechanical properties of fully-dense Ti-6Al-4V alloy strips produced by this invention were found: tensile strength is 897 to 966 MPa, yield strength is 828 to 897 MPa, and elongation is over 10%.

Several key elements of powder rolling were described by this ADMC patent. The diameter of the rolls of the direct powder rolling mill requires being 40-250 times larger than thickness of the rolled strip. The powder blend used is a mix of CP titanium matrix powder and an alloying powder having a particle size at least ten times smaller than the matrix powder in order to reduce the voids between CP-titanium and alloying particles. This ADMC has claimed that the green density of strips cannot reach to 100% due to a presence of residues of organic binders that do not allow to achieve an effective densification by compaction during cold rolling of green strip. Moreover, evaporation of binders creates the voids which cannot be removed during sintering and which form so-called gaseous porosity. The final examined mechanical properties of the sintered strips were almost equalized with the ASM (grade 5) Ti-6Al-4V strips. However, Commonwealth Scientific and Industrial Research Organization (CSIRO) has reviewed that the metal production cost component for titanium strip is very high relative to the production of strip of other metals [27]. Thus, it is necessary to seek cost reducing efficiencies at all production stages until a more cost efficient process is developed.

Titanium Flat Product Production (2010) [27]

The patent for Titanium Flat Product Production [27] was published by CSIRO in 2010. A continuous titanium powder rolling process was developed by the CSIRO titanium powder metallurgy group. This rolling process consists of a vertical rolling mill, pre-heating station, hot rolling station and a cooling station.

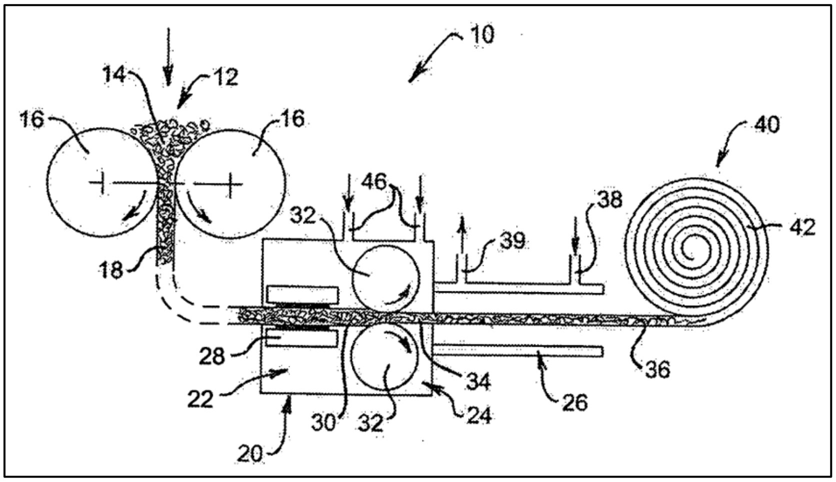

Figure 2.43: the configuration of continuous titanium powder rolling process [26].

The CSIRO titanium powder rolling process is illustrated in Figure 2.43. The titanium powder is inserted in the hopper for the vertical cold rolling process after the powder has been pre-heated to a temperature of 40°C to 80°C to enhance its flowability. Secondly, the cold rolled titanium strip is passed through a pre-heating station and was heated at temperature of 750°C to 1350°C for 2-5 minutes under a protective atmosphere. Thirdly, the heated green strip is subjected to a second rolling device when its temperature is dropped to 800°C to 1000°C during transportation. Finally, the hot rolled strip is passed through a rapid water cooling station under a protective atmosphere until its temperature is dropped below 400°C (see flow chart in Figure 2.44).

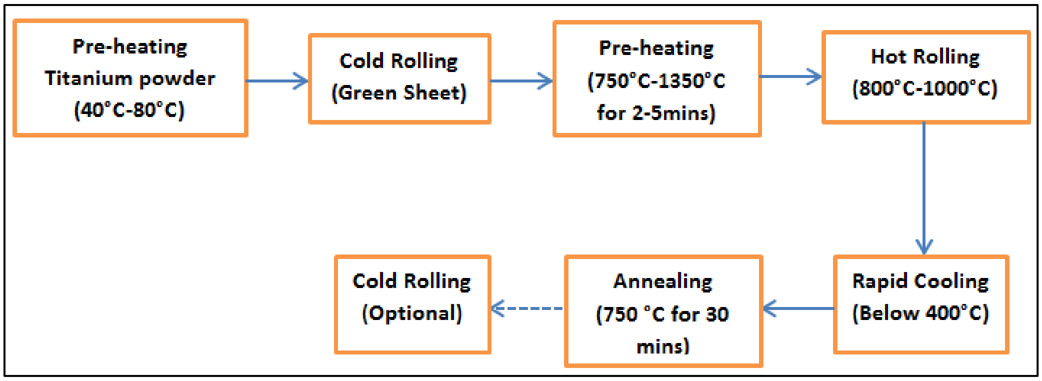

Figure 2.44: Flow diagram of process of titanium flat product production.

The first powder rolling trial experiment used a hydride-dehydride derived grade 3 titanium powder with an oxygen content of 0.32 to 0.35% and particle size less than 150 microns. The relative density of rolled green strip was measured as 81% with 1.2 mm thickness and 100 mm width. The green strip was hot rolled twice at a speed of 4 m/min through the hot rolling chamber at a temperature of 1200°C. The first hot rolling was at a reduction of 35% and the second hot rolling at 15% which resulting in a total thickness reduction of 50%. The final relative density was greater than 99.9% after the hot rolling process. This hot rolled strip was then subjected to an annealing process at 750°C for 30 minutes in order to achieve stress relief. The following mechanical testing resulted in elongations of 16 to 18% with a tensile strength of 750MPa and a 0.2% proof yield strength of 670 MPa.

In the second trial, the hydride-dehydride titanium powder was replaced by sodium reduced titanium powder (oxygen at 0.10 to 0.13%, Cl at about 1000 ppm) with particle size less than 150 microns. This powder was cold rolled to relative density of 89% with 1.00 mm thickness and 100 mm width. The green strip was hot rolled twice at a speed of 6 m/min through the hot rolling chamber at a temperature of 1200°C. The first hot rolling was at a reduction of 43% and the second hot rolling at 16% which resulting in a total thickness reduction of 59%. The final relative density was greater than 99.5% after the hot rolling process. This hot rolled strip was subjected to annealing process at 750°C for 30 minutes in order to achieve stress relief purpose. The following mechanical testing resulted in elongations of 16 to 18% with a tensile strength of 525 MPa.

This invention of powder rolling process is more compact relative to the ADMC rolling process. A number of repeating rolling steps was reduced by the CSIRO invention such as multi re-rolling and sintering. The most critical improvement was that a protective atmosphere is present all along the hot rolling and rapid cooling processes to avoid oxidation. This patent was mainly to provide a continuous titanium powder and titanium alloy rolling process. The patent is still limited to understanding of the relationship between the rolling process and the quality of final strip. However, this work has provided valuable information for the additional heat treatment that after the direct cold powder rolling process.

Chapter 3

Experimental Methodology

3.1 General Experimental Methodology

The goal of this experimental procedure is to investigate the influence of the direct rolling parameters including rolling speed, powder feeding rate, roll gap and roll width on the physical properties and dimensions of the powder compact strip. This work was based on the Johanson's theory to simulate the direct powder rolling process. Parametric studies were conducted in various setups of powder rolling combination accordingly. For cost concerns, stainless steel 316L powder was selected as alternative powder material that can avoid oxidation during handling in laboratory processes for the initial investigations in this study. Eventually, CP-titanium powder rolling was optimized to reach its highest possible relative density according to the simulated results and parametric studies on stainless steel 316L.

3.1.1 Material

The stainless steel AISI 316L and hydride-dehydride (HDH) CP-titanium powders was supplied by Chengdu HuaRui Industrial and the details of these powders are listed below:

- **Pre-alloyed Stainless Steel 316 Powder:**

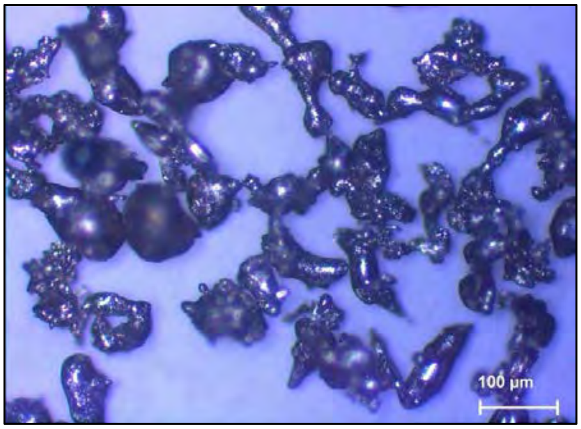

CHEMICAL CONTENT wt (%)		**PARTICLE SIZE**: -100+200 mesh	
Cr	17	Ni	11.01
Mo	1.98	C	0.021
Si	1.67	O	0.24
Fe	Bal		
PHYSICAL PROPERTIES			
Hall Flow Velocity(s/50g)		25	
Bulk Density (g/cm^3)		3.3	

- **HDH CP-titanium Powder:**

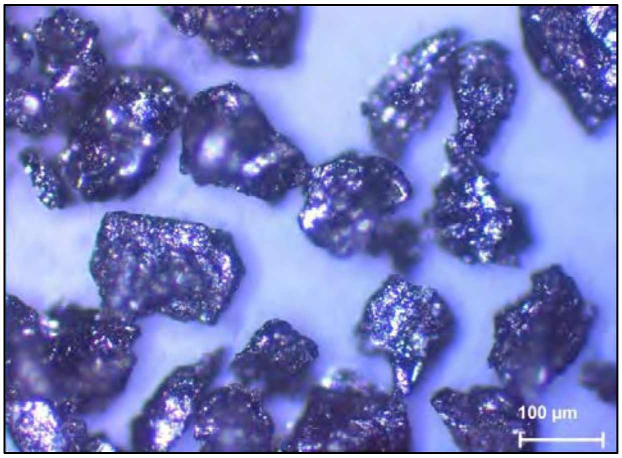

CHEMICAL CONTENT wt (%)		**PARTICLE SIZE**: -100+200 mesh	
Ti	99.4	Si	0.02
N	0.025	Fe	0.035
C	0.02	O	0.3
H	0.03	Cl	0.04
Al	0.006		
PHYSICAL PROPERTIES			
Hall Flow Velocity(s/50g)		35	
Bulk Density (g/cm^3)		1.8	

3.1.2 Direct Powder Rolling Apparatus

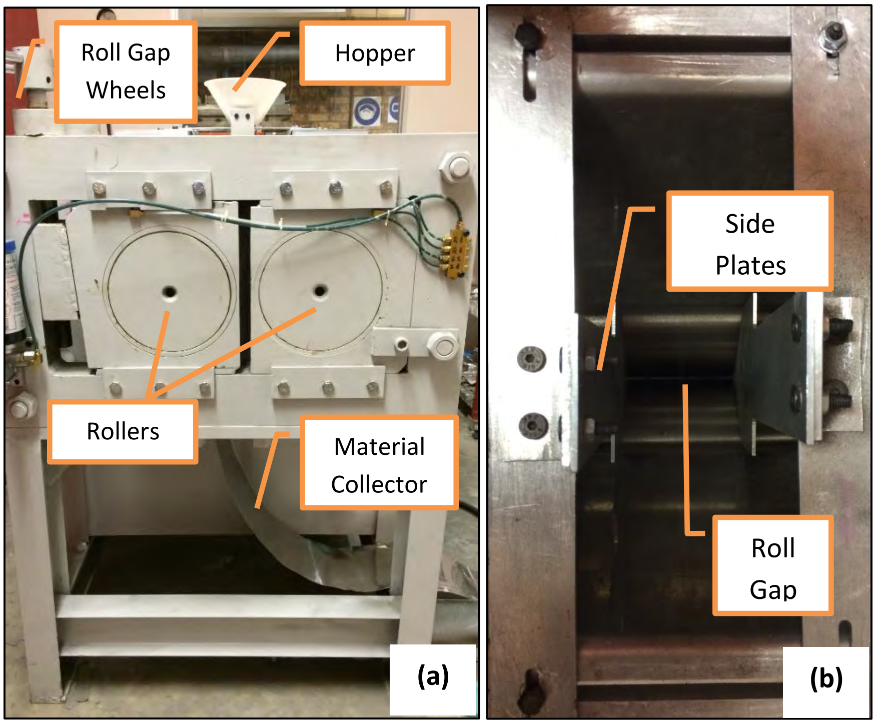

Figure 3.1: Gravity-fed vertical powder rolling mill.

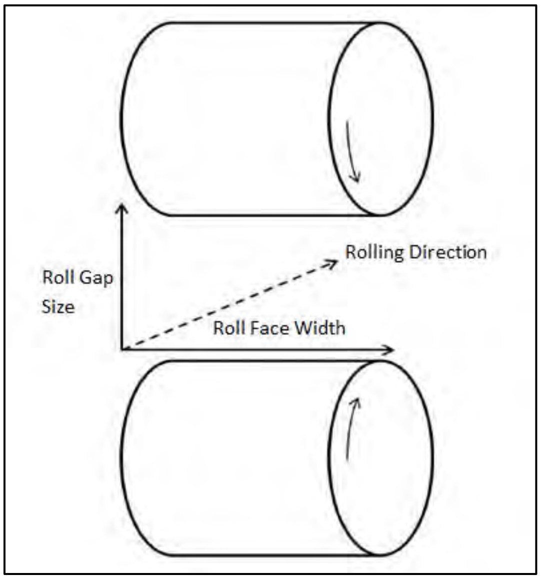

Figure 3.2: Schematic of the Roll gap, Roll face width and rolling direction in roll compaction [28].

The direct powder rolling experiments were carried out on the CME laboratory rolling mill shown in Figure 3.1(a) which was equipped with two horizontal arranged rollers that have diameters of 265 mm and mean surface roughness of 2.5 µm. The roll gap (S) can be adjusted between 0.5 to 5 mm and the roll face width (W) can be varied from 0 to 150 mm by a set of aluminum side plates mounted on the feed zone shown in Figure 3.1(b) and 3.2. The rolling speed range of this rolling mill is capable to be varied from 0 to 14 rpm. The powder feeding rate was controlled by three gravity-fed hoppers which have different outlet diameters of 1.5 cm, 2 cm and 2.5cm. The powder material volume was fixed at 200 ml in order to produce 200 – 400 mm long strip depending on roll gap and roll face width for each trial.

Direct Powder Rolling Procedure:

1. Measure 200 ml stainless steel 316L or CP-titanium powder into glass containers.
2. Set the relevant rolling parameters according to the planned rolling setup combinations.
3. Start the rolling mill until the rolling speed reaches the desired value.
4. Fill the measured 200 ml powder into hopper and let it gravity-fed to the roll gap.
5. Collect the powder compacted strip from the material collector.

3.1.3 Density Measurement

The procedure used for measuring the density of powder metallurgy and as-sintered products that usually have surface-connected porosity which is given in detail in ASTM B962-13[29] standard and is included in the appendix of this work.

Figure 3.3: Beaker support above balance pan [29].

The equipment required is shown in Figure 3.3. The rig consists of a mass balance, a “bridge”, a beaker and a specimen support structure. The bridge is used to support the beaker above the balance pan and the specimen support is connected to the balance pan. A wire basket, connected to the specimen support, hangs into the water and contains the specimen. The technique involves taking five measurements: the mass of the test specimen in air (A); the mass of the oil-impregnated test specimen (B); the mass of the oil-impregnated test specimen and specimen support immersed in water (C); the mass of the oil-impregnated test specimen support immersed in water (E).

The relative density is determined by the formula as follows:

$$D_g = \frac{A\,\rho_w}{B-(C-E\,)}$$

Where

Dg = green density of test specimen, $\mathrm{g/cm^3}$
A = the mass of the green specimen in air, g
B = the mass of the oil-impregnated test specimen, g
C = the mass of the oil-impregnated test specimen and specimen support immersed in water, g
E = the mass of the oil-impregnated test specimen support immersed in water, g

and

ρ_w = the density of water, g/cm

3.1.4 Microstructural Analysis

Grinding and Polishing

Specimens were ground and polished by the technique for titanium as detailed in Table 3.1 below. This material graphic preparation was followed by the Struers instrument.

Table 3.1: Steps of the grinding and polishing for CP-Titanium Specimen.

Step	Grit/Pad	Speed (rpm)	Force(kN)	Time(min)	Lubricant
1	1200 SiC	200	30	1:00	Water
2	4000 SiC	200	30	1:00	Water
3	MD Dac	150	30	5:00	3µm Diamond Suspension
4	MD Nap	300	30	5:00	OP-Nap Colloidal Silica

Etching Procedure

In order to analyze the microstructure, polished samples were etched for approximately 15 seconds by using Kroll's reagent (Table 3.2). Samples were then rinsed with distilled water to prevent the reaction and followed by an ultrasonic bath in one minute for cleaning. Finally, the samples were dried for 45 minutes in 50 °C before microscope examination.

Table 3.2: The formulation of Kroll's reagent.

Component	Volume (ml)
50% Nitric Acid (HNO3)	2
40% Hydrofluoric Acid (HF)	1
Distilled Water	100

Light Microscopy

Light Microscopy was carried out using a Reichert MeF3A inverted light microscope that was fitted with using a bright-field mode Leica DCF 320 camera and images were acquired.

3.2 Methodology of Direct Powder Rolling Modelling

The powder rolling model was simulated by using a Matlab platform to determine the nip angle for the powder material at specific rolling parameter combinations. Subsequently, the pressure distribution curve was plotted from the nip region once the nip angle is determined. The maximum rolling pressure where the pressure at the angular positon $\theta = 0$ was plotted for different roll gaps. The obtained maximum rolling pressure determined for specific roll gaps was further converted to the relative densities for both stainless steel 316L and CP-titanium according to their pressure-density relationships.

3.2.1 Cold Uniaxial Pressing

Overview

The uniaxial pressing test was employed to find the linear pressure-density relationship or compressibility of the powder material. The CP-titanium and stainless steel powders were pressed uniaxially on an Enerpac 100 ton press with both punches moving for measuring its compressibility. Subsequently, the compressibility factor (K) was calculated from the pressure-density curve. The process is summarized in the Figure 3.4 below. It involves filling the die with powder, setting the required pressure from the machine, pressing and ejecting the compact from the die.

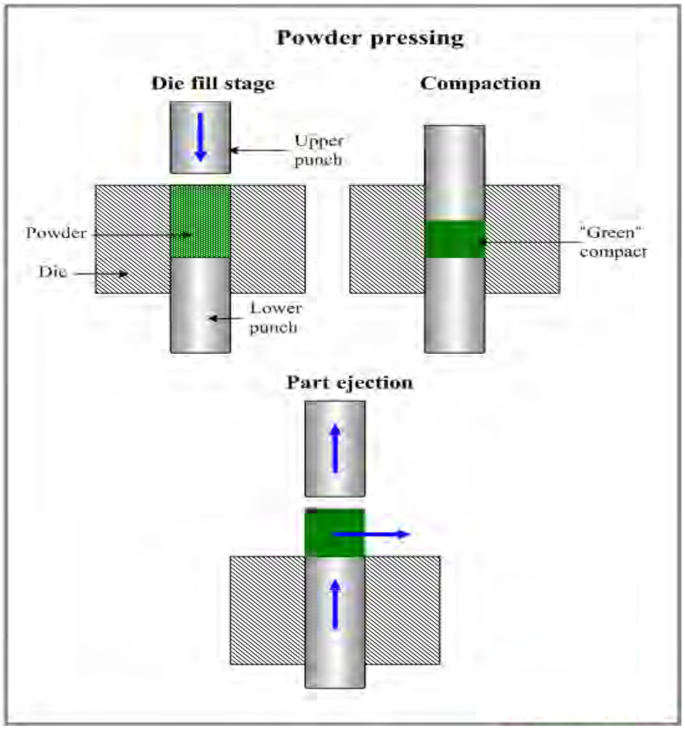

Figure 3.4: Schematic of cold uniaxial pressing process.

A 17.5mm die was used with a thin film of zinc stearate (ZnSt) die wall lubricant applied to the walls of the die. The press was set to a value on the pressure gauge which is in bar. Five pressures of 100, 200, 300, 400 and 500 bars were used and were converted to MPa in order to calculate the pressure on the sample. The pressure on the sample was calculated based on the size of the plungers and the die and are given in Table 3.3 below.

Pressing Procedure:

1. Measure 5 g samples into glass containers.
2. Fill the die by pouring powder into die.
3. Insert the die on the machine with the bottom plunger fixed.
4. Press the powder using the top plunger at the pressure selected on the machine.
5. Eject the sample by raising the lower punch.

Density Determination Procedure:

1. Measure the mass of the compact on a balance.
2. Measure the thickness (height) of the sample using the micrometer screw gauge.
3. Measure the diameter of the sample using a Vernier caliper.
4. Calculate the density by using the (m/v) formula.

The results obtained from this procedure can clearly be represented on a compressibility of % relative green density versus compaction pressure.

Table 3.3: Pressure conversion of cold uniaxial test

Applied pressure in Bar	Applied pressure in MPa	Pressure on Sample (MPa)
100	10	327
200	20	653
300	30	979
400	40	1306
500	50	1632

3.2.2 Powder Shear Test

Overview

Shear properties are important for understanding how easy the consolidated powder is able to flow. For this flow to occur, the yield limit of the powder must be overcome. In general, physical properties such as size, shape, and surface roughness of the particles can significantly influence the yield point. The powder shear test is capable to plot the Jenike-Shield yield locus plot for stainless steel and CP-titanium to determine certain variables in the powder rolling model such as powder internal friction angle (ϕ).

General Methodology

The rotational shear cell module in Figure 3.5 consists of a vessel containing the powder sample and a shear head to provide both vertical and rotational stresses. The dimensions of this shear cell module are given in Table 3.4. The shear head moves downwards inserting the blades into the powder and produces a normal stress as the shear head face contacts the top of the powder. The shear head continues to move downwards until the required normal stress, σ, is established. Slow rotation of the shear head then begins, producing a shear stress τ. A shear plane is established just below the ends of the blades.

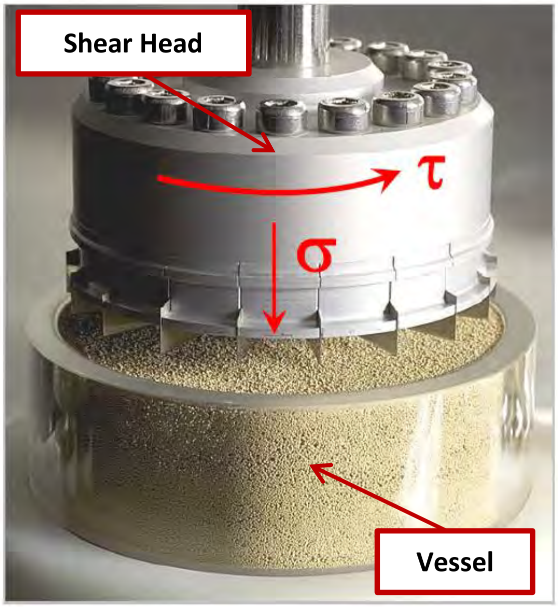

Figure 3.5 Schematic of powder shear test setup.

Table 3.4: The detail of the shear test fixture.

Vessel Size	Standard Program Name	Starting Accessory	Vessel
25 mm	25mm__σ_{ps} _15kPa	23.5mm Blade	25mmx 10ml Split Vessel

As the powder bed resists the rotation of the shear head, the shear stress increases until the bed fails or shears, at which point a maximum shear stress is observed. The normal stress is maintained constant throughout the shear step and the maximum shear stress is the point of incipient failure of the yield point.

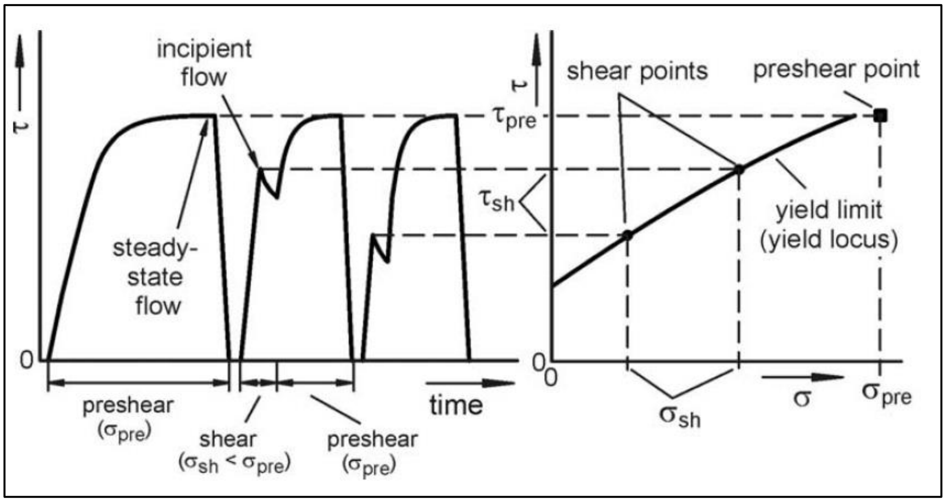

Figure 3.6： The shear test profile of normal stress and shear stress[31].

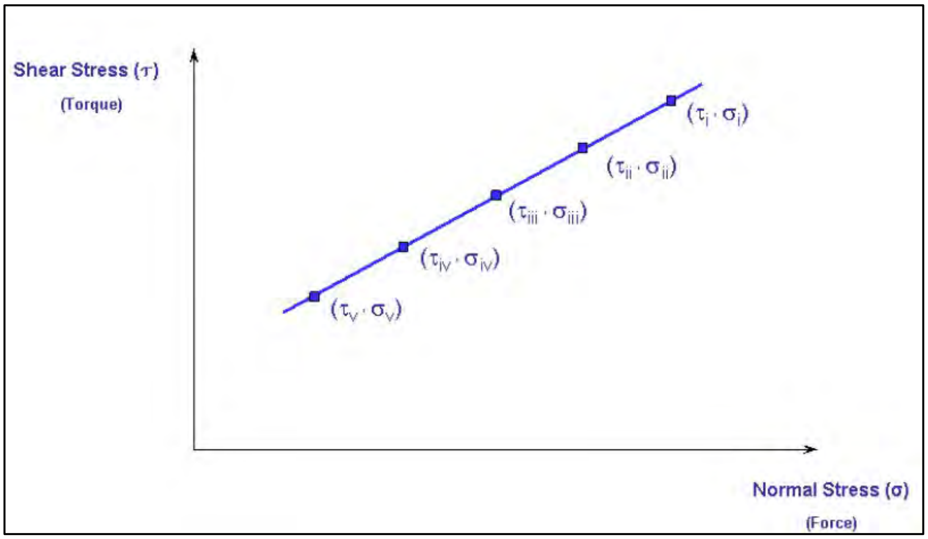

Figure 3.7: Powder yield locus.

Table 3.5： Applied normal stresses for shear test of titanium and steel powder.

Normal stress (KPa)	$\boldsymbol{\sigma_i}$	$\boldsymbol{\sigma_{ii}}$	$\boldsymbol{\sigma_{iii}}$	$\boldsymbol{\sigma_{iv}}$	$\boldsymbol{\sigma_v}$
Titanium and Stainless steel Powder	9	8	7	6	5

Shear Test Procedure (see Figure 3.7 and Table 3.5):

1. Apply 15 kPa pre-consolidating normal stress σ_{pre} and pre-shear until steady state is achieved.
2. Apply σ_i kPa normal stress and shear it until incipient flow occurs.
3. Apply 15 kPa pre-consolidating normal stress σ_{pre} again and pre-shear until steady state is achieved.
4. Apply σ_n kPa normal stress and shear it until incipient flow occurs.
5. The applied normal stresses have a magnitude relationship of $\sigma_{\text{pre}} > \sigma_i > \sigma_{ii} \ldots > \sigma_n$.
6. This test was performed for five normal stresses which are shown in Table 3.5 and each test was repeated three times on both titanium and stainless steel powder.

The principles of measuring shear properties and constructing the Jenike-Shield yield loci are explained in Figure 3.6, each obtained value of the incipient shear τ from the applied corresponding normal stress σ is projected to the stress-shear coordinate system, and as known shear point. The best fit line for connecting these shear points from y-axis is the yield locus or the yield limit of the bulk material. In particular, in order to obtain reproducible results and well defined incipient failure point, it is necessary for the sample to be over-consolidated with respect to the normal stresses imposed during the shear test. Therefore, the pre-consolidating normal stress σ_{pre} is applied to over consolidate the sample at a maximum normal stress until the shear stress reaches steady state.

Determination of Effective Internal Friction Angle φ

The yield locus is used to further analyse test data with the application of Mohr Stress circles which are constructed as follows (see Figure 3.8):

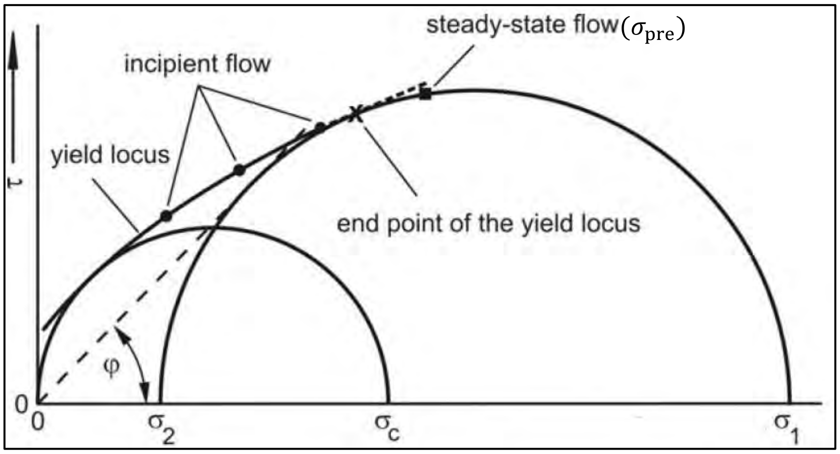

Figure 3.8: Diagram of effective internal friction angle determination[31].

Procedure (see Figure 3.8):

1. A semi-circle or unconfined stress circle is drawn which passes through the origin and is tangential to yield loci (e g. the best fit linear line of five test data points).
2. A second semi-circle is drawn which passes through the steady-state flow point - σ_{pre} and is tangential to the yield loci.
3. A straight line is drawn which passes through the origin and is tangential to the greater Mohr stress circle.
4. The effective internal ϕ friction angle is measured from the slope of this straight line.

3.2.3 Wall Friction Test

Overview

Wall Friction properties are important for understanding how easy the metal powder begins to flow in relation to the roller surface. The wall friction test setup (see Figure 3.9) is similar to the shear test and the difference is that the wall friction disk is used instead of the shear head blade in the shear test. The dimensions of wall friction test fixture are given in Table 3.6. The wall friction disk has the same surface roughness as the roller surface. The test is to determine the wall friction angle (δ) for the powder rolling model implementation.

Figure 3.9: Wall friction disk.

Table 3.6: The detail of the shear test fixture

Vessel Size	Wall Friction Disc	Standard Program Name	Starting Accessory	Vessel
25 mm	24mm_2.5um roughness	25mm__σ_{ps} _15kPa	23.5mm Blade	25mmx 10ml Split Vessel

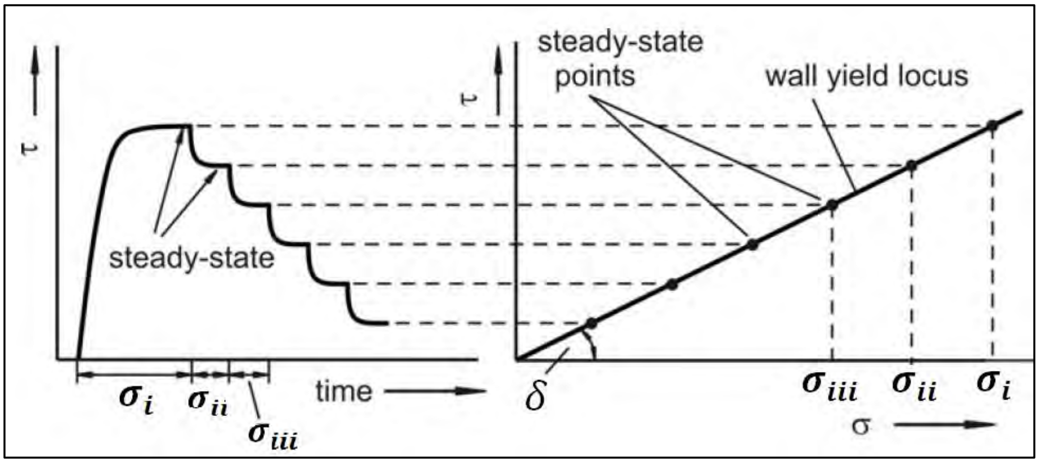

Figure 3.10: The wall friction test profile of normal stress and shear stress[31].

Table 3.7: Applied normal stresses for wall friction test for titanium and steel powder

Normal stress (kPa)	$\boldsymbol{\sigma_i}$	$\boldsymbol{\sigma_{ii}}$	$\boldsymbol{\sigma_{iii}}$	$\boldsymbol{\sigma_{iv}}$	$\boldsymbol{\sigma_v}$
Titanium and Stainless steel Powder	9	8	7	6	5

Wall Friction Test Procedure (see Figure 3.10 and Table 3.7)***:***

1. Apply 15 kPa Pre-consolidating normal stress σ_{pre} and pre-shear until steady state is achieved.
2. Apply σ_i kPa normal stress and shear it until another steady state is achieved
3. Apply σ_n kPa normal stress and shear it until steady state is achieved.
4. The applied normal stresses (see Table 3.7) have a magnitude relationship of $\sigma_{\text{pre}} > \sigma_i > \sigma_{ii} \ldots > \sigma_n$.
5. This test was performed for five normal stresses and each test was repeated three times on both CP-titanium and stainless steel 316L powder.
6. Plot each of the steady-state shear stress value against its corresponding normal stress in the stress and shear stress graph.
7. Construct the Wall friction locus and determine the Wall friction angle δ.

3.2.4 Implementation of Direct Powder Rolling Model

Matlab mathematics software and the program that is developed by Balicki et al. [18] were used to implement the Johanson's model for direct powder rolling to analyze the roll compaction pressure distribution during the rolling process. The required input parameters and output data for the simulation are indicated in Table 3.8. A flow chart for the entire simulation execution is indicated in Figure 3.11.

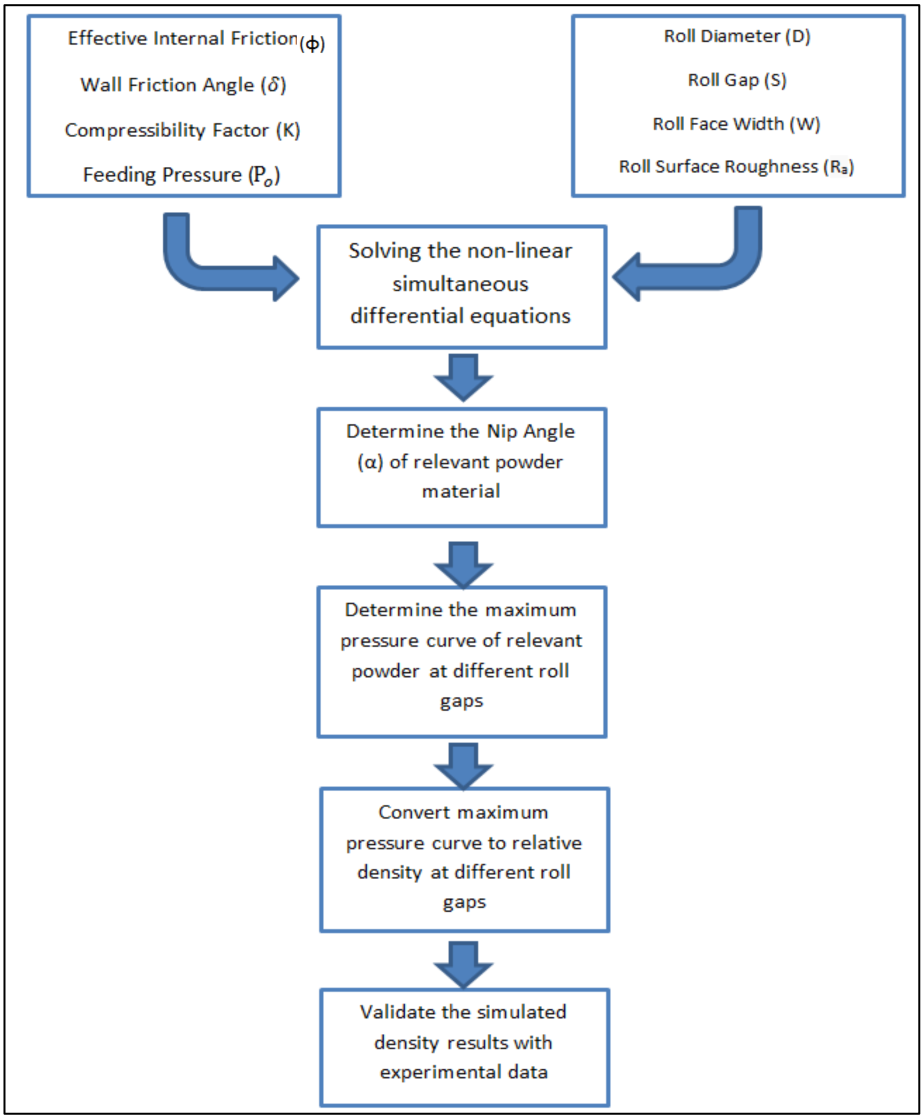

Figure 3.11: Flow chart of direct powder rolling simulation.

Table 3.8: Summary of input parameters and output data for Johanson powder rolling model.

Powder Rolling Model	Input Parameters	Output Data
Characteristics of Powder Material	Effective Internal Friction Angle (ϕ)	Maximum Rolling Pressure Rolling Force Rolling torque
	Wall Friction Angle (δ)	
	Compressibility Factor (K)	
	Feeding Pressure (P_o)	
Geometry of Rolling Mill	Roll Diameter (D)	
	Roll Gap (S)	
	Roll Face Width (W)	
	Roll Surface Roughness (R_a)	

3.3 Direct Powder Rolling Experimental Setups for Stainless Steel 316L

The stainless steel 316L was chosen to be the initial powder material to investigate the powder rolling behaviors. The rolling experimental plan in Table 3.9 was designed based on the simulated powder rolling results from Johanson's model to conduct a parametric experimental study in various setups of powder rolling parameter combinations, including roll gap, roll face width, rolling speed and powder feeding rate. The rolling speed range was set to be 10, 12 and 14 rpm (maximum) since Johanson's model does not cover the rolling speed effect. According to the rolling pressure simulation, the roll gap range was set to be 0.5, 1 and 1.5 mm in order to obtain effective rolling pressure. Three sizes of hopper outlet diameter (1.5, 2, 2.5 cm) were used to investigate the feeding rate effect. The powder material volume was fixed at 200 ml for each trial.

Table 3.9: The planned experimental matrix of powder rolling setups in Stainless Steel 316L.

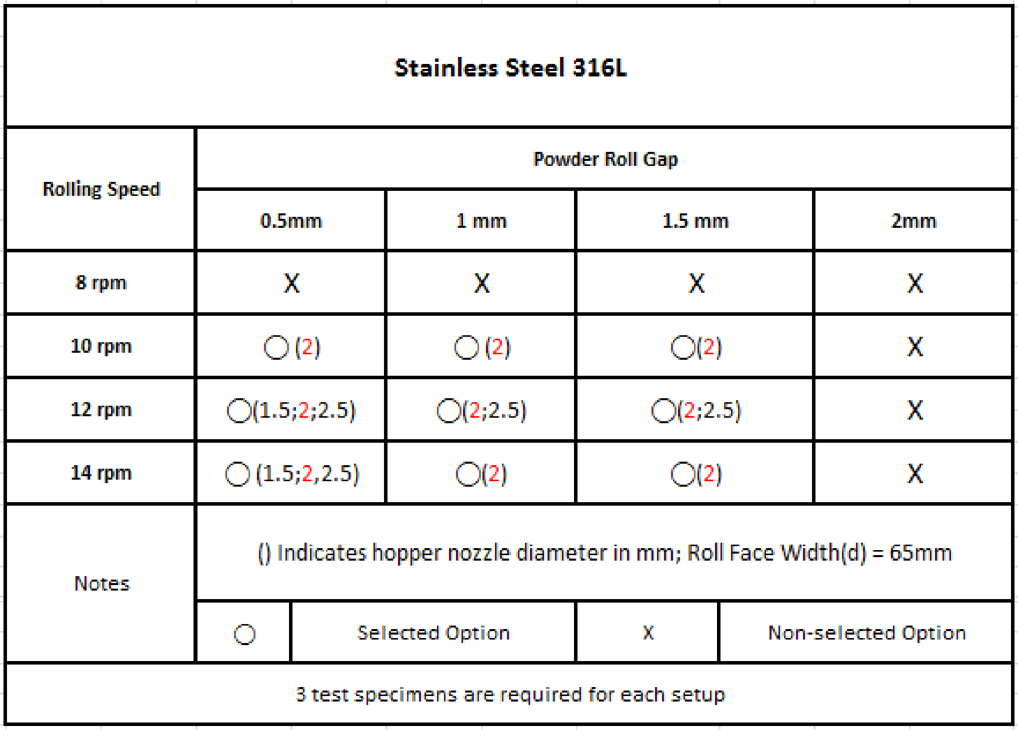

Stainless Steel 316L				
Rolling Speed	**Powder Roll Gap**			
	0.5mm	**1 mm**	**1.5 mm**	**2mm**
8 rpm	X	X	X	X
10 rpm	○ (2)	○ (2)	○(2)	X
12 rpm	○(1.5;2;2.5)	○(2;2.5)	○(2;2.5)	X
14 rpm	○ (1.5;2,2.5)	○(2)	○(2)	X
Notes	() Indicates hopper nozzle diameter in mm; Roll Face Width(d) = 65mm			
	○	Selected Option	X	Non-selected Option
3 test specimens are required for each setup				

3.4 Direct Powder Rolling Setups for CP-Titanium

The HDH CP-titanium powder rolling experiment was conducted based on the simulated maximum rolling pressure results from Johanson's model and the stainless steel 316L powder rolling experimental data. The experimental plan in Table 3.10 was designed to achieve the situation where CP-titanium powder can be rolled to its highest relative density and widest strip length (e.g. higher powder utility).

Table 3.10: The optimized experimental matrix of powder rolling setups in CP-titanium Powder.

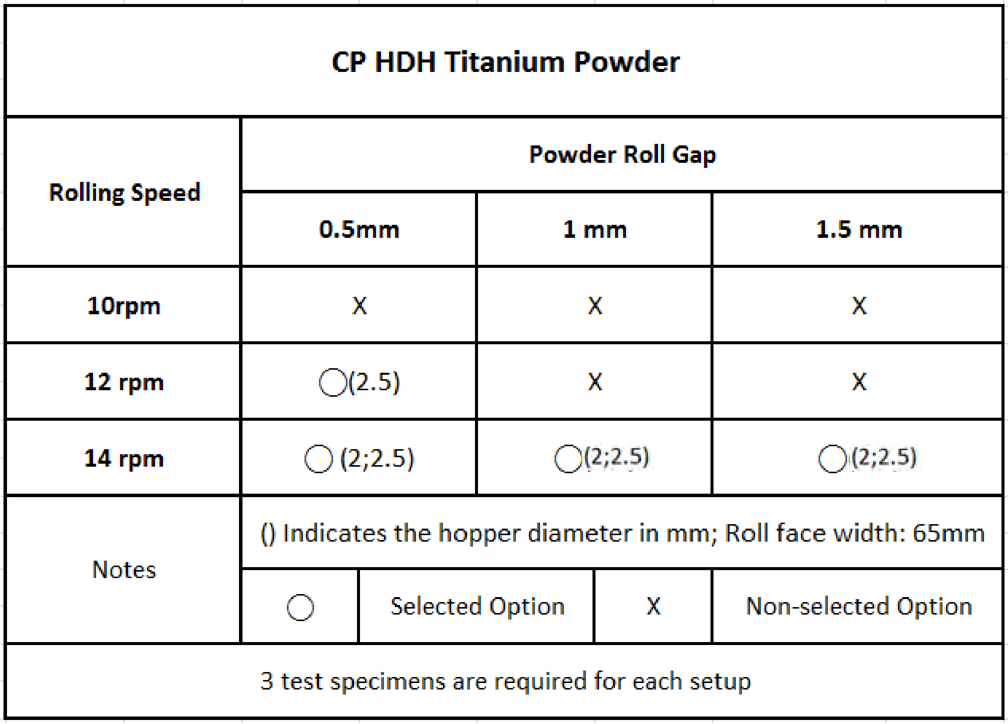

CP HDH Titanium Powder			
Rolling Speed	**Powder Roll Gap**		
	0.5mm	**1 mm**	**1.5 mm**
10rpm	X	X	X
12 rpm	○(2.5)	X	X
14 rpm	○ (2;2.5)	○(2;2.5)	○(2;2.5)
Notes	() Indicates the hopper diameter in mm; Roll face width: 65mm		
	○ Selected Option	X Non-selected Option	
3 test specimens are required for each setup			

In order to compare the rolling behavior of CP titanium and stainless steel powders, three roll gap sizes of 0.5, 1 and 1.5 mm were used in CP titanium powder rolling. However, only the highest rolling speed of 14 rpm and the hopper outlet diameters of 2 and 2.5 cm were applied in CP titanium powder rolling since high powder feeding rate and rolling speed enhance the relative density and strip width respectively. In particular, three optimized sets of rolling parameters (see Table 3.11) were employed at 0.5 mm initial roll gap to examine the relative density of CP titanium strip. Once again 200 ml of powder material was used for each trial.

Table 3.11: The detail of the three rolling parameters setups.

Rolling Parameter Set	Rolling Speed		Hopper Outlet Diameter		Roll Gap	Roll Face Width
	12 rpm	14rpm	2 cm	2.5 cm		
1	✓			✓	0.5 mm	65 mm
2		✓		✓	0.5 mm	65 mm
3		✓	✓		0.5 mm	65 mm

3.5 Sintering of CP-Titanium Green Strip

Four trials of each type of CP-titanium green strips which were produced according to the parameters in Table 3.12, were subjected to a sintering process for 2 hours at a temperature of 1200 °C in a vacuum environment of pressures lower than 10^{-3} Pa. The heating rate for sintering temperature was 300 °C/hour and the strip was allowed to furnace cool after the sintering process which is described in Table 3.13.

Table 3.12: Process parameters and physical property characteristics of selected CP titanium strips before sintering.

Green Titanium Strips	Rolling Parameters			Physical Properties			
	Rolling Speed (rpm)	Hopper Outlet Diameter (mm)	Roll Gap (mm)	Av. Strip Thickness (mm)	Av. Strip Width (mm)	Av. Strip Length (mm)	Av. Relative Density (%)
CP-Titanium 75 (Type 1)	14	2	0.5	2.2	52.0	350	75.6
CP-Titanium 85 (Type 2)	14	2.5	0.5	2.4	56.2	300	85.4

Table 3.13: Sintering parameters.

Material	Sinter Temperature	Heating Rate	Sintering Time	Vacuum
CP-Titanium	1200 °C	300°C/hour	2 hours	$< 10^{-3}$ Pa

3.6 Post-deformation Annealing of CP-Titanium Strip

One trial of each type of CP-titanium as-sintered strips which were produced according to the parameters in Table 3.12 and Table 3.13, were further deformed by 50% thickness reduction cold rolling and subjected to an annealing process for 30 minutes at a temperature of 750 °C in a vacuum environment of pressures lower than 10^{-3} Pa. The heating rate was controlled at 300 °C/hour and the cooling rate was performed by air cooling. The detail of the annealing process is shown in Table 3.14.

Table 3.14: The annealing parameters for cold rolled as-sintered CP-Titanium Strips.

Green CP-Titanium Strips	Relative Density of As-sintered Condition	Temperature of Annealing Process	Heating Rate	Heat Treatment Duration	Vacuum
CP-Titanium 75 (Type 1)	88%	750 °C	300 °C/hour	30 minutes	$< 10^{-3}$ Pa
CP-Titanium 85 (Type 2)	95%				

3.7 Tensile Testing for As-sintered and Post-Deformation Annealed CP-Titanium Strip

In order to evaluate any improvement in mechanical properties resulting from the as-sintered and post-deformation annealed CP-titanium strips, mechanical testing of processed material was required to measure its mechanical tensile properties including yield strength, ultimate tensile strength and plastic elongation. The ASTM E8/E8M – 09 [30] test methods for tension testing of metallic materials, where the tooling for creating the tensile specimens used in this research is detailed, involves fractures of the tensile specimens under a uniaxial load as shown in Figure 3.12.

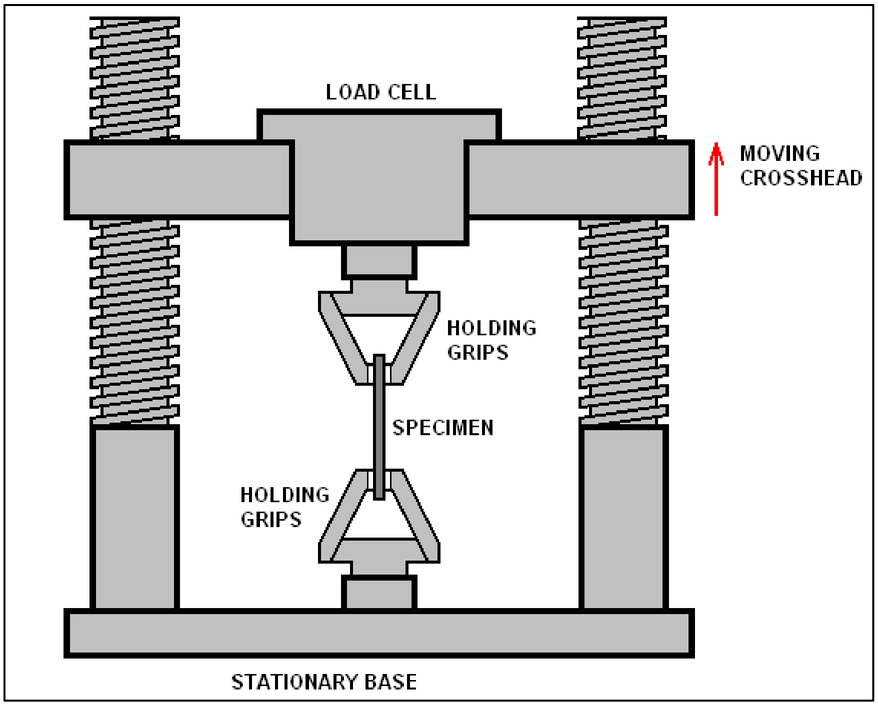

Figure 3.12: The tensile test fixture setup for CP-titanium specimens.

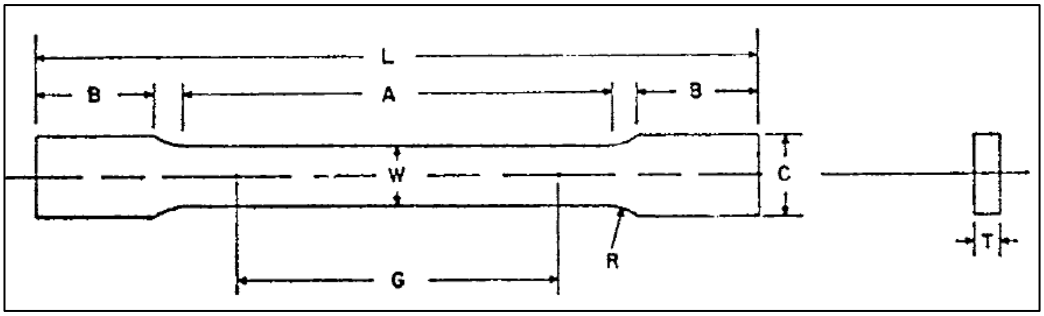

Figure 3.13: Geometry of rectangular tensile test specimen.

Table 3.15: The details of tensile test specimen dimensions.

Tensile Specimen Dimensions	
G – Gage length	25.0 ± 0.1 (mm)
W - Width	6.0 ± 0.1 (mm)
T- Thickness	Thickness of material (mm)
R – Radius of fillet	6 (mm)
Overall Length	100 (mm)
A – Length of reduced section	32 (mm)
B – Length of grip section	30 (mm)
C – Width of grip section	10 (mm)

The tensile testing was conducted on specimens from only as-sintered and post-deformation annealed CP-titanium specimens. The geometry of all the specimens that subjected to this test is given in Table 3.15 and Figure 3.13. A pre-load of 100N and initial strain rate of $1\text{x}10^{-3}\ s^{-1}$ was employed during the testing. The testing was carried out on a Zwick 1484 universal testing frame equipped with a 200 kN load cell.

Creating the Tensile Testing Specimens

One tensile testing specimen was created from the middle section of each as-sintered CP-titanium strip and three tensile testing specimens were created from the middle section of each post-deformation annealed strip according to the specimen geometry given in Table 3.15 and Figure 3.14. The details of the number of machined specimens is shown in Table 3.16.

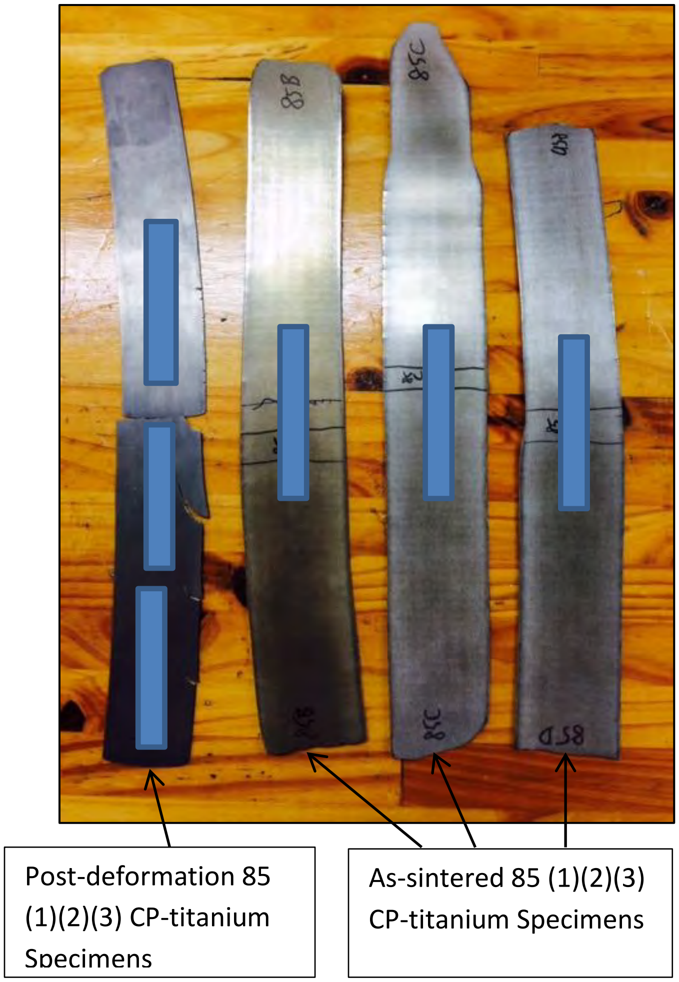

Figure 3.14: The schematic of creating tensile specimens from CP-titanium strips (the rectangular blocks indicate the positions of the tensile specimens).

Table 3.16: The details of the expected tensile specimens.

Material Condition	Quantity of Tensile Specimens		
	Number of Created Strips	Number of Created Specimens from each strip	Total number of specimens
As-sintered 75 (type 1)	3	1	12
As-sintered 85 (type 2)	3	1	
Post-deformation Annealed 75 (type 1)	1	3	
Post-deformation Annealed 85 (type 2)	1	3	

Analysis of Stress-Strain Curve from Tensile Test

The obtained data from tensile test was further imported to Excel for analyzing mechanical tensile properties. The measured terms are defined from the diagram in Figure 3.14 below.

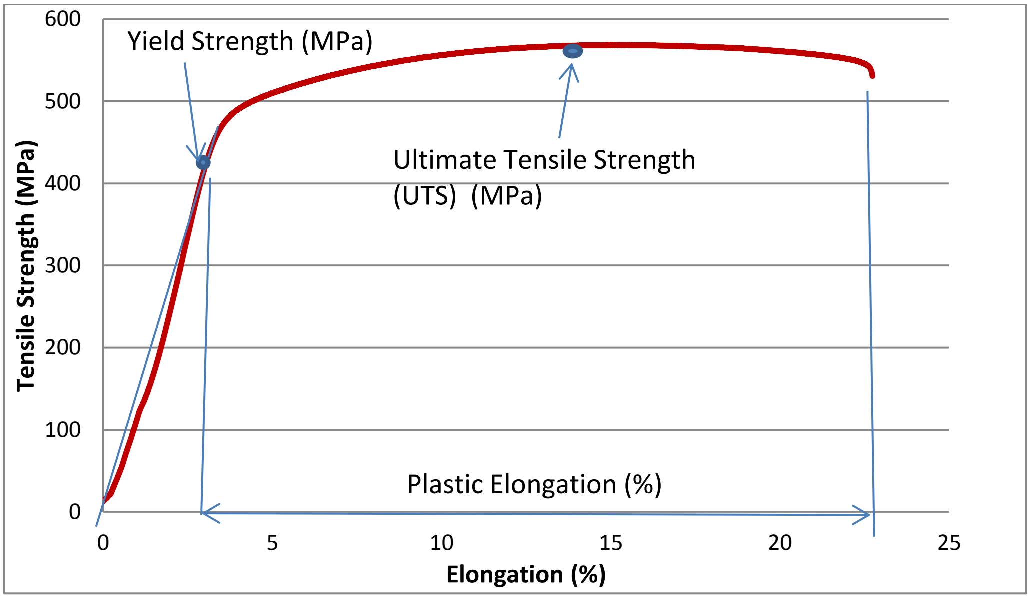

Figure 3.15: The diagram of analyzing tensile properties from stress-strain curve.

Chapter 4

Results and Discussion of Direct Powder Rolling

4.1 Powder Characteristics

4.1.1 Cold Uniaxial Pressing

Pressure-Density Curve for Stainless Steel

The powder characteristics data was tested at the Light Metals Division, CSIR, Pretoria. As expected the results demonstrate an increase in density with increasing applied pressure as shown in Figure 4.1 within a logarithmic trend line below. The compressibility curve for stainless steel 316L in a logarithmic plot is shown linearly in Figure 4.2 and images of the compacts are shown in Figure 4.3. Except for the 100 bar pressed sample which showed signs of disintegrating, all the other samples were strong enough for subsequent handling. The density value for the 100 bar sample is not accurate due to the sample disintegrating.

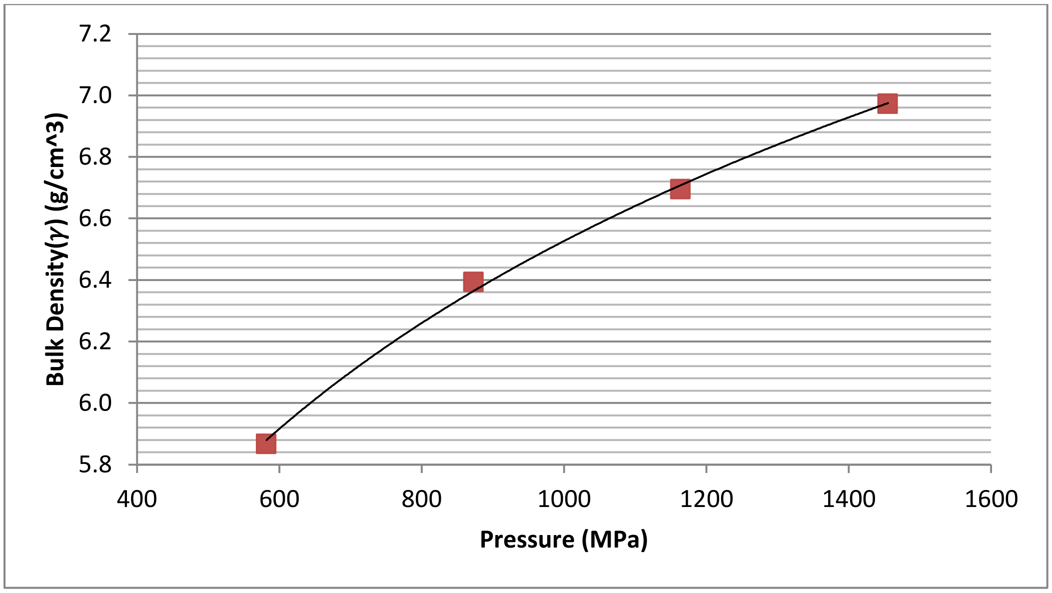

Figure 4.1: Compressibility curve for stainless steel 316L.

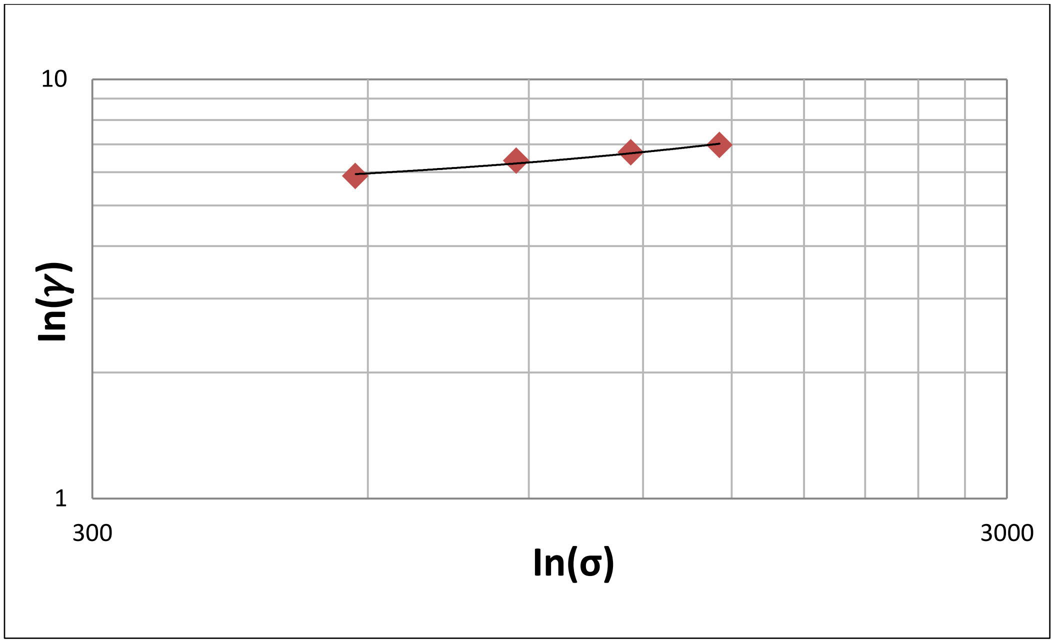

Figure 4.2: Compressibility curve for stainless steel 316L in logarithmic plots.

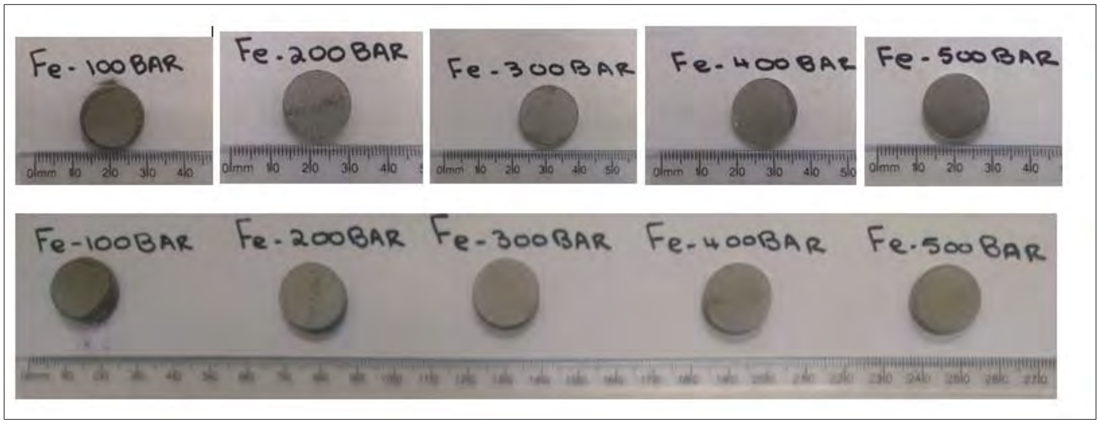

Figure 4.3: Photographs of stainless steel 316L.

Pressure-Density Curve for CP-Titanium

The cold uniaxial pressing test results have shown an increase in density with increasing applied pressure as shown in Figure 4.4 within a logarithmic trend line below. The compressibility curve for CP-titanium powder in logarithmic scale is given linearly in Figure 4.5 and images of the compacts are shown in Figure 4.6.

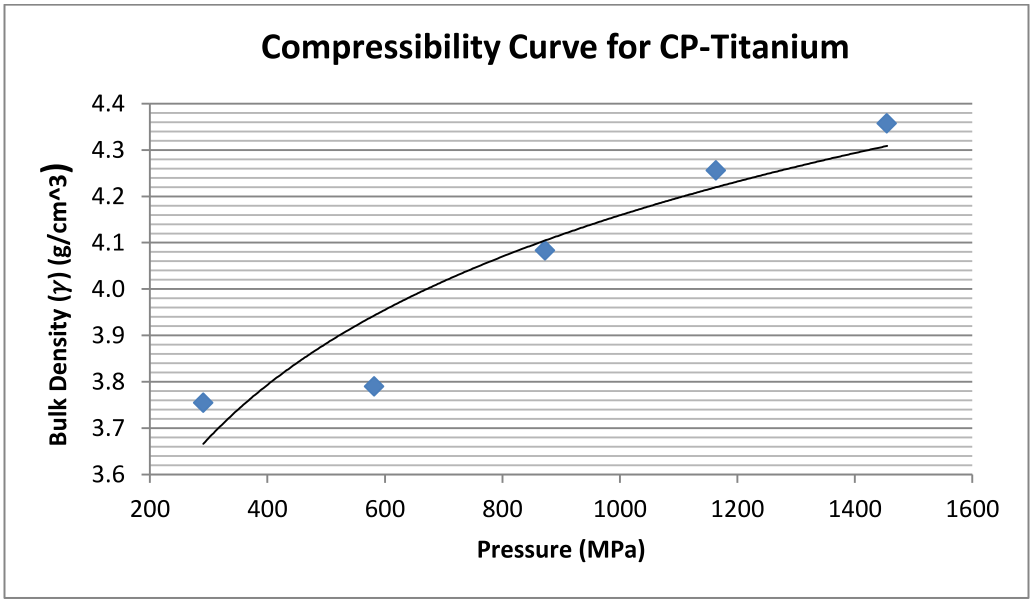

Figure 4.4: Compressibility curve for CP-titanium powder.

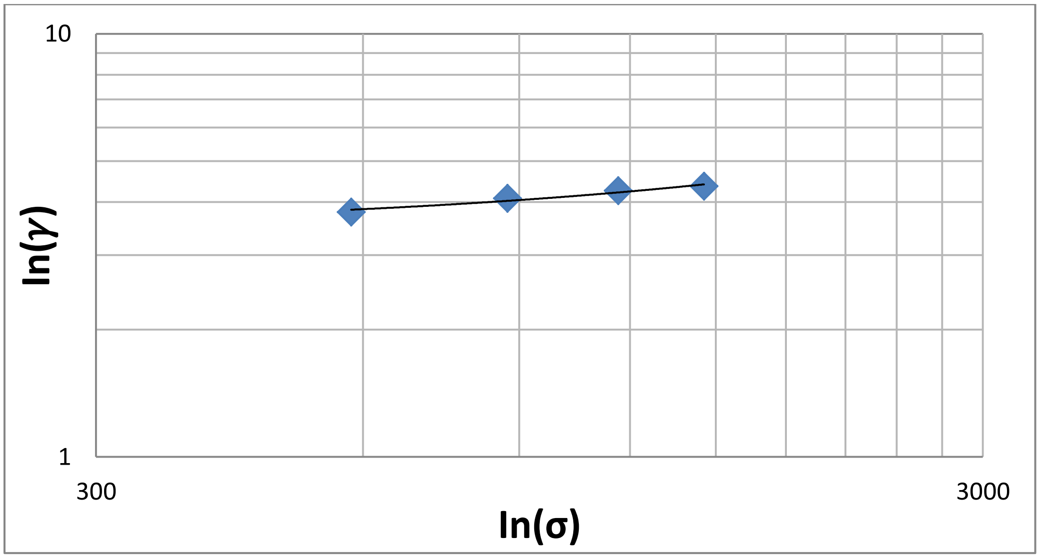

Figure 4.5: Compressibility Curve for CP-titanium powder in logarithmic plots.

Figure 4.6： Photographs of CP-titanium compacts.

Table 4.1 the calculated compressibility factor of CP-titanium and stainless steel 316L powder.

Material	CP-Titanium (Ti)	Stainless Steel 316L (Fe)
Compressibility Factor (K)	6.83	5.30

Two different metal powders have both shown reasonable high compressibility from Figure 4.1 and 4.4. In particular, the CP-titanium compacts have approximately 8-9% higher relative density than the stainless steel compacts under the same pressing load. The calculation of the value of K still has some degrees of uncertainty since the slope of the pressure-density curve turns to be zero when a large pressing load is applied. With regard to the rolling pressure modelling, the pressure range of the pressure-density curve was selected to be consistent with the actual pressure range of the CME rolling mill. Furthermore, the measured pressure-density curve can determine the required pressure of the rolling setup for the desired relative density of the metal powder compacted strip.

4.1.2 Powder Shear Test Results

The shear test was carried out on both CP-titanium (Ti) and stainless steel (Fe) and each test was repeated three times. Graphical analysis and abbreviations of the shear test results and test data are shown in Figure 4.5 and Tables 4.2 and 4.3.

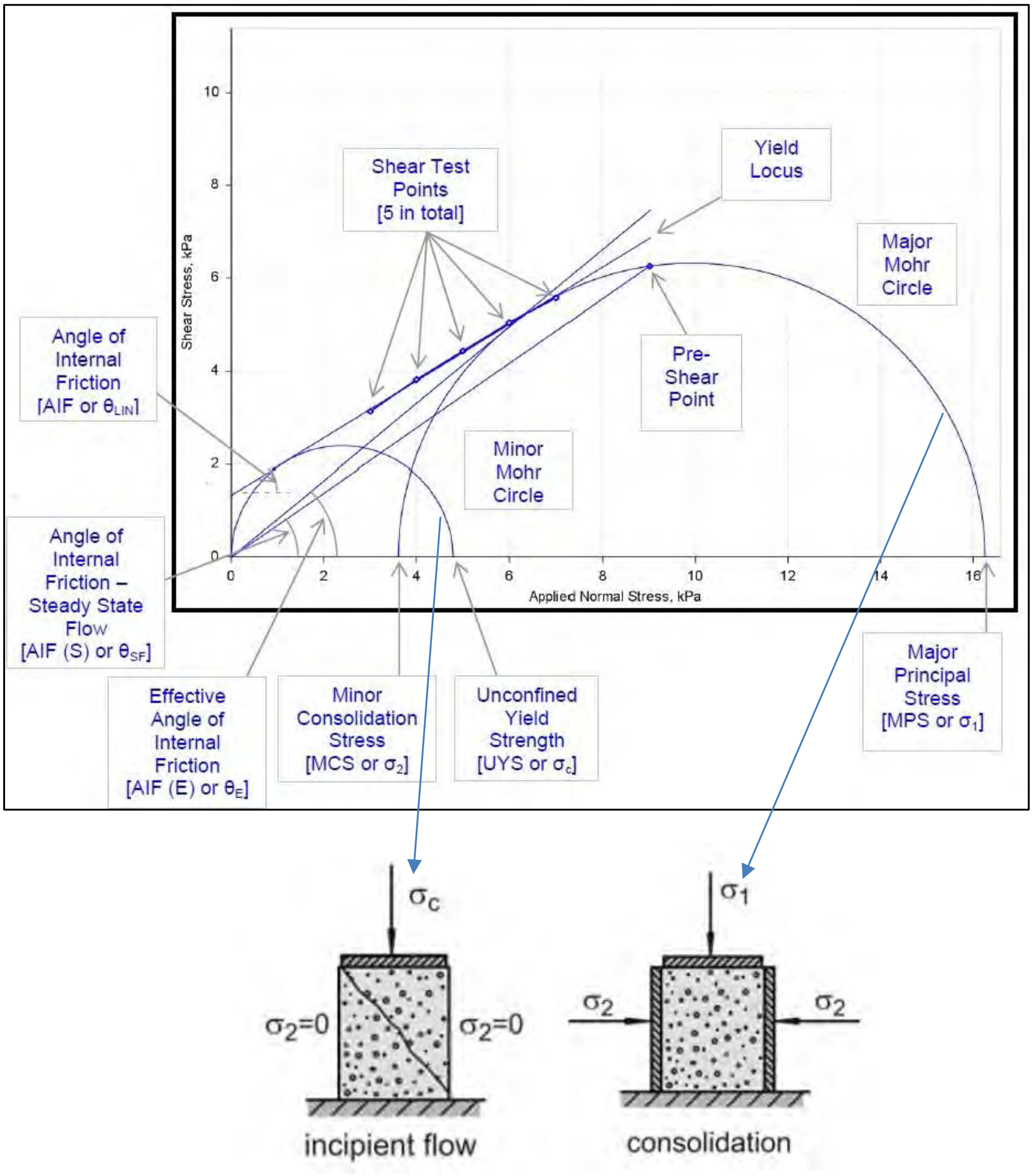

Figure 4.7: Graphical Analysis of Shear Cell Test Results[31].

Refer to Figure 4.7, the major mohr circle describes the stresses in the bulk solid sample at consolidation state, with the major principal stress σ_1 acts vertically and the minor principal stress σ_2 is the normal stress acts horizontally on the bulk material sample. The small mohr circle that cuts through the origin describes the stress in the bulk solid sample at unconfined state after it is consolidated, the incipient flow of the sample is occurred due to the load σ_c corresponding to this Mohr stress circle. Once the Mohr stress circle reaches the yield limit (failure), no larger load could be exerted on the sample. The use of the uniaxial compression test with bulk material to measure the yield locus is problematic, because one obtains unconfined yield strength values that are too low [31]. Therefore, the shear test is introduced by Jenike [23] to solve this problem, the bulk material is consolidated by a vertical normal load with increasing shear stress instead of a uniaxial load which leads the resultant force acting on the sample to increase, is called pre-shear point (consolidation). The consolidated bulk material is subsequently loaded within a defined normal stress (lower than the consolidated normal stress) with increasing shear stress to reach its incipient flow (failure), is called "shear to failure" or shear test point. The trend line of each shear test point is the yield locus of the bulk material.

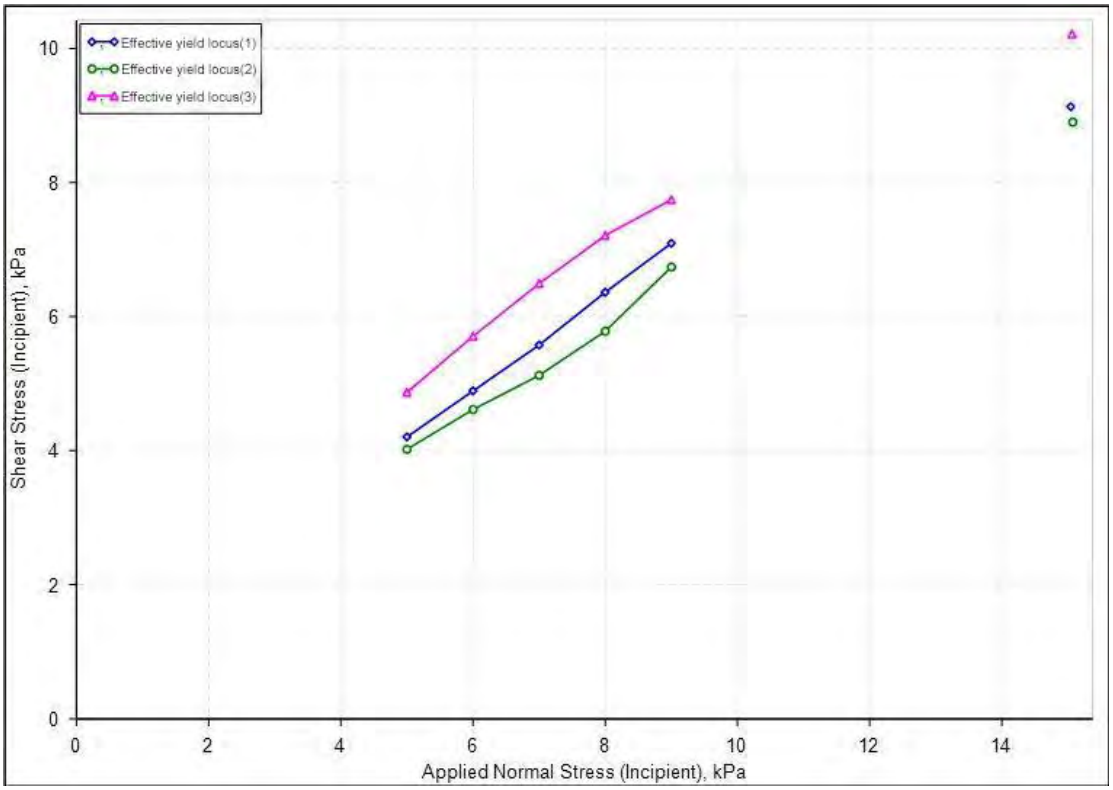

Figure 4.8: Yield loci for Stainless Steel 316L.

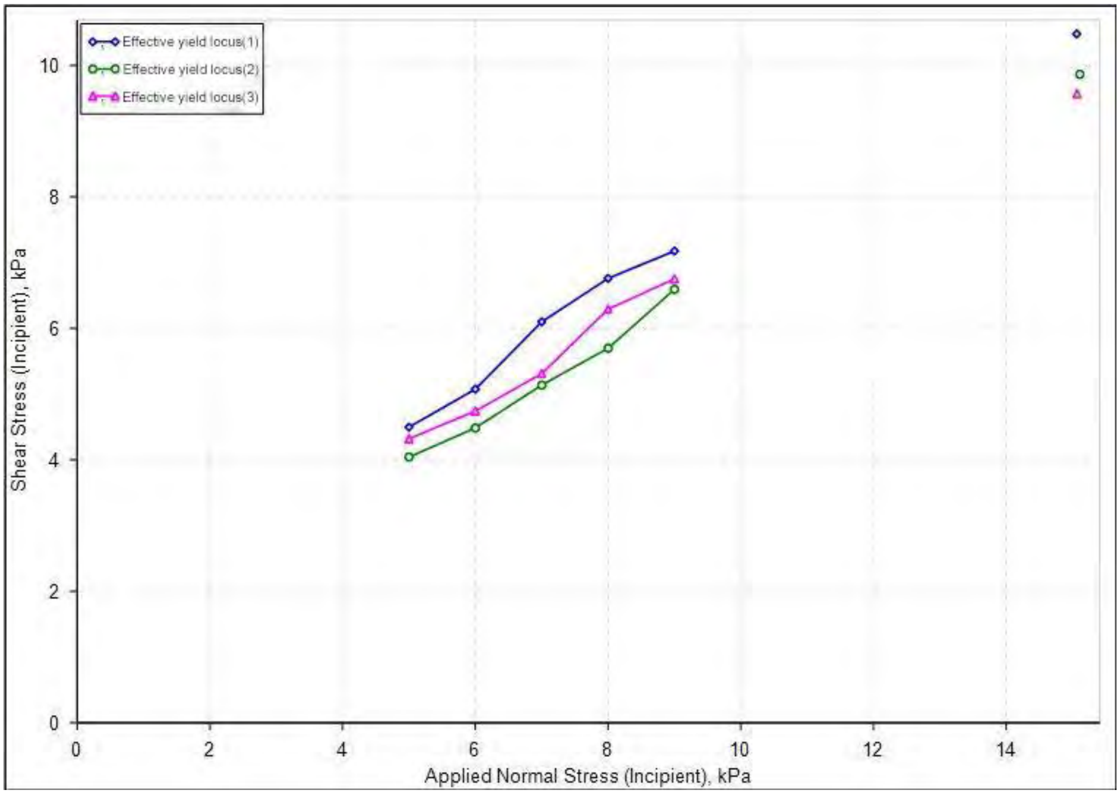

Figure 4.9: Yield locus for CP-titanium.

Table 4.2: The shear test results for stainless steel 316L powder.

Series Name	Material	UYS,KPa	MPS,KPa	MCS,KPa	AIF(E), º	Ave.AIF(E), º	BD,g/ml
Effective Yield Locus(1)	Fe	2.16	23.93	5.67	38.10	38.31	3.32
Effective Yield Locus(2)	Fe	2.30	24.09	6.28	35.89		3.32
Effective Yield Locus(3)	Fe	5.30	25.84	5.38	40.95		10.83

Table 4.3: The shear test results for CP-titanium powder.

Series Name	Material	UYS,KPa	MPS,KPa	MCS,KPa	AIF(E), º	Ave.AIF(E), º	BD,g/ml
Effective Yield Locus(1)	Ti	3.97	27.90	6.51	38.44	36.51	1.85
Effective Yield Locus(2)	Ti	2.69	28.27	7.71	34.84		1.79
Effective Yield Locus(3)	Ti	3.60	25.96	6.67	36.26		0.72

Symbols and parameters are indicated as follows:

UYS – Unconfined Yield Strengthσ_c

MPS – Major Principal Stress σ_1

MCS – Minor Consolidation Stress σ_2

AIF(E) – Effective Internal Friction Angle θ_{E}

BD – Bulk Density γ

As the shear test results shown in Figure 4.8 and 4.9, the data shows significant scatter, and this is due to both powder materials are highly susceptible to slip-stick behavior. This has been corrected by improving the repeatability of the measured shear stresses. 'Average Peaks of Last 10%' is designed to address the variability in slip-sticking incipient failure, and makes these three results even more repeatable in terms of measured shear stresses. Moreover, The variation in bulk density (BD) as shown in Table 4.3 is due to a weighing error taking place, in which the split mass appeared to be 10 g below the split mass for the other two samples. This difference is consistent with the mass of the funnel and it may not have been removed at the correct point in the splitting procedure. However, this error only introduced variability in the bulk density and the other parameters are unaffected. It is common that high variability can occur in derived parameters such as Cohesion, UYS, MPS and AIF when the measured parameters show that the results are actually quite repeatable.

4.1.3 Wall Friction Test Results

Wall friction test was carried out on both CP-titanium (Ti) and stainless steel (Fe) and each test was repeated three times. Graphical Analysis of shear test results and test data were shown in Figure 4.10 and 4.11, and Table 4.4, 4.5.

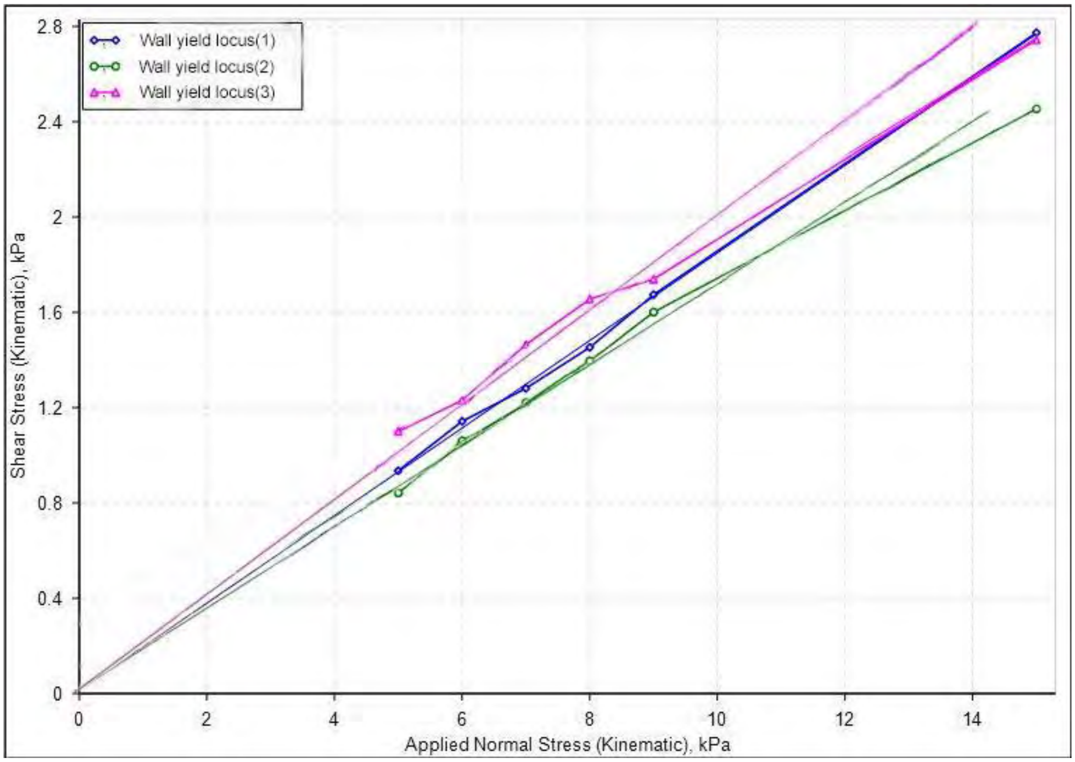

Figure 4.10: Yield loci for Stainless Steel.

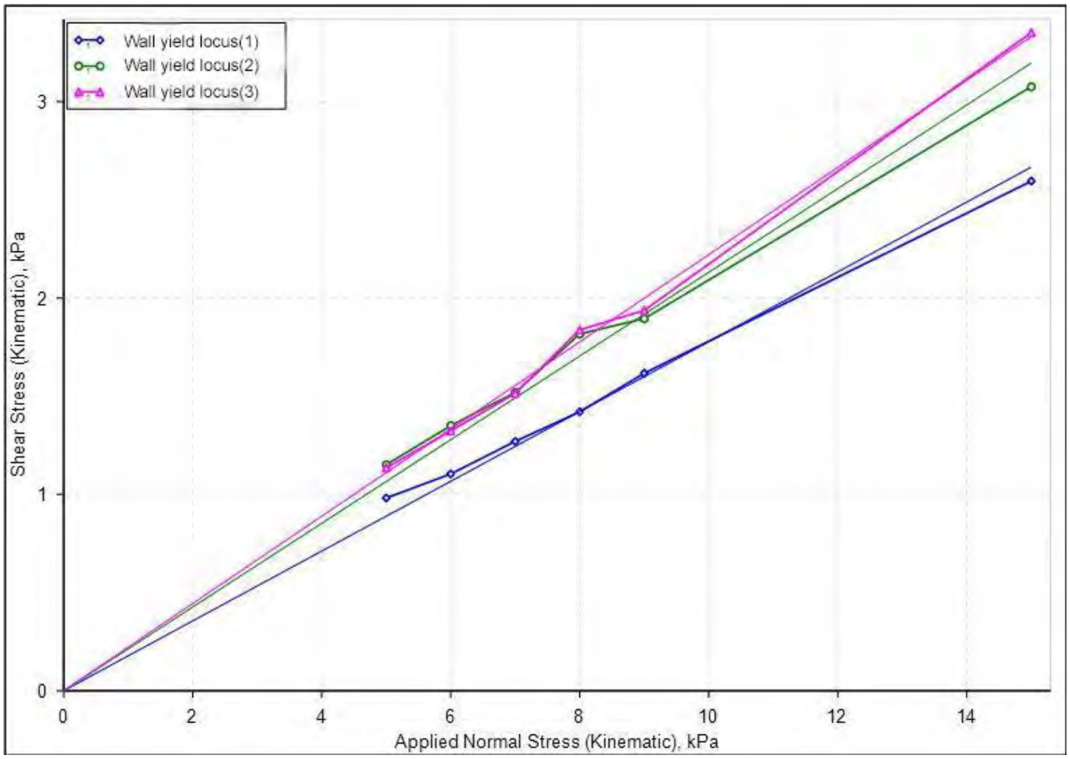

Figure 4.11: Yield loci for Titanium.

Table 4.4: The Wall friction test results for stainless steel 316L (Fe).

Series Name	Material and Batch	WFA, º	Ave. WFA, º	BD, g/ml
Wall Yield Locus (1)	Fe	10.41	9.58	3.29
Wall Yield Locus (2)	Fe	9.01		3.29
Wall Yield Locus (3)	Fe	9.34		3.23

Table 4.5: The Wall friction test results for CP-titanium (Ti).

Series Name	Material and Batch	WFA, º	Ave. WFA, º	BD, g/ml
Wall Yield Locus (1)	Ti	9.30	10.91	1.76
Wall Yield Locus (2)	Ti	10.88		1.84
Wall Yield Locus (3)	Ti	12.58		1.89

4.2 Johanson Rolling Model Implementation

The powder rolling model was developed through the Matlab platform according to Johanson's theory. The rolling mill geometrical data was imported from the CME powder rolling mill. The geometrical symbols and parameters are indicated in Figure 4.10.

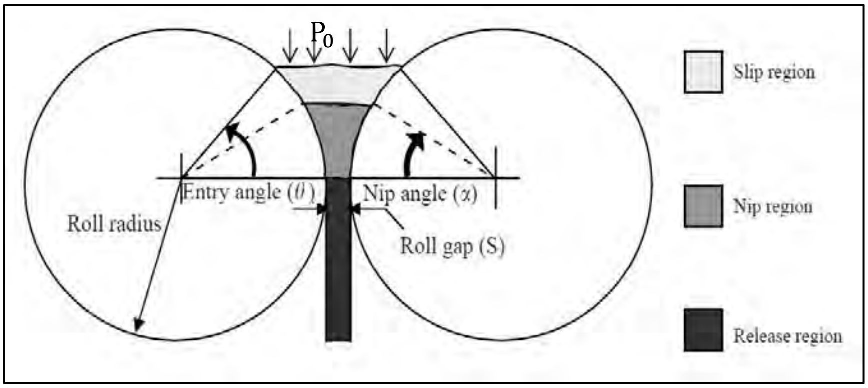

Figure 4.12: Roll Press.

Symbols and parameters are indicated as follows:

S - Roll Gap Size

D = Roll Diameter

K = Compressibility Factor (powder characteristics)

δ= Effective internal Friction Angle (powder characteristics)

μ = friction Coefficient (roll surface)

P_o = Powder Feed Pressure

α = Nip Angle (the effective compaction roll angle)

RW = Roll Face Width

4.2.1 Determination of Nip angle

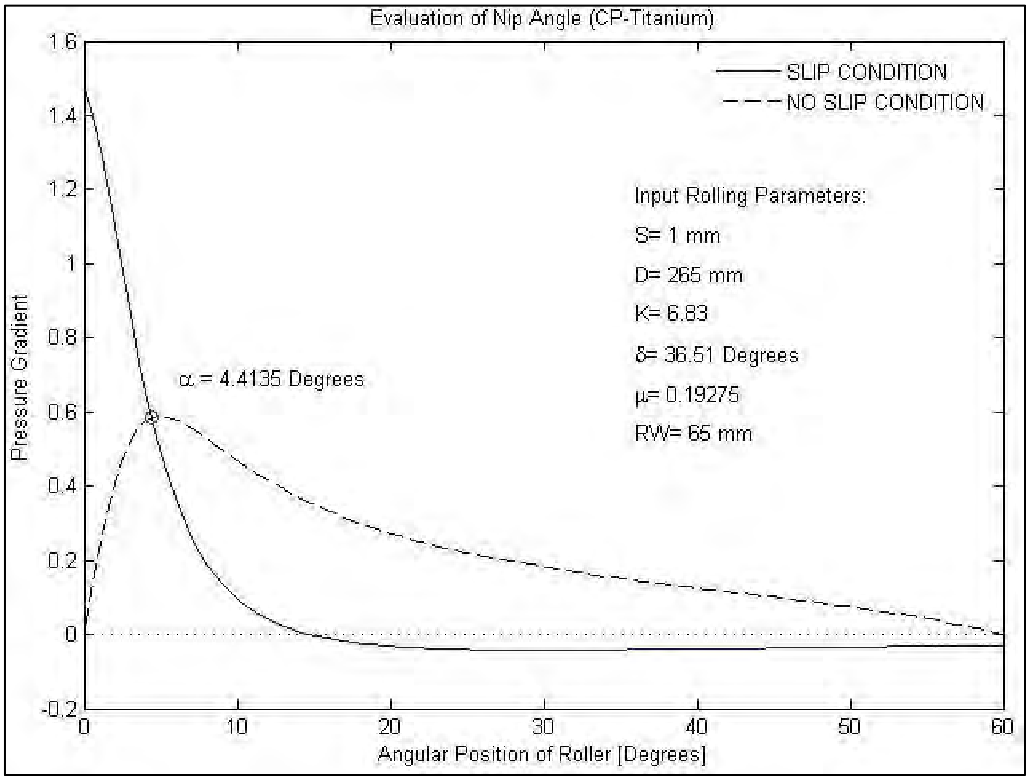

Figure 4.13: Determination of nip angle for CP-titanium.

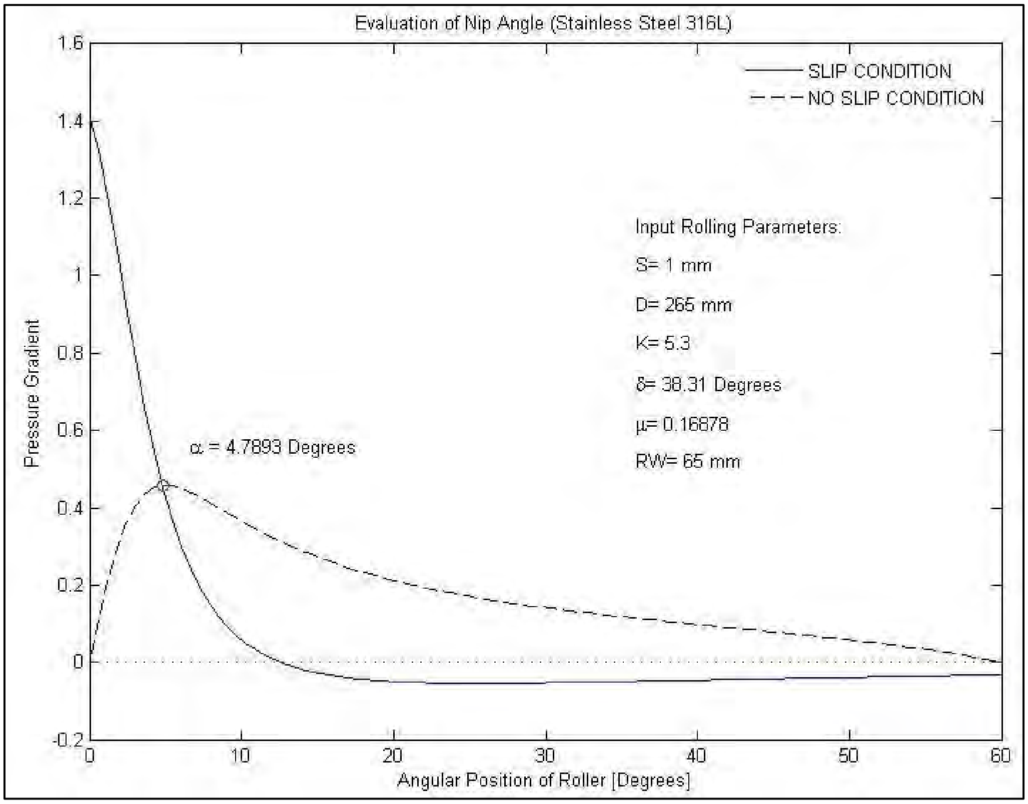

Figure 4.14: Determination of nip angle for stainless steel 316L.

The starting point of compaction or nip region was determined from the intersecting point of slip and no slip curve which is shown in Figure 4.13 and 4.14 for both stainless steel 316L and CP-titanium powder. For the 1 mm roll gap scenario, the nip angles for CP-titanium and stainless steel 316L rolling were found as 4.4 and 4.8 degrees, respectively. The main input parameters that influence the nip angle are effective internal friction angle δ, wall friction angle ϕ and compressibility factor K. In particular, a larger effective internal friction angle and wall friction angle leads to a larger nip angle, but a larger compressibility factor gives a smaller nip angle. The change in roll gap has been found to have nearly no significant effect on the nip angle since the gap size is relatively small compared to the roll diameter and the term of S/D in the pressure equation turns towards zero.

4.2.2 Maximum Rolling Pressure Simulation

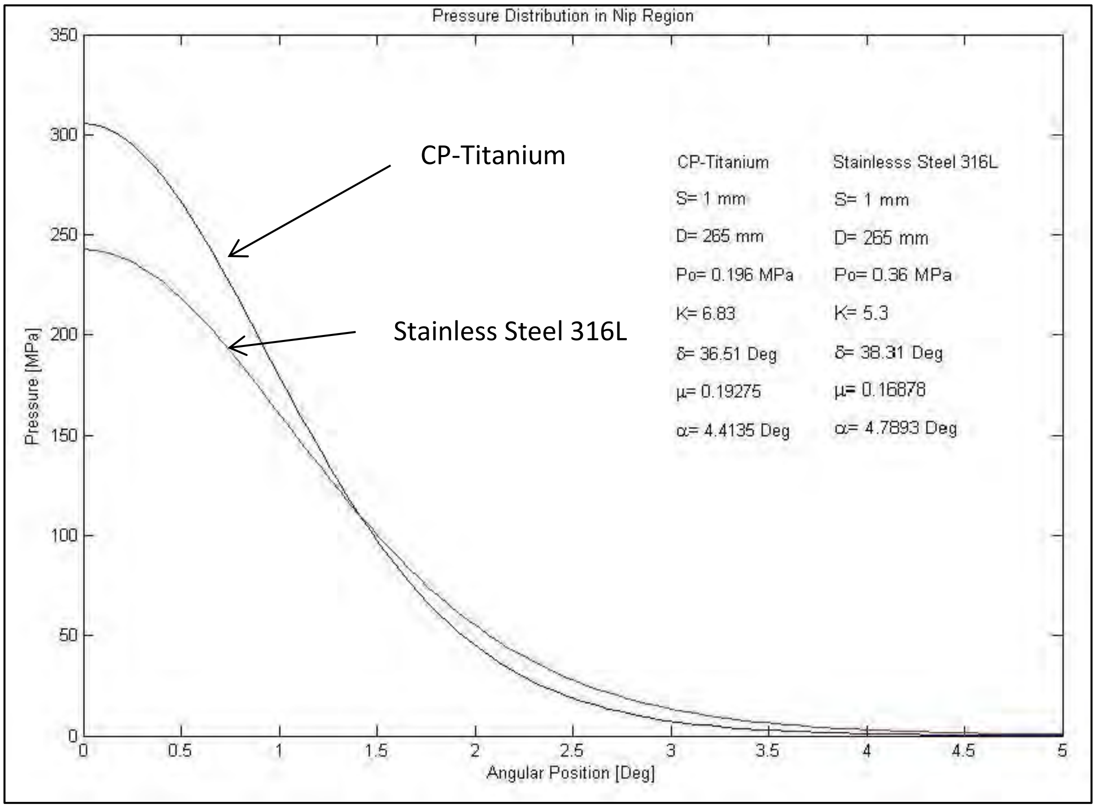

Figure 4.15: The roll pressure distribution in compaction region when roll gap = 1 mm.

The rolling pressure distribution curve in Figure 4.15 was implemented at 1 mm roll gap after the nip angle is defined. The feed pressures for both CP-titanium and stainless steel powder were estimated based on the results of Simon and Guigon [32] (see Appendix), since no piezoelectric transducers are equipped in the rolling mill of this dissertation. The results have shown that the maximum rolling pressure for CP-titanium and Stainless steel 316L bulk material are 318 MPa and 243 MPa Respectively. This also helps to understand that the formability or utility of stainless steel powder rolling is lower than that for the titanium powder rolling compaction. According to Johanson's model, the pressure distribution difference is mainly dependent on the powder characteristics, such as particle size, internal friction, flowability and compressibility.

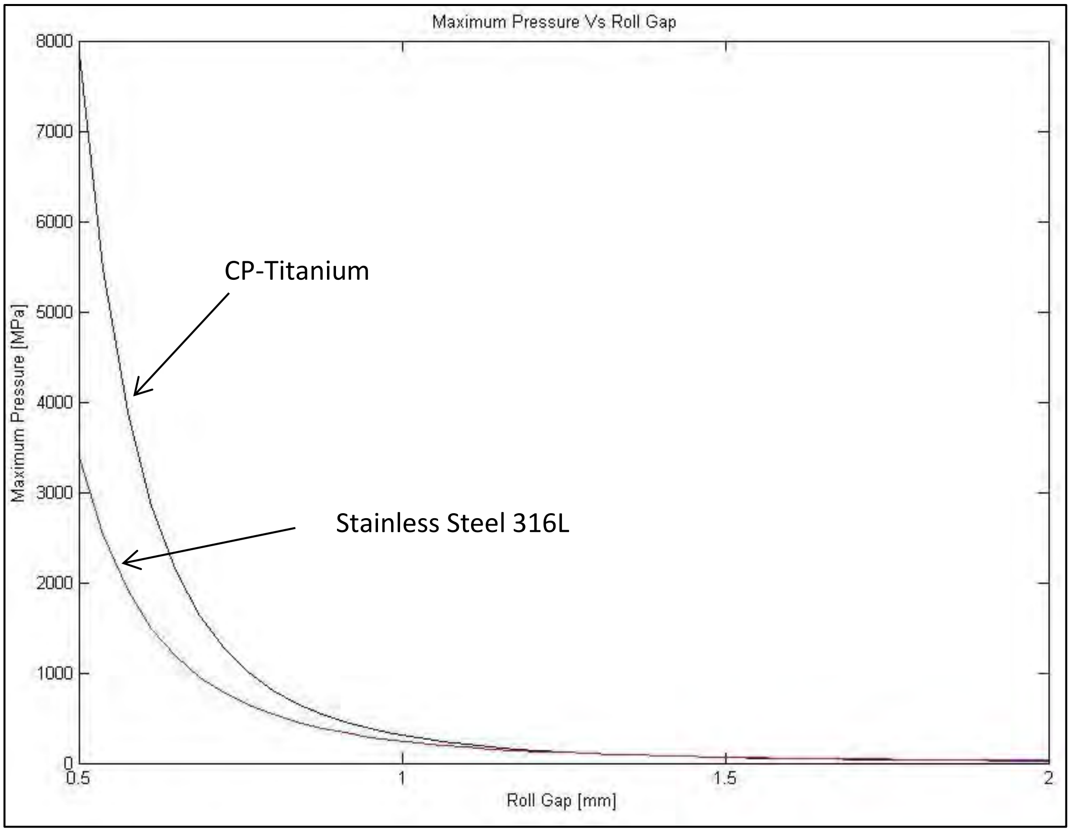

Figure 4.16: The maximum roll pressure vs roll gaps.

In order to simulate the roll gap effect on the maximum rolling pressure, the relationship of maximum rolling pressure and roll gap was established in Figure 4.16. The roll gap range was only focused on 0.5 mm to 2 mm. The reason is due to the fact that the rolling mill was overloaded if the roll gap is smaller than 0.5 mm and the green strip was not formed during rolling compaction if the roll gap is bigger than 2 mm. The results have shown that the maximum roll pressure was increased as the roll gap decreases. In particular, maximum compaction pressure for CP-titanium and stainless steel 316L powder rolling was approximately 8000 MPa and 3300 MPa at the roll gap of 0.5 mm respectively. However, Johanson's model does not take account of material yield condition so that the maximum pressures of 8000 MPa and 3300 MPa will not be appeared in experimental results and the powder material would not be able to withstand such high pressures and undergo plastic deformation. This simulated pressure result can be further explained by the fact that the formation of edge cracks of CP-titanium strip at roll gap below 0.5 mm during the rolling experiment.

4.2.3 Maximum Rolling Pressure Analysis

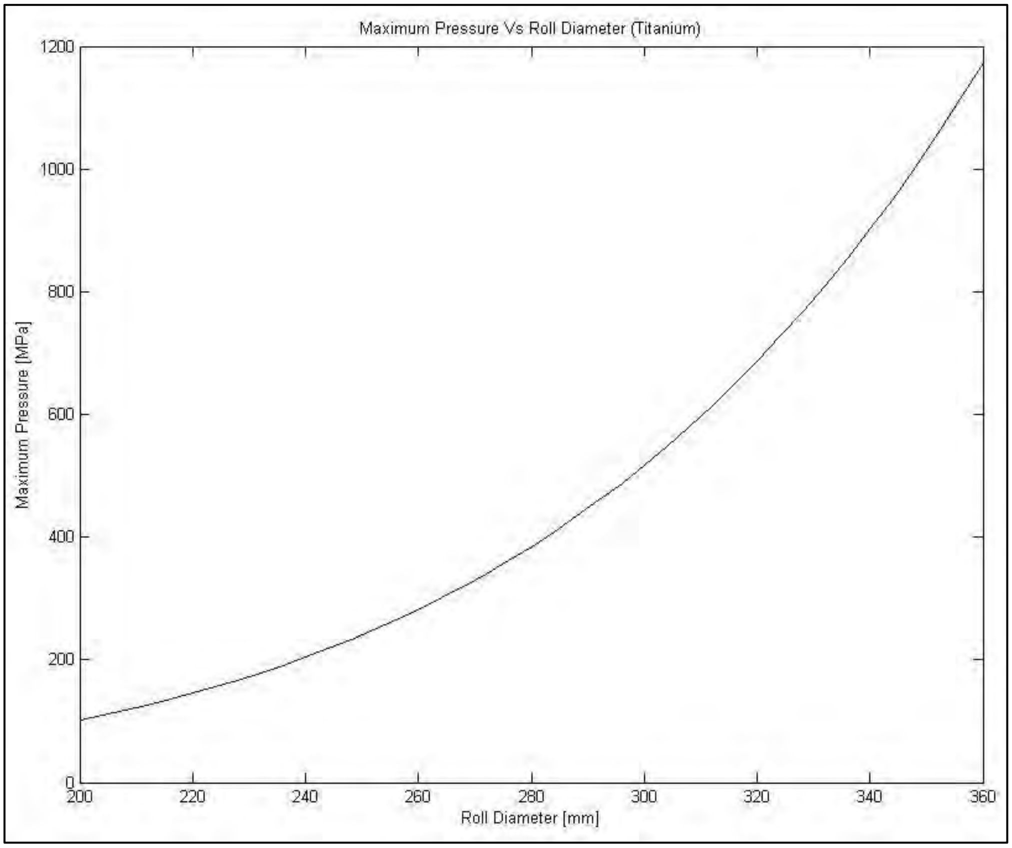

Figure 4.17: The size of roll diameter effect on the maximum roll pressure for CP-titanium at roll gap of 1 mm.

From the point of view of rolling mill design perspective, the relationship of roll diameter and roll pressure was established in Figure 4.17. The results have shown that the maximum roll pressure was increased as the roll diameter increases. This model is capable to determine the required minimum roll diameter for desired maximum rolling pressure in specific metal powder material. In other words, it helps to design a rolling mill or process that produces the powder compacted strip of specific thickness, width and density and also explains the statement of the roll diameter is 50 to 150 times larger than the rolled strip thickness from Evans and Smith [22].

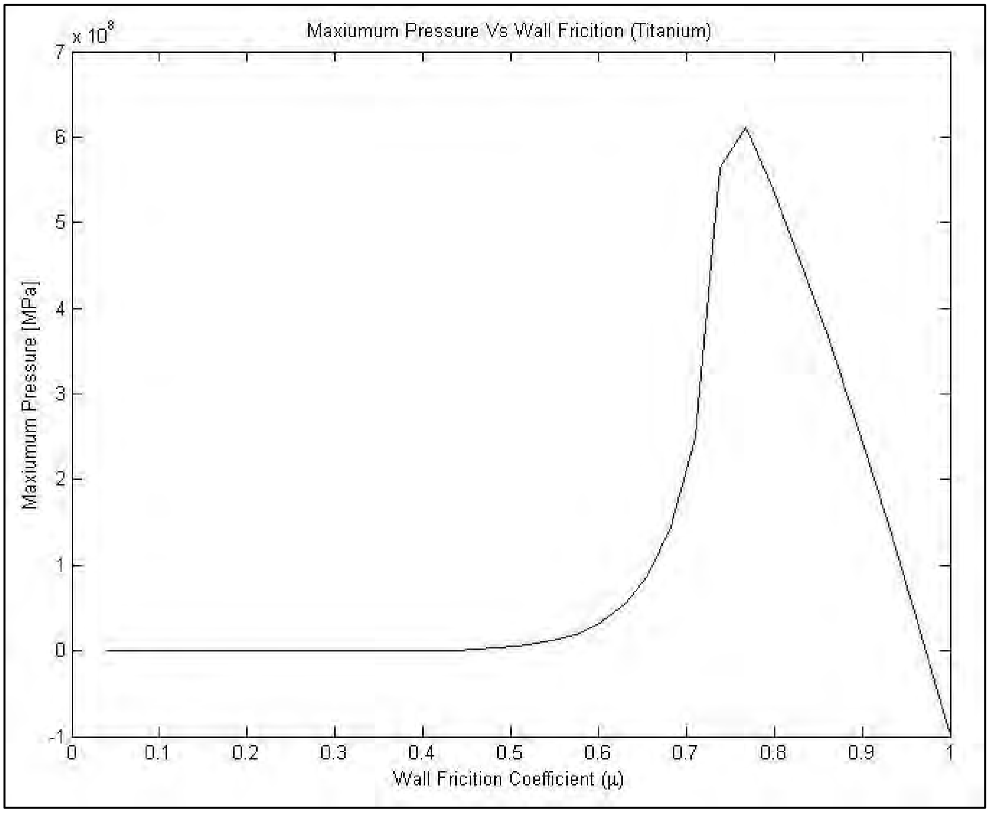

Figure 4.18: The maximum roll pressure versus the wall friction coefficient (roll surface roughness) for CP-titanium at 1 mm roll gap size.

One of the objectives is to understand the roll surface roughness effect on the maximum rolling pressure. Rough rolls increase the force that drags the bulk solid material into the nip region, and as a result of Johanson's assumption of the mass conservation, a denser strip is expected resulting from an increase in maximum pressure. The graph in Figure 4.18 establishes the relationship between the maximum pressure and the wall friction coefficient μ. It would be easy to misunderstand that the wall friction coefficient will always increases the rolling pressure at a constant rate since the normal force is proportional to the frictional force on the roll surface. In fact, this curve reaches its peak point at coefficient value of 0.78 and then the maximum pressure starts to drop back to zero. That is because the increase of friction coefficient not only increases the normal force on the roll surface, but also enlarges the nip angle and the nip region. Therefore, the rate of this area increase is greater than the rate of increase of roll force once the wall friction coefficient of 0.78 is reached, and then the pressure decreases eventually. It helps to design the roll surface roughness when the specific maximum pressure is required.

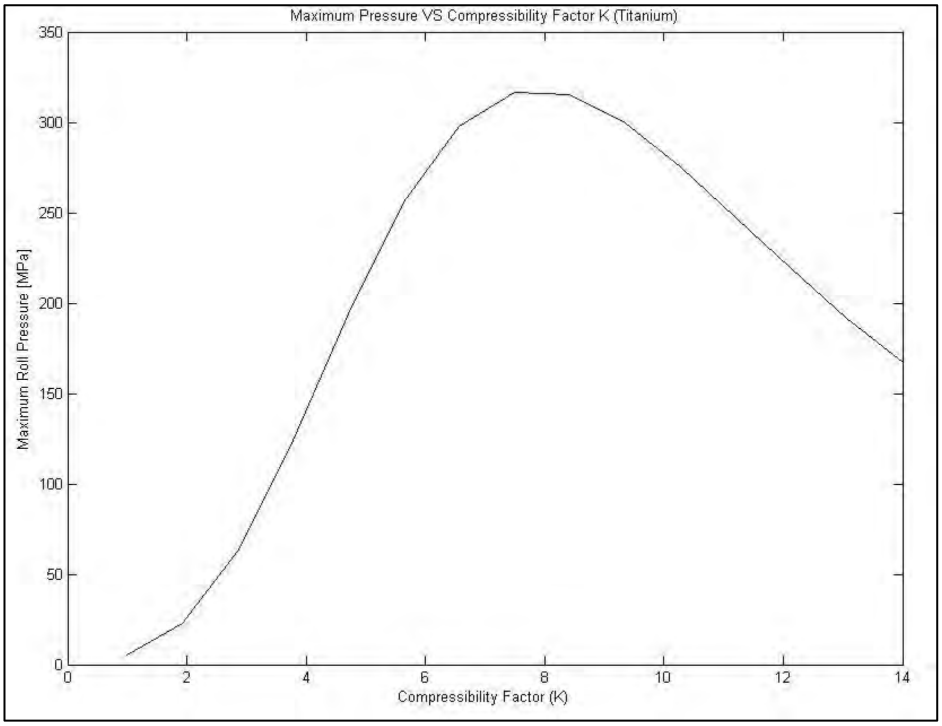

Figure 4.19: The relationship between maximum roll pressure and compressibility factor K for CP-titanium (at roll gap of 1mm).

The relationship of maximum roll pressure and compressibility factor K was similar to the wall friction effect on the maximum roll pressure, whereby the observed curve in Figure 4.19 starts to reverse its trend after a certain peak point. This is a model phenomenon which can be explained by the relationship between the rate of change in compressibility factor and the rate of change in nip angle. As the compressibility factor K increases the nip angle decreases (see

Figure 4.21). Therefore, if the rate of decrease in nip angle is greater than the rate of increase in compressibility factor K, and then the maximum rolling pressure starts to decrease since a decrease in nip angle reduces the rolling pressure (see Figure 4.22). Although it is very difficult to predict the point where the curve starts to decay since it also depends on the geometry dimensions of the rolling mill and the characteristic parameters of the powder, the most valuable result from Johanson's model is to find the nip angle.

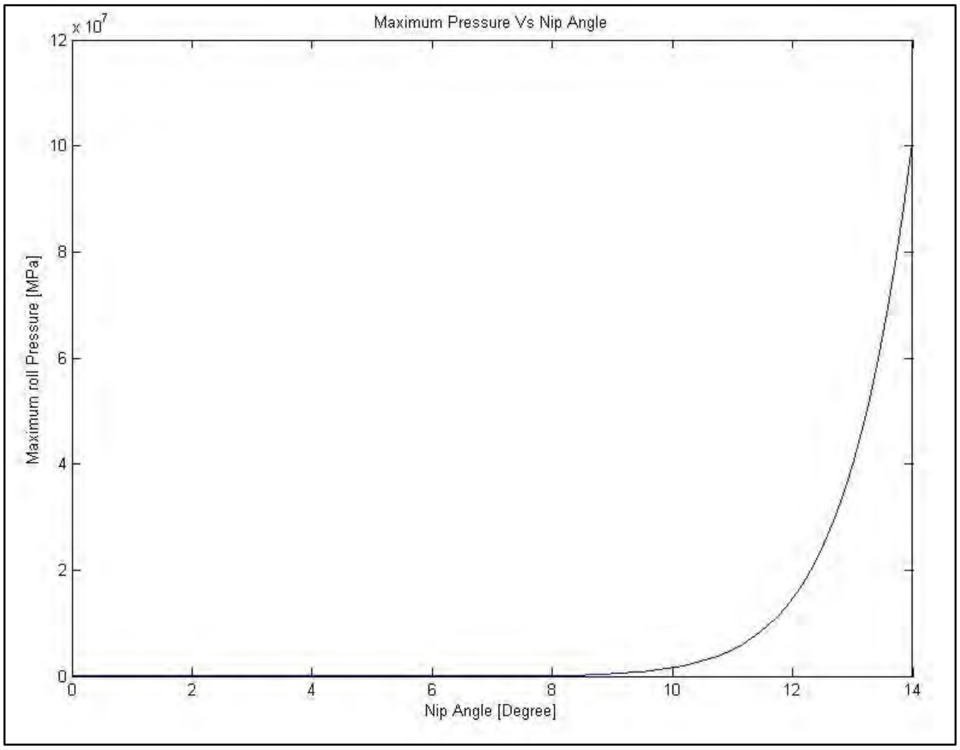

Figure 4.20: The relationship between maximum roll pressure and nip angle (at roll gap of 1mm).

The relationship between maximum roll pressure and nip angle is given in Figure 4.20. As can been seen from this graph, the maximum roll pressure is increased as the nip angle increases. In fact, there is nearly no significant change in maximum roll pressure when the nip angle is within the 0 – 8 degrees, and then the maximum roll pressure is increased dramatically when the nip angle exceeds at a certain transient point.

4.2.4 Nip Angle Analysis

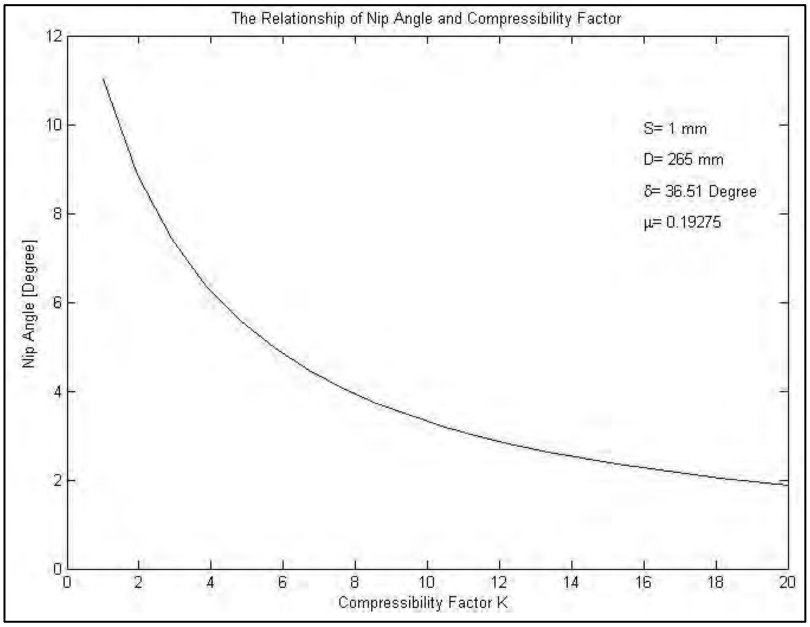

Figure 4.21: The relationship between nip angle and compressibility factor K (at roll gap of 1mm).

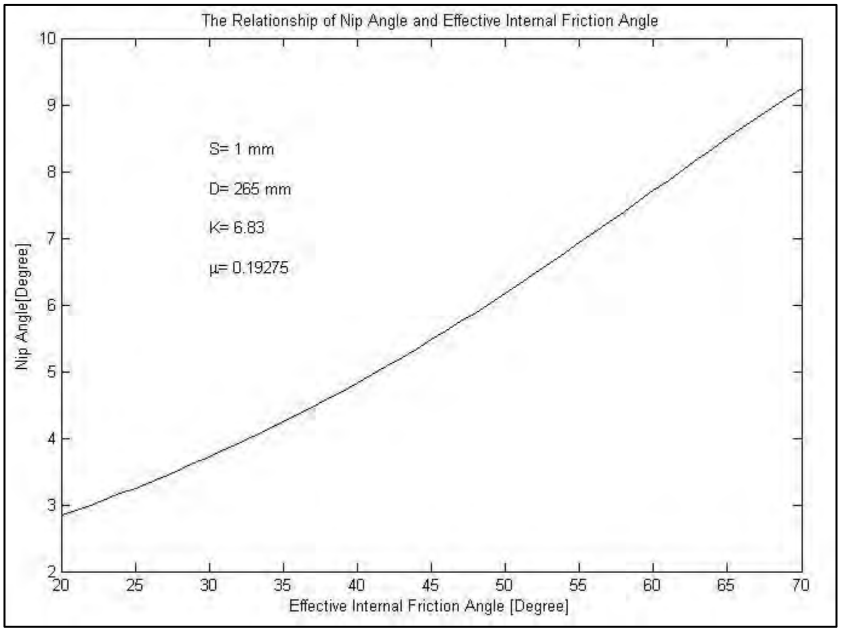

Figure 4.22: The relationship of nip angle and effective internal friction angle (at roll gap of 1 mm).

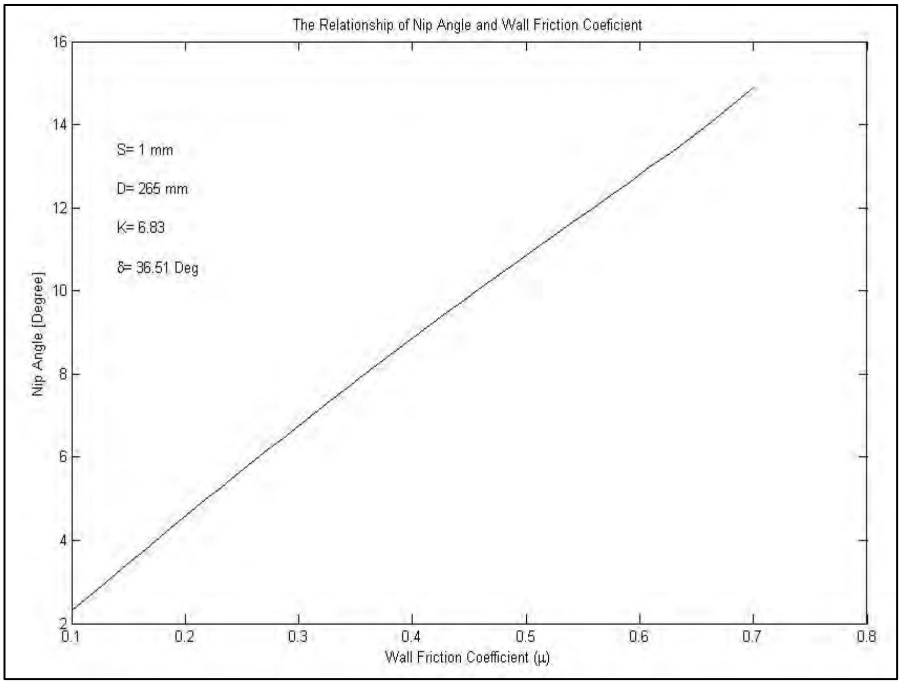

Figure 4.23: The relationship between nip angle and wall friction angle (at roll gap of 1mm).

The nip angle is the starting point to implement this model for the vertical rolling compaction of powders. It is important to know the powder characteristic parameters that influence the value of the nip angle. Although the nip angle cannot be measured directly, Johanson [21] is able to provide the model for predicting this region where the compaction is to take place.

As shown in Figure 4.21, it is observed that the nip angle decreases significantly for materials with high compressibility factor K value. It may be assumed that there is no existence of a slip condition region for an extremely high value of K.

For certain parameter combinations, the nip angle increases if only the internal friction angle increases and as a result more powder is drawn into the region between the rolls producing a higher density compact requiring greater roll pressure (see Fig. 4.22). A similar effect is obtained by increasing the coefficient of wall friction between the roll surface and powder as shown in Figure 4.23.

4.3 Stainless Steel 316L Powder Green Strips

Three stainless steel 316L samples (A, B, C) were acquired in each rolling setup according to the previous planned experimental matrix. One typical image for the 0.5 mm gap, 14 rpm speed combination is shown in Figure 4.24. The relative density of each strip was calculated according to ASTM B962-13 [29] standard by recording the density of the center square section along the strip length direction, which is indicated as red squares in Figure 4.24.

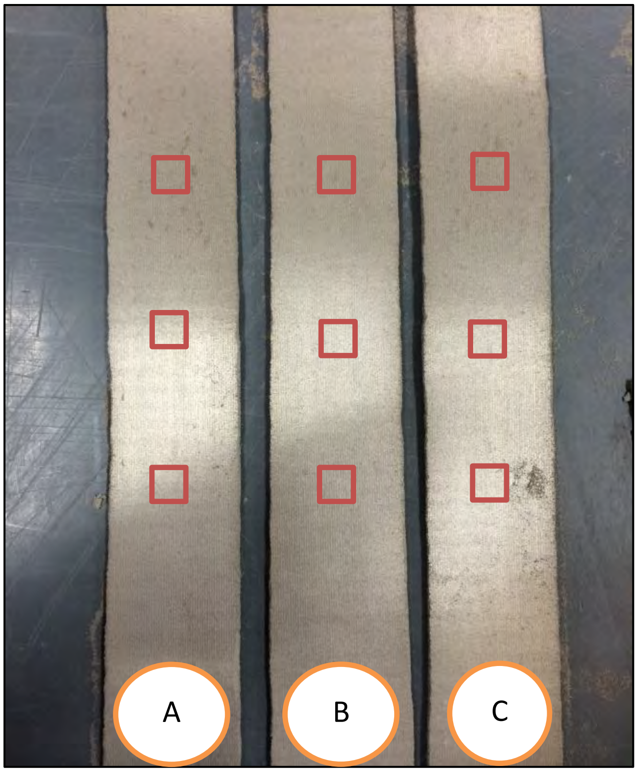

Figure 4.24: Three samples of stainless steel 316L green strip (0.5 mm gap, 14 rpm speed, 2 cm hopper outlet diameter and 65mm face wide).

4.3.1 Rolling Speed Effect

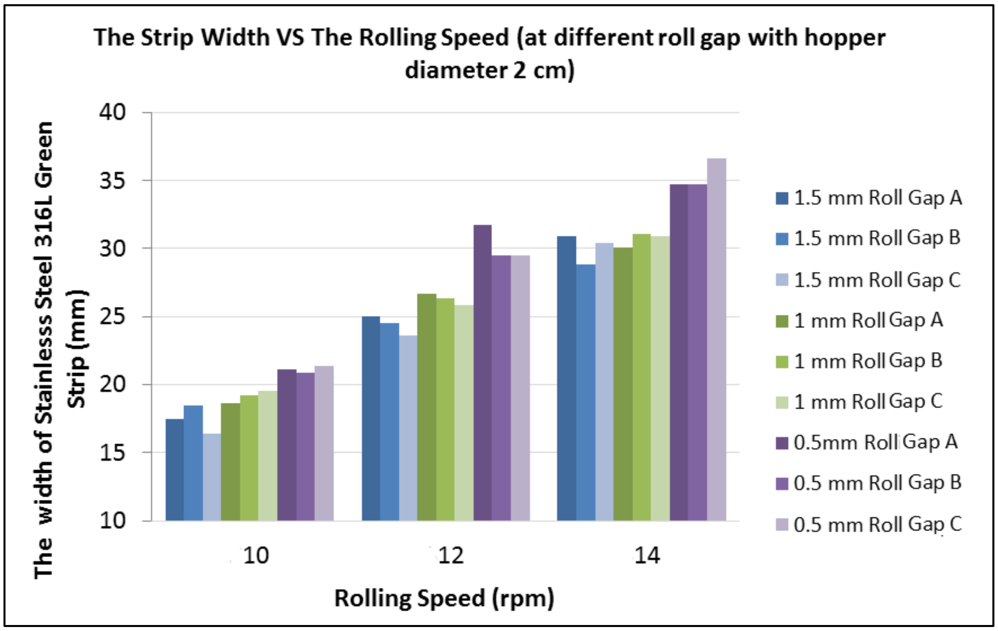

Figure 4.25: The rolling speed effect on the width of green strip (roll face width = 65mm).

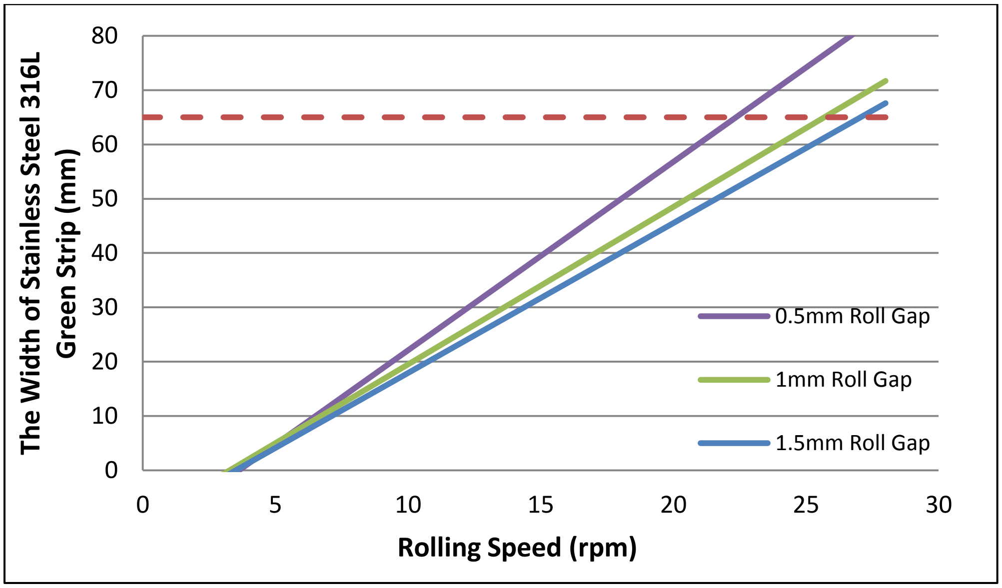

Figure 4.26: Estimation of required minimum rolling speed at three different roll gaps for stainless steel 316L (roll face width = 65 mm).

The results of the rolling speed effect on the strip width are shown graphically in Figure 4.25 above. The results show that the strip width is always smaller than the roll face width of 65 mm and the strip width increases linearly as the rolling speed increases when other rolling parameters are constant. It is easy to understand that the strip width is directly proportional to the rolling speed in a gravity-fed rolling mill. Moreover, the strip width increases when the roll gap is decreased if the rolling speed and the other parameters are constant. It is not difficult to understand that the smaller roll gap indirectly reduces the flow area of powder flowing though the nip region, which means there is more time for powder to stay within the nip region rather than just leaking away.

It may be assumed that the strip width can be equal to the roll face width at a certain point where the rolling speed is higher enough to prevent powder leaking through the roll gap. The minimum rolling speed that is required to roll a full roll face width strip can be estimated if the rolling speed and strip width follows such linear relationship as shown in Figure 4.26. Linear relationships at three different roll gaps were established by the best linear fit line from the bar graphs in Figure 4.25. Three straight lines were further extended to intersect with the horizontal dash line of the 65mm full face width, and then the required minimum rolling speeds for roll gaps of 0.5, 1 and 1.5 mm were found as 23, 26 and 28 rpm respectively. Unfortunately, the present rolling mill is not able to reach the roll speed higher than 14 rpm, so that there is not enough experimental data to support this assumption.

4.3.2 Roll Gap Effect

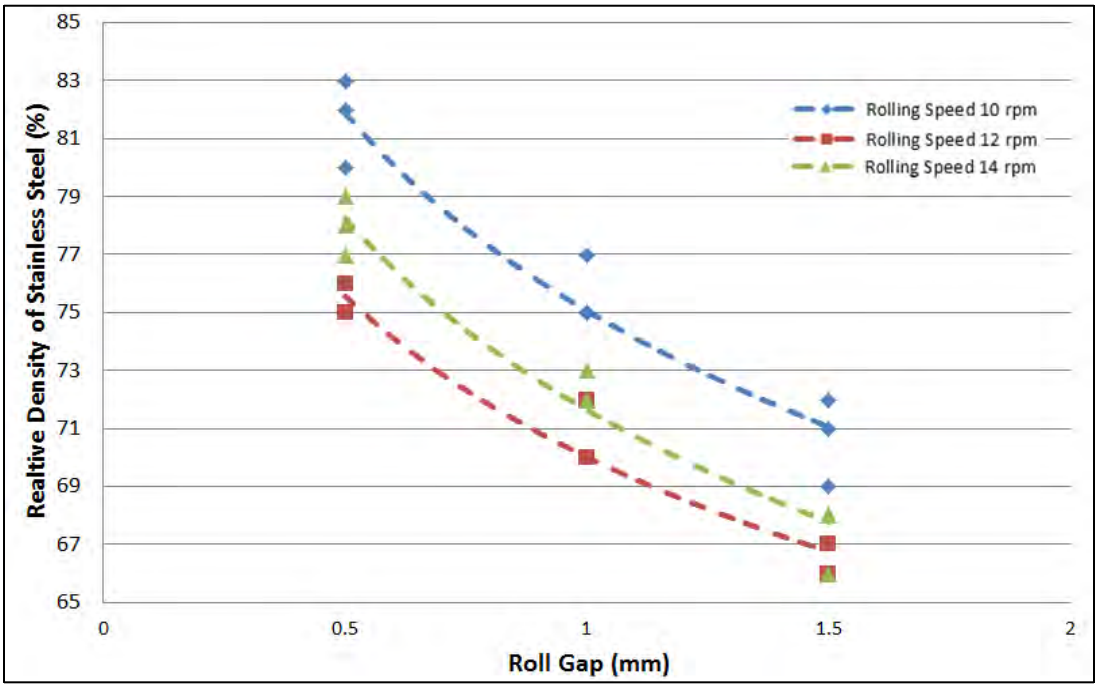

Figure 4.27: The roll gap vs the relative density of stainless steel 316L (hopper diameter: 2 cm; roll face width: 65 mm).

In order to understand the effect of the gap on the material green density, experiments were conducted at different roll gaps and at three varied roll speeds of 10, 12 and 14rpm. The measured experimental results are shown in Figure 4.27. The result is very promising in that the density increases with smaller roll gaps followed by a second order polynomic trend line when other parameters are constant. That is because the roll surface pressure or stress was increased by reducing the distance of the two rollers. Moreover, the slope of the density curve was increased more rapidly if comparing the roll gap from 1.5mm to 1mm and 1mm to 0.5mm particularly as the minimum gap becomes smaller. It is possible that the deviations resulted from the roll gap approaching that of the particle size or that the particle unit density was increased in the compaction region as the gap was reduced.

Although Bindhunmadhavan et al. [24] has pointed out that the higher rolling speed decreases the compaction force and increases the entrainment of air in the strip, which all leads to be the smaller density of the green strip, but the rolling speed effect on the strip density cannot be determined at this stage since there is no specific trend that can be found in Figure 4.27. Therefore, the rolling speed effect discussed in the literature review was not accomplished in the present work. This is probably due to the fact that the rolling speed used in the present experiment was not higher enough to investigate the entrainment of air and additional rolling speed increments are required to investigate the trend of such a relationship.

4.3.3 Feeding Rate Effect

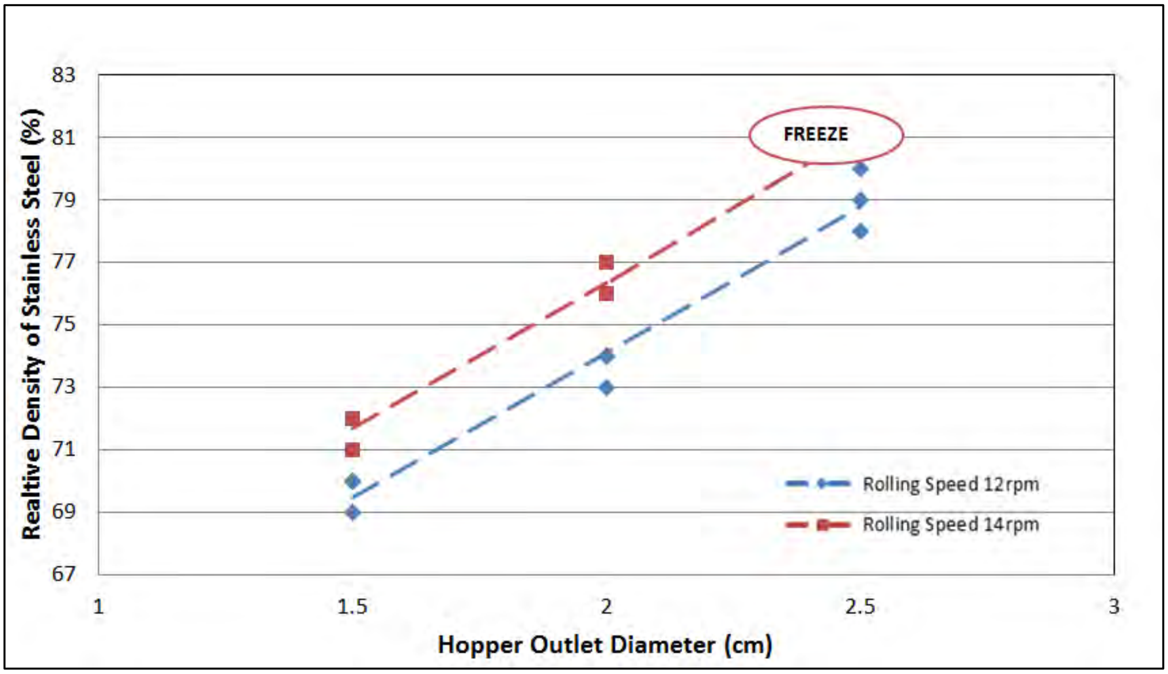

Figure 4.28: The feeding rate vs the density of green strip (roll gap = 0.5mm).

In order to investigate the effect of the powder feeding rate on the relative density, the experiments were carried out at three different hopper diameters (1.5, 2, 2.5 cm) with two rolling speeds of 12 and 14 rpm. The measured results are shown in Figure 4.28 where the linear graphs indicated that the green density of stainless steel 316L increases as the material feeding rate is increased for both rolling speeds 12 and 14 rpm. This can be explained by the fact that feeding rate directly increases the amount of powder flowing though the compaction region within the unit time. However, the rolling compactor was overloaded at the rolling setup of 2.5 cm hopper diameter and 14 rpm rolling speed, and the density of green strip at this setup cannot be measured. It is assumed that a rough relative density of 83% can be speculated if the red line is extended to a certain point (dash line) according to the tendency of the blue line in Figure 4.28. This evidence indicates that a higher rolling force is required since the strip density is proportion to the roll surface pressure. Thus, the highest relative density of stainless steel 316L strip is roughly 80% for this rolling mill when the 65 mm roll face width is used. In addition, the increase in powder feeding rate enlarges the feeding pressure which influences the maximum rolling pressure directly according to Johanson's model.

4.3.4 Roll Face Width Effect

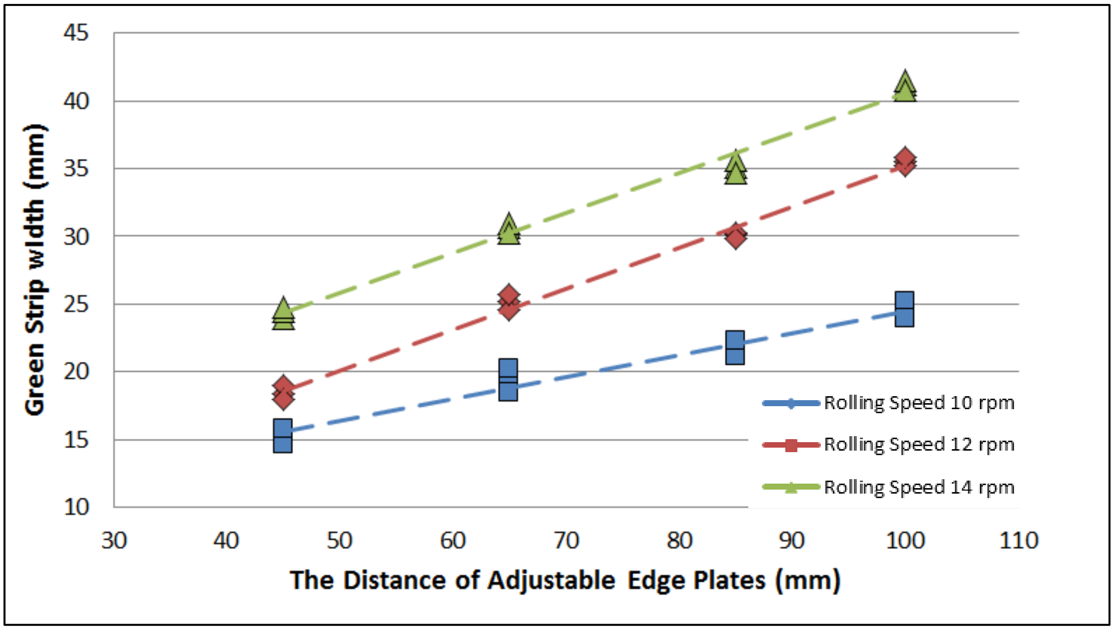

Figure 4.29: The roll face width effect on the strip width of stainless steel 316L.

In order to investigate the roll face width effect on the strip width, the experiments were conducted at four different roll face width distances (45, 65, 85, 100 mm) with three rolling speeds of 10, 12 and 14 rpm. The measured results are shown in Figure 4.29; the strip width is always smaller than the roll face width and it increases linearly as the roll face width is increased without taking consideration of rolling speed effect. The percentage value was obtained from the ratio of strip width to roll face width. The values are remarkably consistent when the rolling speeds are fixed at 10, 12 and 14 rpm. This evidence indicated that rolling speed is the main factor that influences the strip width no matter what face width is given. Once again, the strip width can be equal to the roll face width when the rolling speed is higher enough to prevent the powder leakage and then the roll face width effect is negligible.

4.4 HDH CP-Titanium Powder Green Strips

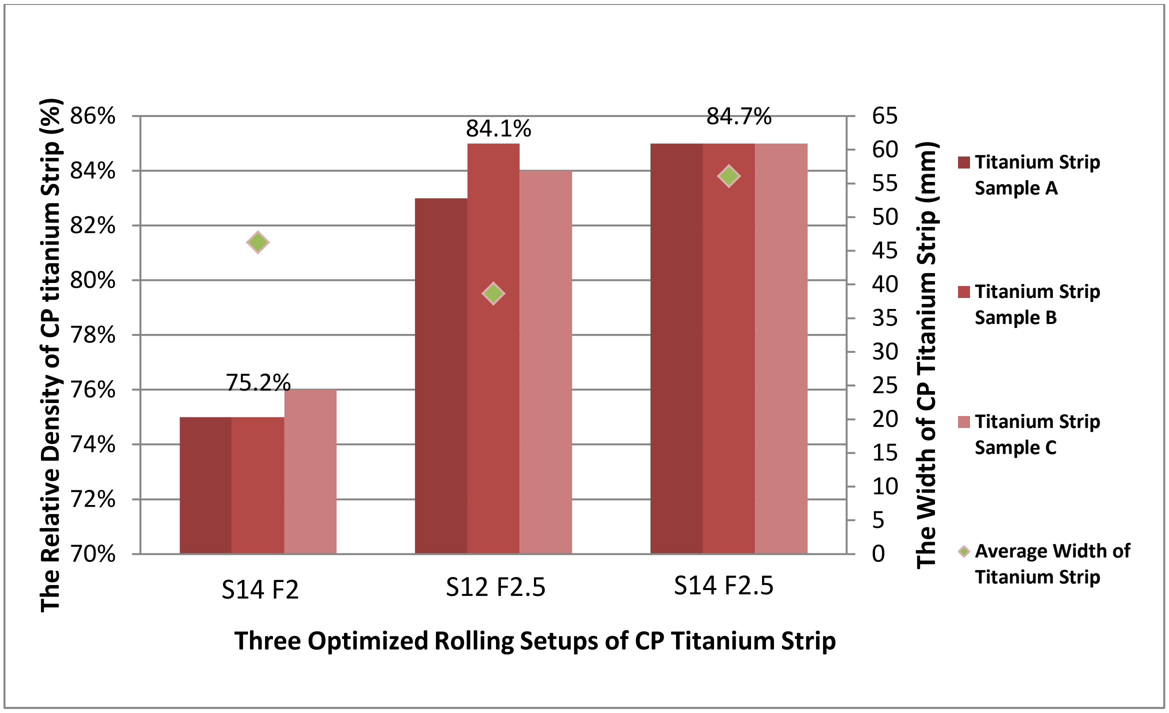

Figure 4.30: The density and width comparison of CP titanium strips at optimized rolling speed and powder feeding rate at 0.5 mm roll gap (Note: the letter S represents rolling speed in rpm and F represents hopper diameter in cm).

The rolling parameter studies were further conducted on CP-titanium powder. It was rolled with a set of optimized rolling parameter setups including 0.5mm roll gap, two hopper diameters (2, 2.5 cm) with two rolling speeds of 12 and 14 rpm and fixed 65 mm roll face width. The measured results are shown in Figure 4.30; the relative densities are represented by the bar graphs and the width of the CP-titanium strips were represented by the secondary y-axis. The rolling behavior of CP-titanium powder was very similar to the stainless steel powder except that the CP-titanium strips are much denser and wider than the stainless steel strips under the same rolling parameter setup. The highest average relative density of 85% was obtained from the rolling setup of 14 rpm rolling speed and 2.5 cm hopper diameter. The evidence further proves the influence of rolling speed and feeding rate on the improvement of the strip width and relative density respectively during gravity-fed powder rolling.

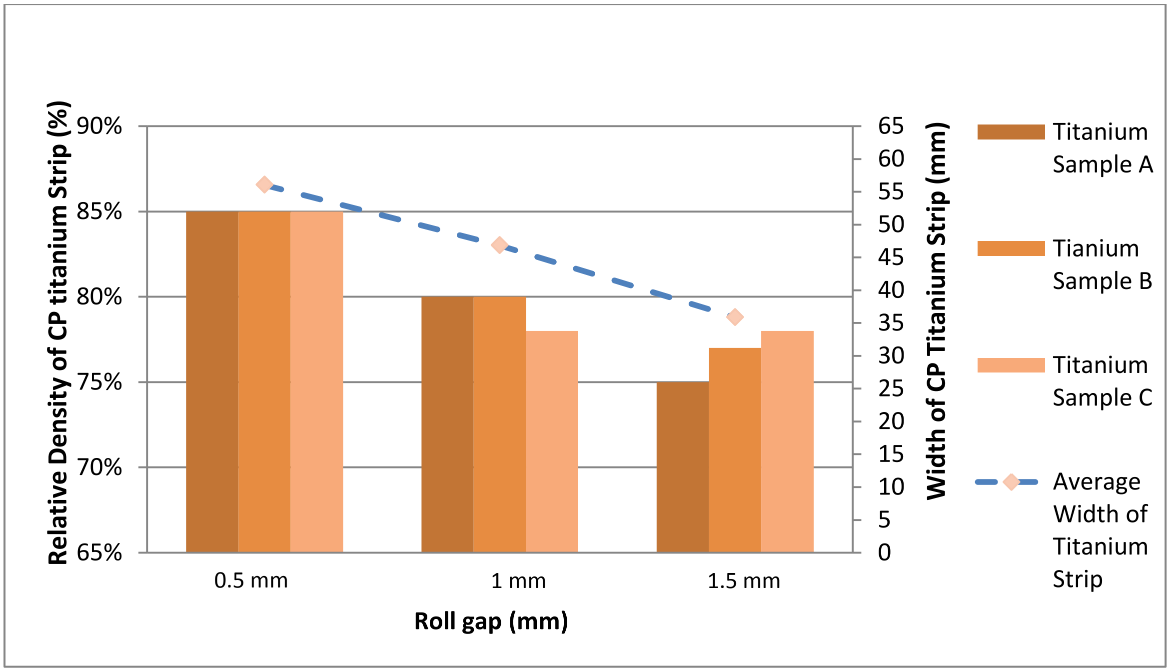

Figure 4.31: The relative density and strip width comparison of CP titanium strips at three different roll gaps (rolling speed: 14 rpm; hopper diameter: 2.5 cm; roll face width: 65 mm)

In order to further investigate the roll gap effect on the CP-titanium powder rolling, the experiments are conducted with a set rolling parameter setups including roll gaps of 0.5, 1 and 1.5 mm with hopper diameter of 2.5 cm and rolling speed of 14 rpm. The measured results were shown in Figure 4.31; the relative densities are represented by the bar graphs and the width of titanium strips are represented linearly by the secondary y-axis. Similarly, the strip relative density is increased approximately 10% and strip width is also increased from 35 mm to 55 mm by reducing the roll gap from 1.5 mm to 0.5 mm. It is easy to misunderstand that the roll gap also influences the strip width. However, the rolling speed mainly influences the pressing time (retention time) of the powder that passes through the nip region, which is related to the amount of material passing through the roll gap (kg/h). In fact, the feeding rate was fixed by using the 2.5 cm diameter hopper at three roll gaps of 0.5, 1 and 1.5 mm in this experiment, which indirectly reduces the amount of material passing through the roll gap and increases the pressing time while the roll gap is subsequently enlarged. In order to maintain a constant strip width in this case, the solution is to either increase the rolling speed or the feeding rate.

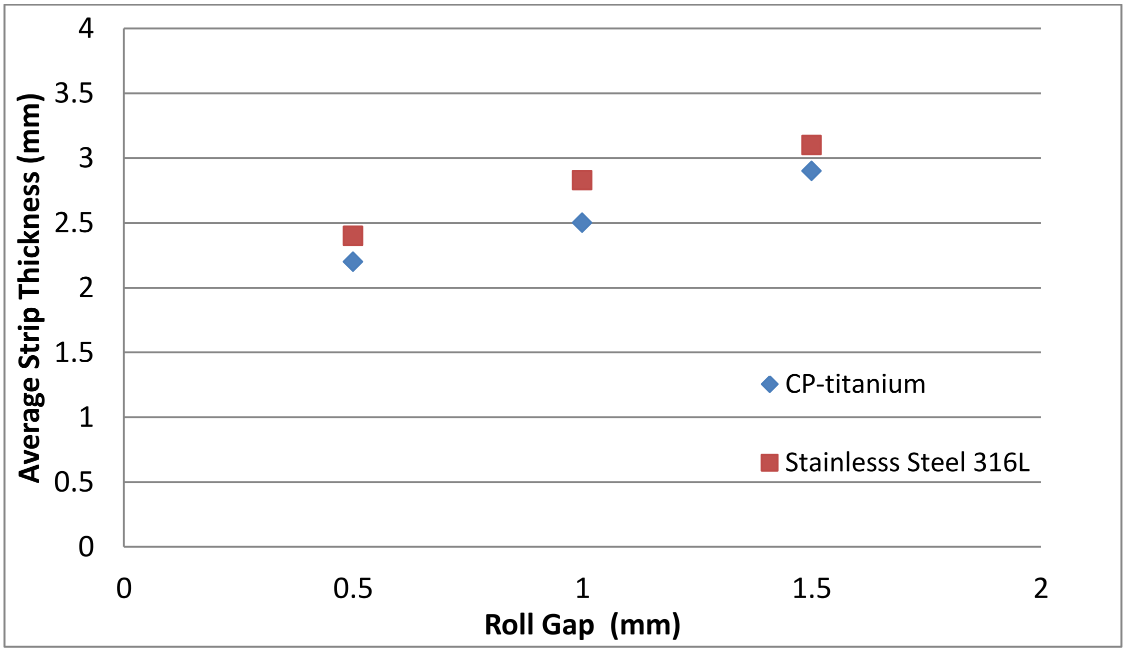

Figure 4.32: The strip thickness comparison of CP-titanium and stainless steel 316L at three roll gap sizes (rolling speed: 14 rpm, hopper diameter: 2 cm and roll face width: 65 mm).

The comparison between the strip thickness and the roll gap is illustrated in Figure 4.32. Surprisingly, the strip thickness was always thicker than the roll gap from the experimental data. The average thicknesses of stainless steel and CP-titanium strips were found as 2.4 and 2.2 mm when the roll gap is 0.5 mm. It is nearly impossible to direct roll both powders for the strip thickness that equals the roll gap due to the powder material and roll spring-back effect during rolling compaction. This difference of strip thickness and roll gap was significantly large at a very small roll gap; the strip thickness was nearly 4 times larger than the roll gap of 0.5 mm. In order to reduce this distinction, these green strips also have been cold re-rolled to reach the thickness that equals to the roll gap, but the final re-rolled strips demonstrated certain degrees of edge cracks as shown in Figure 4.33.

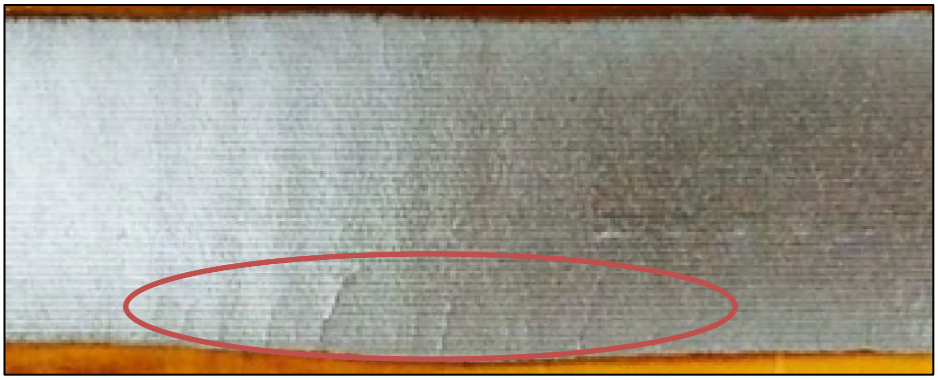

Figure 4.33: Image of CP-titanium strip with edge cracks.

The density variation of CP-titanium green strip across its width was also investigated by evenly cutting 7 square sections from the strip width direction. The measured density distribution curve is given in Figure 4.34 below.

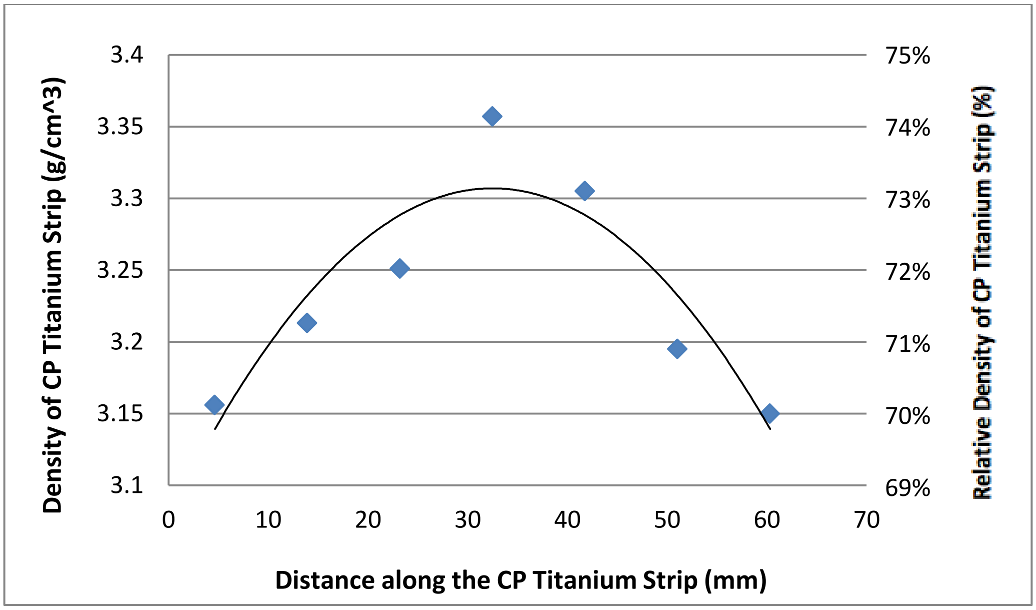

Figure 4.34: The density variation of CP-titanium strip along its width (roll gap: 1mm; rolling speed: 14 rpm; hopper diameter: 2.5 cm; roll face width: 100 mm).

As can been seen from Figure 4.34, the density increases from the strip edge towards the middle section of the strip which has shown a similar variation phenomenon of strip thickness as discussed by Li Yongjun [25]. The largest difference in density variation was investigated to be 6 % from this CP-titanium strip. This could be caused by the fact that the powder flows unevenly from the round hopper nozzle to the rectangular roll gap and the spring-back effect of the rollers that forces more powder material flow into the middle section of the compaction region.

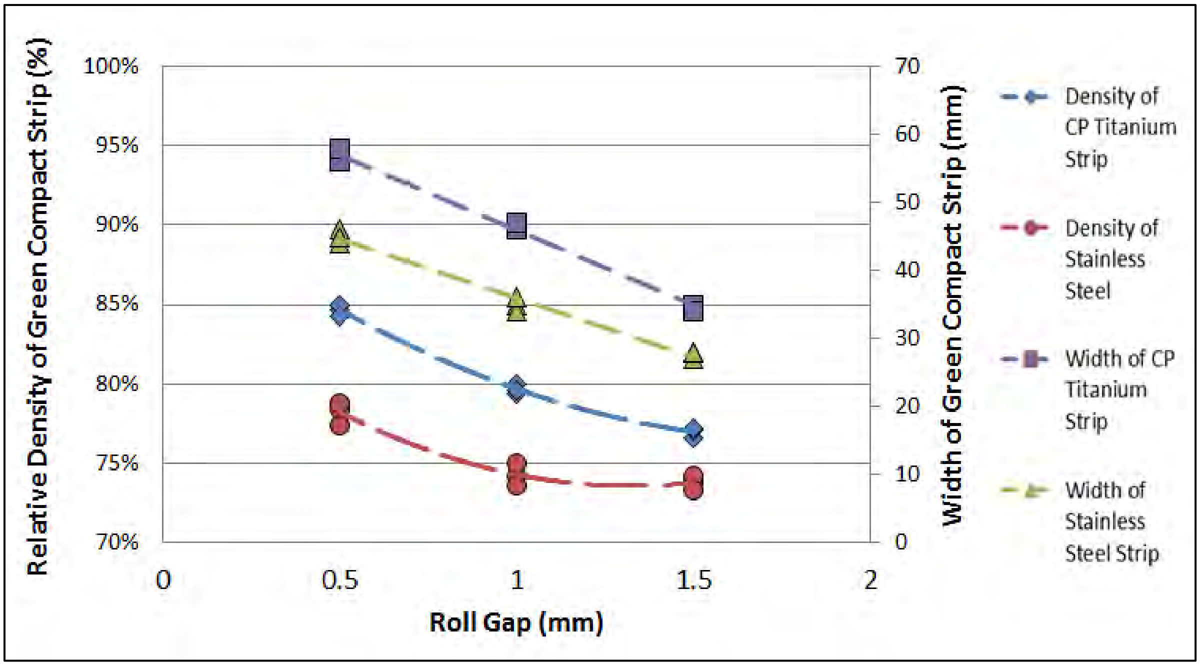

Figure 4.35: The relative density and strip width comparison of CP titanium and stainless steel 316L at identical rolling parameters: 14 rpm rolling speed, 2.5 cm hopper diameter and 65 mm roll face width.

A comparison of CP-titanium and stainless steel strips at identical rolling parameters is established in Figure 4.35. CP-titanium strips have relatively higher density and wider strip width than the stainless steel strips no matter the size of the roll gap. This can be explained by the fact that the compressibility for CP- titanium powder is relatively higher than stainless steel powder during rolling compaction. In addition, the maximum roll pressure difference was mainly influenced by their powder characteristics as discussed at the modelling section.

4.5 Johanson Rolling Model Validation

The validation was implemented in terms of relative density of the rolled strips. The experimental data was only taken for the 2.5 cm outlet diameter hopper setups due to the observation of sub-feeding or non-ideal feeding from the hopper outlet diameters of 1 and 1.5 cm, which means the amount of powder that is provided by such hoppers is too small to reach the feeding angle θ_h, thereby the feed pressures are relatively smaller than the simulated results. The relative densities of the experimental rolled powder compact strips were measured by ASTM B962-13 [29] standard. The predicted green density was calculated by its compressibility curve which was obtained from uniaxial pressing.

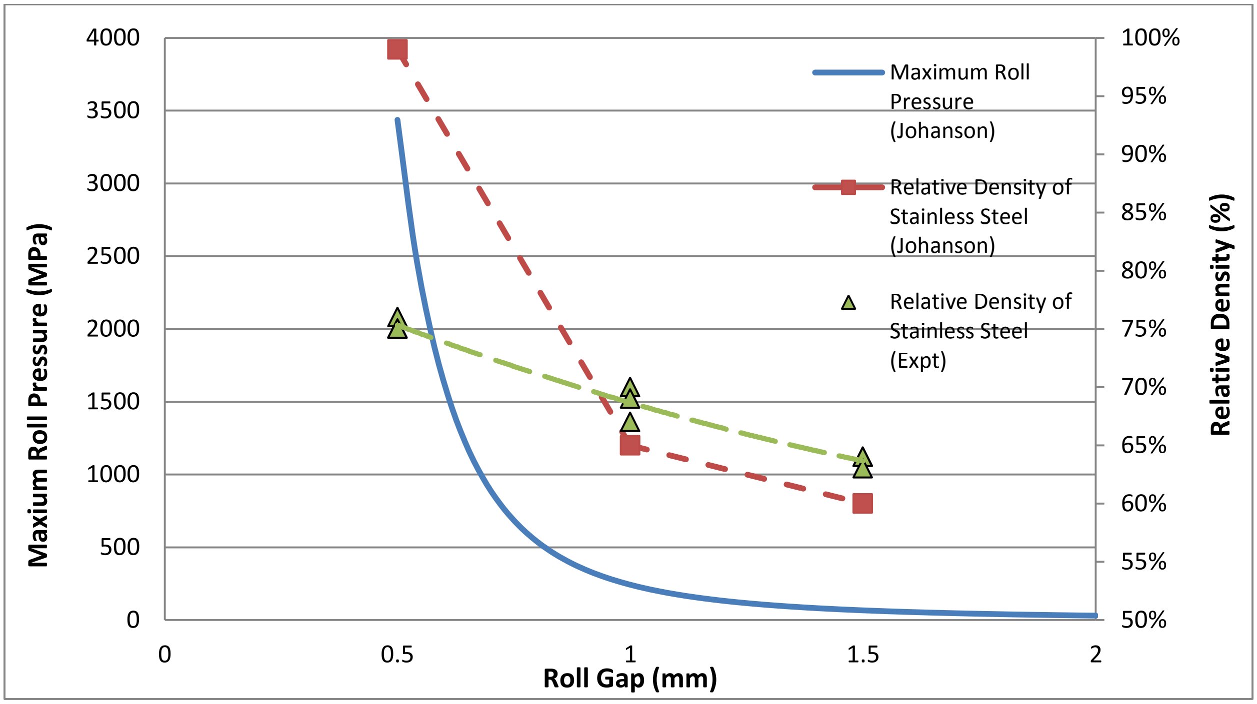

Figure 4.36: Comparison of the predicted and experimental effect of roll gap for stainless steel 316L in terms of relative density.

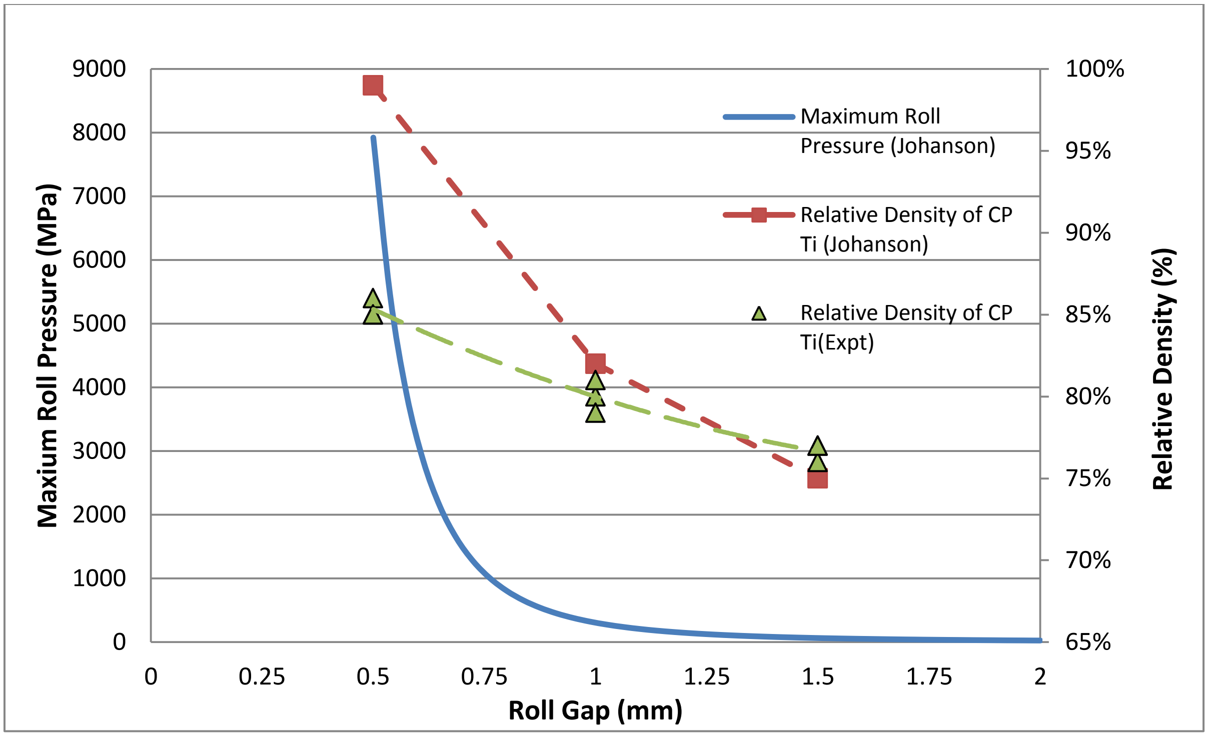

Figure 4.37: Comparison of the predicted and experimental effect of roll gap for CP-titanium powder in terms of relative density.

The results show that the Johanson model is reasonable to provide the relationship between maximum roll pressure and roll gap. The two density curves are nearly matched up except that the experimental relative density is much lower than the predicted density at the smallest gap of 0.5 mm. As discussed in section 4.2.2, the simulated maximum rolling pressure of 8000 MPa and 3300 MPa means is above the yield limit of CP-titanium and stainless steel 316L respectively, which the powder material cannot withstand such pressures and will undergo plastic deformation. Therefore the actual rolling pressures are much smaller than the simulated results. This also can be explained by the fact that the roller was experienced a certain degree of dislocation due to a relative large roll pressure so that the roll gap expanded. In addition, the actual feed pressures from the experimental data are relatively smaller than the estimated values due to the inhomogeneity between the roll face width and the strip width (the strip width is smaller than roll face width). The roll pressure for titanium powder rolling is nearly two times higher than the stainless powder at a roll gap of 0.5 mm which can be further explained why stainless steel powder is not easy to be compacted by the powder rolling process. One pitfall for this validation is that the Johanson model is only valid when feed pressure is constant and all bulk material is fully compacted. The acquired experiment data is limited to these assumptions.

Chapter 5

Results and Discussion of As-sintered and Post Deformation Annealed CP-Titanium Strips

Four of each type 1 and 2 of green CP-titanium strips were sintered at of 1200 °C for 2 hours with a heating rate of 300 °C/hour in order to enhance its mechanical properties and study the contribution of sintering effect on the final density of as-sintered strips. Type 1 and type 2 refer to the strips that were compacted to approximately 75% and 85% relative density respectively. One of each as-sintered type 1 and 2 CP-titanium strips was further cold rolled with 50% reduction followed by an annealing process at a temperature of 750 °C for 30 minutes. The details of the processing steps of these tested specimens are given in Table 5.1.

Table 5.1: Details in processing steps of tested CP-titanium specimens.

Name of Specimen Condition	Processing Step		
	Vacuum Sintering	**Cold Rolling**	**Annealing**
As-sintered 75 (type 1)	✓		
As-sintered 85 (type 2)	✓		
Post-deformation Annealed 75 (type 1)	✓	✓	✓
Post-deformation Annealed 85 (type 2)	✓	✓	✓

These three as-sintered CP-titanium specimens with initial average green density of about 75% and 85% will be referred to as As-sintered 75(1)(2)(3) and As-sintered 85(1)(2)(3) respectively. The three cold rolled and annealed as-sintered tensile specimens with initial average green density of 75% and 85% will be referred to as Post-deformation Annealed 75(1)(2)(3) and Post-deformation Annealed 85(1)(2)(3) respectively and these designations will be used for the stress-strain curves throughout this chapter.

5.1 Analysis of As-sintered CP-Titanium Strips

5.1.1 Porosity and Density of As-sintered CP-titanium Specimens

This section is mainly focused on the porosity and density of as-sintered CP-titanium specimens. The size and the distribution of porosity are seen clearly in Figure 5.1 which includes low magnification micrographs of un-etched as-sintered CP-titanium strips. The measured relative densities and pore sizes which measured statistically by three light microscope images are shown in Table 5.2 below.

Table 5.2: The measured relative density and pore sizes of as-sintered CP-titanium strips.

Specimens	Av.Green Density (%)	Av.As-sintered Density (%)	Pore Sizes of Edge Section (µm)	Pore Sizes of Middle Section (µm)
As-sintered 75 (Type 1)	75.6	88.2	2-150	2-60
As- sintered 85 (Type 2)	85.4	94.3	2-80	2-40

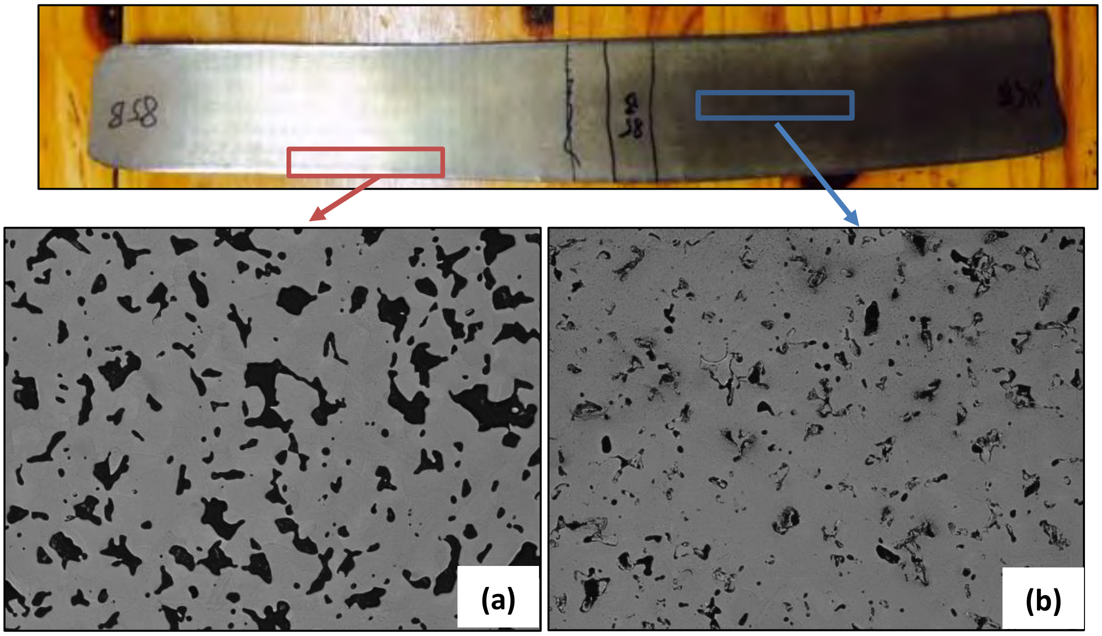

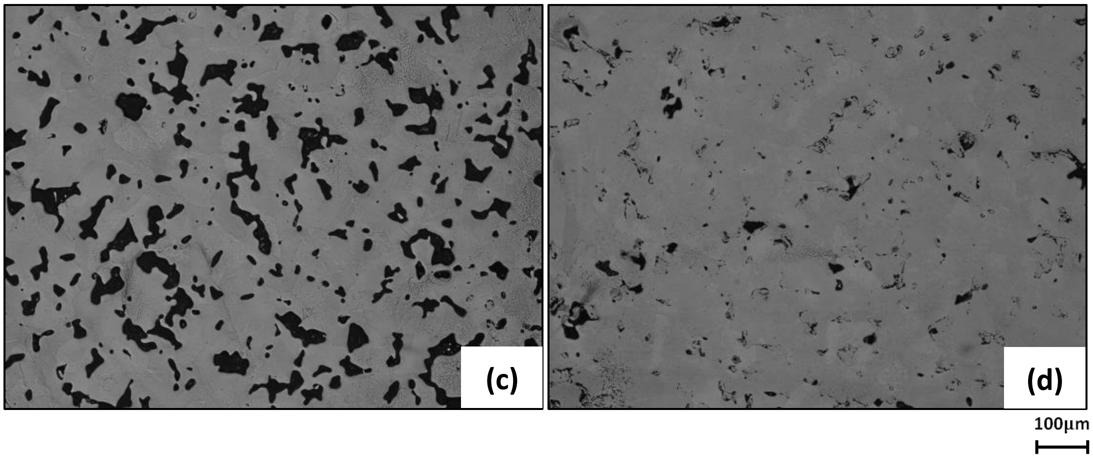

Figure 5.1: Micrographs of the porosity in un-etched (a) as-sintered 75 (type 1) edge section (b) as-sintered 75 (type 1) middle section (c) as-sintered 85 (type 2) edge section (d) as-sintered 85 (type 2) middle section.

As can be seen from Table 5.2 and Figure 5.1, the density and pores of both type 1 and 2 are not evenly distributed along the specimen width and the middle section has relatively higher density and lower porosity than the edge section of the strip which is due to the non-isostatic pressing behavior of rolling compaction.

The middle section of as-sintered 75 strips (type 1) has pore size distribution consisting of larger pores of 40 - 60 µm and smaller pores of about 2 - 20 µm. The middle section of as-sintered 85 strips (type 2) has pore size distribution consisting of larger pores of 30 - 40 µm and smaller pores of about 2 - 15 µm. The as-sintered 85 samples (type 2) show relatively smaller pore size distribution than the as-sintered 75 type 1 after an identical sintering process.

With respect to density comparison of sample type 1 and type 2, the as-sintered 75 strips (type 1) were densified up to 88% and as-sintered 85 strips (type 2) were densified up to 94% after an identical sintering process. In fact, both densities of type 1 and type 2 strips are increased by 13% and 9% respectively. This phenomenon can be explained by the fact that type 1 strip has relatively less surface contact areas associated with particles due to the intensity of rolling compaction deformation, in which the neck growth of type 2 particles is relatively faster than the type 1 CP-titanium strip at the early stage of sintering. In addition, the results have also shown that the high initial relative density of CP-titanium compact strip produced from direct powder rolling process is very critical for the final density obtained from sintering process, because the average relative density of as-sintered 85 strips (type 2) was still approximately 8% higher than the as-sintered 75 strips (type 1).

5.1.2 Tensile Test Results of As-sintered CP-titanium Specimens

All as-sintered CP-titanium tensile specimens discussed from Chapter 3.7 were prepared and tested under a quasistatic strain rate of $1\text{x}10^{-3}\ \text{s}^{-1}$. The plotted stress-strain curves of as-sintered CP-titanium 75 (type 1) and 85 (type 2) specimens are given in Figures 5.2 and 5.3. The measured mechanical tensile properties are shown in Table 5.3.

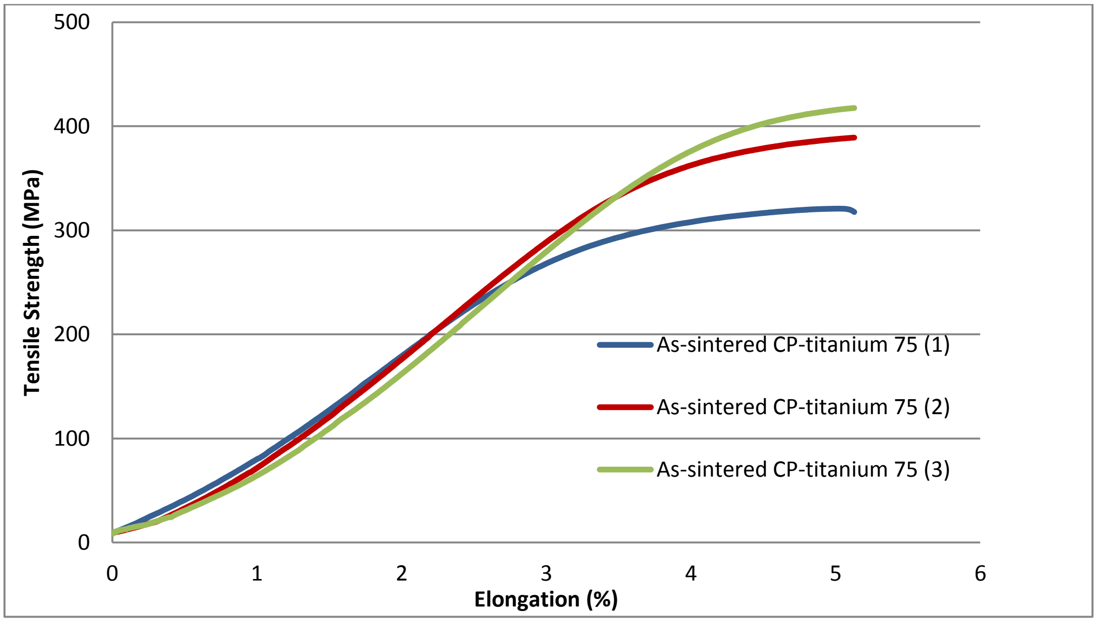

Figure 5.2: The graph of stress-strain curves for as-sintered CP-titanium 75 (type 1) specimens.

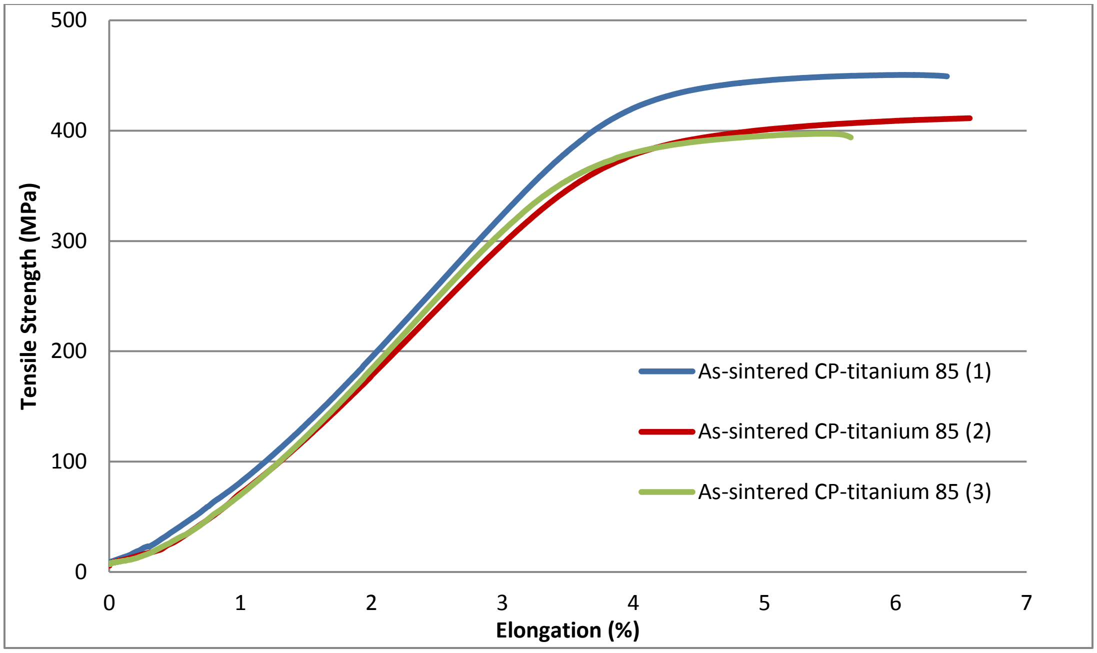

Figure 5.3: The graph of stress-strain curves for as-sintered CP-titanium 85 (type 2) specimens.

Table 5.3: The mechanical tensile properties of as-sintered CP-titanium specimens.

Material Condition	Yield Strength (MPa)	UTS (MPa)	Elongation (%)	Relative Density (%)
As-sintered 75 (Type 1)	250-338	320-419	1.5-3	88
As-sintered 85 (Type 2)	320-350	397-450	3-5	95
Wrought CP Ti Grade 2	335-545	510-605	21-29	99.5

As can been seen from Figure 5.2 and 5.3, both as-sintered 75 (type 1) and 85 (type 2) CP-titanium specimens are very brittle and nearly no plastic deformation occurs before experiencing sudden fracture. With regard to the mechanical tensile properties from Table 5.3, yield strength and ultimate tensile strength of both specimens are still lower than the wrought CP-titanium grade 2 material.

In comparison of these two different material conditions, the as-sintered 85 (type 2) specimens have shown relatively higher mechanical tensile properties and elongation than the as-sintered

75 (type 1) specimens which is mostly due to the difference in density and porosity. The highest yield strengths and ultimate tensile strengths of as-sintered 75 (type 1) and as-sintered 85 (type 2) specimens are 338 and 350 MPa, 419 and 450 MPa respectively. The highest plastic elongation of 5% was measured from the as-sintered 85 (type 2) specimen. Both materials contain irregularly shaped pores whereby some of the pores with sharp edges create stress concentrations at specific regions under tensile load and lead to fast fracture.

5.2 Analysis of the Post-Deformation Annealed Specimens

The as-sintered CP-titanium strip as discussed from the previous section has reached its full density and contains a larger amount of porosity so that it is required to be further densified by an additional cold work with 50% reduction and annealing process to enhance its mechanical properties and ductility.

5.2.1 Porosity and Density of Post-Deformation Annealed Specimens

This section is mainly focused on the porosity and density of post-deformation annealed CP-titanium specimens. The size and the distribution of porosity are seen clearly in Figure 5.4 which includes low magnification micrographs of etched post-deformation annealed CP-titanium strip samples.

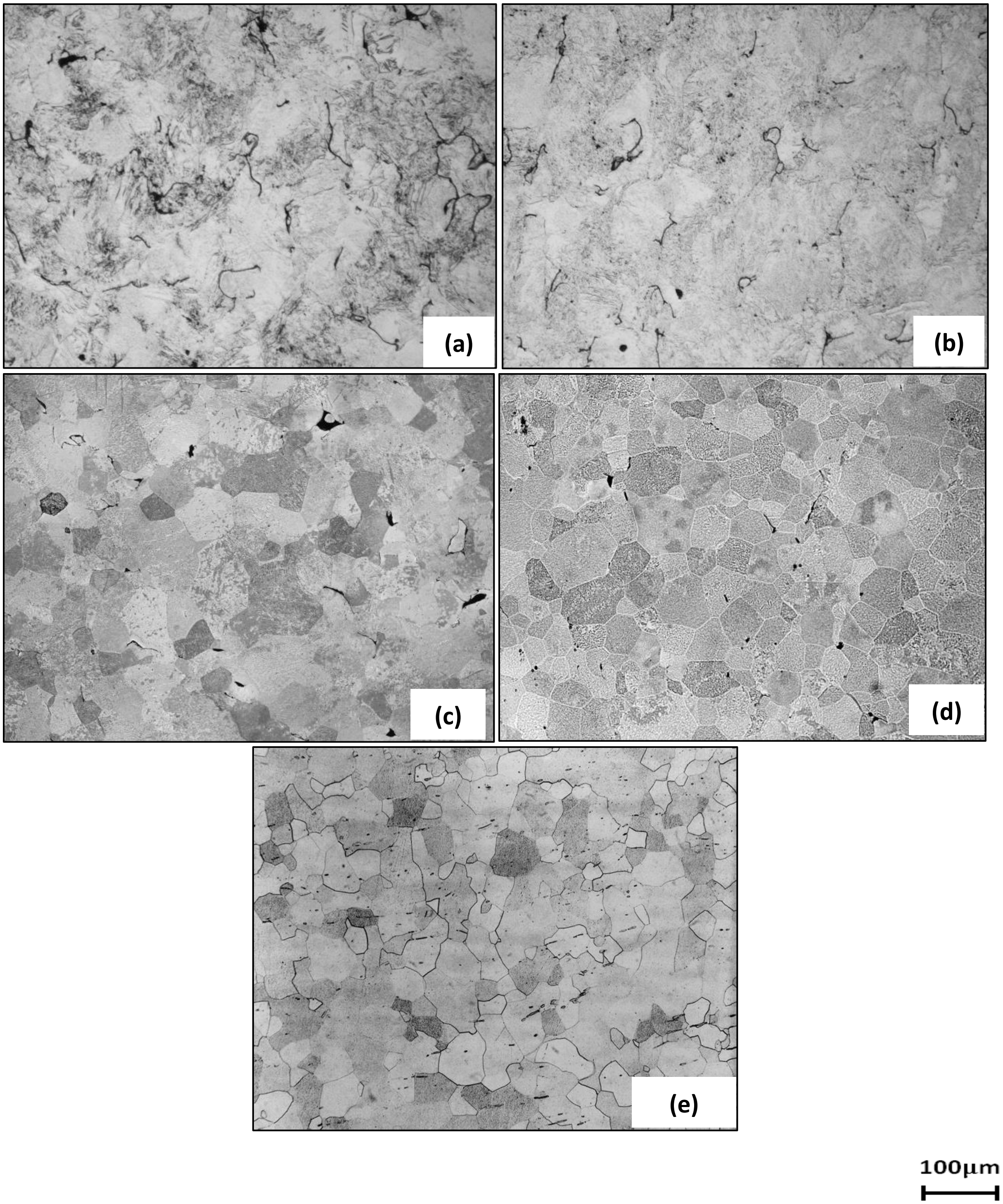

Figure 5.4: Light micrographs of the microstructure in the middle section of (a) cold rolled 75 (type 1) CP-titanium sample (b) cold rolled 85 CP-titanium (type 2) sample (c) cold rolled and annealed 75 CP-titanium (type 2) sample (d) cold rolled and annealed 85 (type 2) CP-titanium sample (e) wrought annealed CP-titanium grade 2 sample [33].

As can be seen from Figure 5.4 (a) (b), these pores from as-sintered CP-titanium strips have not been healed but rather been deformed into many flattened pores after the cold deformation. The grain boundaries were not clearly seen in this condition since they were all elongated in the rolling direction. The created dislocations and increased grain boundary surface area (internal strain energy) among these grains provide the driving force for recrystallization and new grain growth during the subsequent annealing process.

As Figure 5.4 (b) (c) demonstrated, the elongated grains caused by the cold deformation has been fully recrystallized into an equiaxed grain structure which is similar to the wrought CP-titanium grade 2 material after the annealing process, the average pore size was significantly reduced due to the creation of new grain growth from the deformed grain boundaries and the dislocations which were created by the cold deformation. These form many nuclei for new grain growth during recrystallization and results in grains which are smaller than the deformed microstructure. In addition, some of these smaller flattened pores also became the new grain boundaries with the grain growth and the relatively larger pores have not been healed in the recrystallized structure. This explains that the finer powder is more beneficial for the metal powder compacted product since the finer powder can form larger grain boundary area which helps the creation of the fine grain structure after recrystallization, and the finer powder also creates smaller pores which can be easily healed during the post deformation annealing process.

The cold rolled and annealed 85 (type 2) CP-titanium sample from Figure 5.4(d) has less porosity visible than the cold rolled and annealed 75 (type 1) CP-titanium sample from Figure 5.4(c). Although the two samples have both been deformed by 50% cold work, the initial density of as-sintered 85 (type 2) sample was about 8% higher than the as-sintered 75 (type 1) sample which as results in the type 2 sample having higher retained strain and more internal energy for the new grain growth to heal the fattened pores. In the case of the type 1 sample, more thickness reduction is accommodated by pore collapse and hence there is less strain accommodated by the metal when compared to the type 2 sample. The final measured densities of type 1 and type 2 samples are 98.3% and 98.8% respectively which still have not been reached its full density after the post-deformation annealing process.

5.2.2 Tensile Test Results of Post-Deformation Annealed CP-titanium Specimens

All Post-deformation annealed CP-Titanium tensile specimens as described from Chapter 3.7 were prepared and tested under a quasistatic strain rate of $1\text{x}10^{-3}\ s^{-1}$. The plotted stress-strain curves of post-deformation annealed 75 (type 1) and 85 (type 2) specimens are given in Figures 5.5 and 5.6 respectively. The measured mechanical tensile properties of these materials are displayed in Table 5.4.

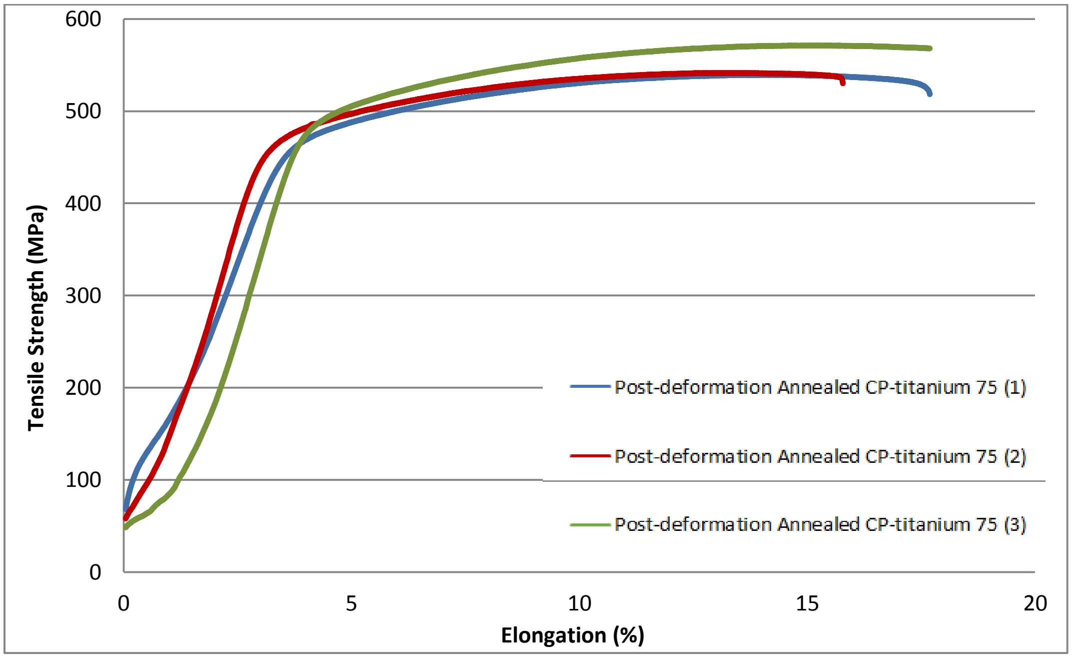

Figure 5.5: The graph of stress-strain curves for post-deformation annealed CP-titanium 75 (type 1) specimens.

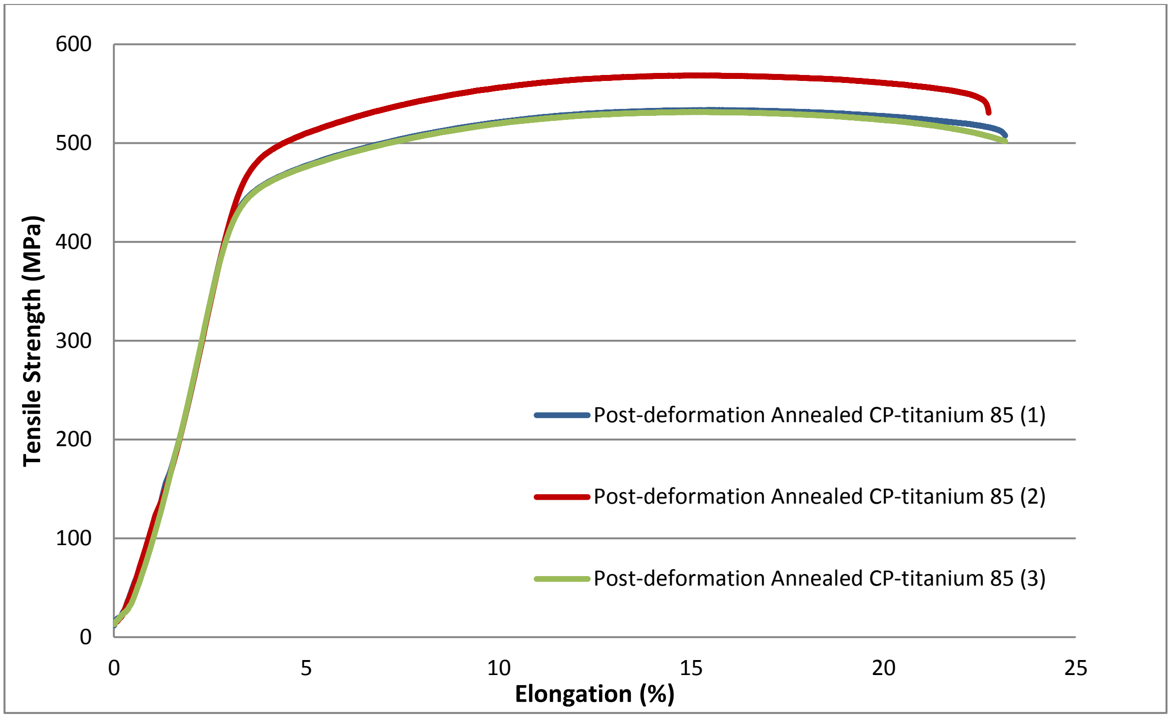

Figure 5.6: The graph of stress-strain curves for post-deformation annealed CP-titanium 85 (type 2) specimens.

Table 5.4: The mechanical tensile properties of post-deformation annealed CP-titanium specimens.

Material Condition	Yield Strength (MPa)	UTS (MPa)	Elongation (%)	Relative Density (%)
Post-deformation Annealed 75 (Type 1)	411-434	541-568	13-15	98.3
Post-deformation Annealed 85 (Type 2)	423-453	530-568	20-21	98.8
Wrought CP Ti Grade 2 [37]	335-545	510-605	21-29	99.5

As can been seen from Figures 5.5 and 5.6, both type 1 and 2 of post-deformation annealed CP-titanium specimens show improved mechanical tensile properties and no sudden fracture was observed. With regard to the mechanical tensile properties in Table 5.3, yield strength and ultimate tensile strength of both types of specimens meet the wrought CP-titanium grade 2 mechanical tensile properties. However, only the elongation of the type 2 specimens satisfies the wrought CP-titanium grade 2 elongation requirement.

In comparing these two different material conditions, the post-deformation annealed 85 (type 2) specimens, show relatively higher mechanical tensile properties and elongation than the post-deformation annealed 75 (type 1) specimens, which is caused by the difference in density and porosity. The highest yield strengths and ultimate tensile strengths of type 1 and type 2 specimens are 434 and 453 MPa, and 568 and 568 MPa respectively. The difference in these two properties between type 1 and type 2 specimens is very small and even identical for the ultimate tensile strength because they have very similar relative densities of 98.3% and 98.8% respectively.

In comparing the plastic elongation results, the plastic elongation ranges of 13-15% and 20-21% were measured for the type 1 and type 2 specimens respectively. These differences can be explained again by the fact that the type 2 specimens have relatively smaller porosity distribution and pore size than type 1 specimens. These irregular pores from the as-sintered material condition have been either reduced in size or healed and resulted in new recrystallized grain boundaries after post-deformation annealing process.

Chapter 6

Conclusions

Based on the research conducted and presented in this dissertation, the following conclusions are drawn:

- The direct powder rolling parameters including roll gap, rolling speed, roll face width and powder feeding rate which have been investigated show significant effects on the integrity of the stainless steel 316L and CP-titanium strip in terms of density and dimensions.

- The powder characteristic parameters including internal friction, wall friction and compressibility demonstrate significant effects on the maximum rolling pressure of the direct powder rolling process.

- The Johanson powder rolling model is able to provide reasonable explanations of relationships between maximum roll pressure, rolling parameters and characteristic powder parameters. But it is also very limited to the rolling speed and powder material yield strength.

- The density of both stainless steel and CP-titanium strip was not evenly distributed across its width. The density of the strip middle section is always higher than the edge.

- The current powder rolling mill is capable to roll maximum 2.4 mm thick CP-titanium strip within relative density up to 85% at an optimized rolling setup. With respect to the rolling mill design perspective, the thickness, width and density of powder compacted CP-titanium strip are possible to be further improved by the rolling parameters including increasing roll gap, roll face width, roll diameter and rolling speed. In particular, the rolling mill is required to have 3 mm roll gap and 1000 mm roll diameter if the spring-back and powder leakage is negligible in order to produce 3 mm thick CP-titanium green strip within relative density above 85%.

- The green density of the CP-titanium strip that was obtained from the direct power rolling process plays a critical role in determining the final density of as-sintered CP-titanium strip.
- The additional cold rolling deformation process after the compaction stage is not an ideal choice for the material densification purpose due to edge cracks are observed on the cold rolled CP-titanium strips.
- Sintering of the direct powder rolled CP-titanium strips at a temperature of 1200°C for 2 hours created a material that is brittle. The CP-titanium powder compacted strips with average relative density of 85% show improved average density of 98.8%, tensile yield strength of 423-453 MPa and plastic elongation of 20-21% after sintering, cold rolling and recrystallization annealing. These properties compare favorably with the wrought CP-titanium grade 2 mechanical property requirements.
- The mechanical tensile properties and the ductility of CP-titanium strip created by powder rolling route are mainly dependent on its relative density and porosity. In particular, the higher density enhances its yield strength and ultimate tensile strength, as well as the smaller porosity and pore size improve its ductility after post deformation annealing.

Chapter 7

Future Work and Recommendations

As a result of the current research and findings, the author suggests the following:

- The powder feeding hopper with a round outlet should be changed to a rectangular outlet. It is thought that this will improve the powder compaction performance since the powder can be fed more evenly through the roll gap.
- Piezoelectric transducers should be installed in the rolling mill in order to monitor the actual roll pressure and the powder feeding pressure changing during powder rolling compaction.
- Any further research conducted on the as-sintered CP-titanium strip produced from the direct powder route should be preceded by a study of Plane Strain Compression (PSC) Tests to reach its full density.
- Further Energy Dispersive Spectroscopy (EDS) analysis should be conducted to test the oxygen content and contaminations of the final post-deformation annealed CP-titanium strips.
- CP-titanium powder was only selected as a start-point for the direct powder rolling route for titanium and titanium alloy sheet products. The Ti-6Al-4V alloy has better mechanical properties than CP-titanium and is more expensive to produce by the conventional route. Therefore studying the Ti-6Al-4V alloy powder rolling by mixing blended elemental powders or master alloy of Al-V powders will be more beneficial and valuable for the titanium alloy sheet material production.

Bibliography

[1] WJ. Kroll, et al. The production of ductile titanium. *Transactions of the Electrochemical Society*, 78:35–47, 1940.

[2] FH. Froes, SJ. Mashl, JC. Hebeisen, VS. Moxson, and VA. Duz. The technologies of titanium powder metallurgy. *JOM Journal of the Minerals, Metals and Materials Society*, 56(11), 46-48, 2004.

[3] Williwe du Preez. The progress in the South African titanium programme, 2013.

[4] G. Lütjering and JC. Williams, *Titanium*, Springer Verlag, 2007.

[5] GS. Upadhyaya, *Powder Metallurgy Technology*, Cambridge International Science Publishing, 1997.

[6] C. Leyens and M. Peters. *Titanium and titanium Alloys*. Wiley Online Library, 2003.

[7] M. Donachie. *Titanium*: *A technical guild*. ASM International, 1988.

[8] G. Lutjering, JC. Williams, and A.Gysler. Microstructure and mechanical properties of titanium alloys. *Microstructure and Properties of Materials*, 1988.

[9] G. Lutjering. Influence of processing on microstructure and mechanical properties of (α + β) titanium alloys. *Material Science and Engineering: A*, 243(1-2):32-45, 1998.

[10] S. Malinov, Z. Guo, W. Sha, and A. Wilson, Differential sanning calorimetry study and computer modeling of beta -> alpha phase transformation in a ti-6al-4v alloy. *Metallurgical and Materials Transactions A*, 32(4), 879-887, 2001.

[11] SL. Semiatin, V. Seetharaman and I. Weiss, 'Hot Working of Titanium Alloys – An Overview', Advances in the Science and Technology of Titanium Alloy Processing, Minerals, *Metals and Materials Society*, 1997.

[12] YT. Lee, M. Peters and G. Welsch. *Metallurgical and Materials Transactions A*, 22(A), 709-714, 1999.

[13] R. German. *Powder Metallurgy Science second edition*. Princeton, 1994.

[14] R. Boyer, E.W. Collings, and G. Welsch, *Materials Properties Handbook: Titanium Alloys*, ASM International, 483-636, 1994.

[15] F. Thummler and R. Oberacker. *An introduction to powder metallurgy*. Institute of Materials series on powder metallurgy, 1993.

[16] D. Schulze. *Powders and Bulk Solids: Behavior, Characterization, Storage and Flow*. Springer, 2008.

[17] VP. Katashinskii, Analytical determination of specific pressure during the rolling of metal powders. *Poroshkovaya Metallurgiya*, 1-10, 1996.

[18] M. Balcaski. Numerical methods for predicting roll press powder compaction parameter. *Ecole Des Mines D'Albi Carmaux*, 2003.

[19] PW. Lee, Y. Trudel, R. Iacocca and RM. German. Powder Metal Technologies and Applications, *ASM Handbook*, 7:389-395, 1998.

[20] DH. Ro, MW. Toaz and VS. Moxson. The direct powder rolling process for producing thin metal strips. *Journal of Metals*, 35: 34-39, 1983.

[21] JR. Johnson. A rolling theory for granular solids, ASME, *Journal of Applied Mechanics*, 32E:4, 1965.

[22] PE. Evans and GC. Smith, Powder Metallurgy, 3:1, 1959.

[23] AW. Jenike and RT. Shield. On the Plastic Flow of Coulomb Solids Beyond Original Failure, *Journal of Applied Mechanics*, 26:599-602, 1959.

[24] G. Bindhumadhavan and MJ. Adams. Roll compaction of a pharmaceutical excipient: Experimental Validation of rolling theory for granular solids. *Chemical Engineering Science*, 60: 3891-3897, 2005.

[25] YongJun, Li. Fabrication of Pure Iron Strips by Direct Powder Rolling Technique and Magnetic Properties. Master's thesis, Wuhan University of Technology, 2006.

[26] VS. Moxson, VA. Duz. Process of Direct Powder Rolling of Blended Titanium Alloys. U.S. Patent 2006/0147333 A1, 2006.

[27] NA. Stone, R. Wilson, M. Yousuff and M. Gibson. Titanium Flat Product Production. U.S. Patent 2010/0183470 A1, 2010.

[28] Y. Shen. Roll Compaction of Pharmaceutical Excipients, PhD Thesis, University of Birmingham, 2012.

[29] http://www.astm.org/Standards/B962.htm [accessed 10 May. 2015].

[30] http://www.astm.org/Standards/E8.htm [accessed 10 May. 2015].

[31] J. Schwedes and D. Schulze. Measurement of flow properties of bulk solids, *Powder Technology*, 61:59–68, 1990.

[32] O. Simon and P. Guigon, Interaction between Feeding and Compaction During Lactose Compaction in a Laboratory Roll Press, PhD Thesis, Université de Technologie deCompiègne, 2000.

[33]http://vacaero.com/information-resources/metallography-with-george-vander-voort/1397-metallographic-preparation-of-titanium-and-its-alloys.html [accessed 10 May. 2015].

[34] O. Simon and P. Guigon, Correlation between powder-packing properties and roll press compact heterogeneity. *Powder Technology,* 130: 257-264, 2003.

[35] JR. Johanson. Factors influencing the design of roll-type briquetting presses. *Proceedings of 9th Biennial Conference of International Briquetting Association*, 17–31, 1965.

[36] http://www.sandmeyersteel.com/images/316-316L-317L-Spec-Sheet.pdf [accessed 10 Nov. 2015].

[37] http://cartech.ides.com/datasheet.aspx?i=101&E=266 [accessed 10 Nov. 2015].

Appendix 1

The ASTM standards used during this dissertation are given in this appendix. For measuring the tensile ASTM B962-13 standard for determining the density of compacted or sintered PM Product followed by ASTM E8/E8M-09 standard for tension testing of metallic materials and powder feed pressure data.

Appendix 2

Powder Feed Pressure Data

	Lactose ∗	**Stainless Steel 316L**	**CP-Titanium**
Bulk Density (γ)	$0.55\ \mathrm{g/cm^3}$	$3.3\ \mathrm{g/cm^3}$	$1.8\ \mathrm{g/cm^3}$
Roll Face Width (W)	50 mm	65 mm	65 mm
Roll Diameter (D)	130 mm	265 mm	265 mm
Roll Gap (S)	1 mm	1 mm	1 mm
Feed Pressure ($\mathrm{P_0}$)	0.06 MPa	0.36 MPa	0.196 MPa

∗ The Lactose data was taken from Simon’ thesis [32].

The values of gravity feed pressure are mainly dependent on the powder material bulk density [34, 35]. Hence, the feed pressures of CP-titanium and stainless steel 316L powder can be estimated by the following relationship of $\gamma \approx \mathrm{P_0}$ from Simon’ data accordingly.